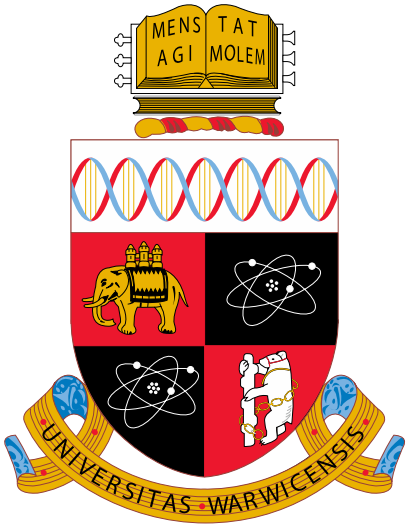


# Photoelectron Spectroscopy Investigation of CdO

by

**James John Mudd**

**Thesis**

Submitted to the University of Warwick in partial fulfilment of the requirements for admission to the degree of

**Doctor of Philosophy**

**Department of Physics**

June 2014

THE UNIVERSITY OF WARWICK

# Contents

# List of Figures

# List of Tables

# Acknowledgements

There are many people who have contributed there help and support in the production of this thesis. Firstly, I should thank my supervisor Prof. Chris McConville for his help, support, and encouragement in guiding me through this PhD. Secondly I would like to thank the many members of the surface science group, in particular Dr. Ajay Shukla for his excellent introduction to UHV and XPS, at the start of this PhD, Rob Johnston for his excellent technical support and discussions. The people I have shared an office with: Dr. Marc Walker, Dr. Chris Burrows, (additionally thanked for proof reading) Dr. Nessa Fereshteh Saniee and Earl Davis for putting up with my craziness and excessive tea consumption, and making coming to work a pleasure. I would also like to thank Dr. Sep Vasheghani Farahani and Dr. Wojciech Linhart for their excellent scientific discussions. Other past and present members of the group: Daesung Park, Dr. Sean McMitchell Dr. Olek Krupski, Dr. Kate Krupski, Dr. Jim Aldous, Dr. Liam Fishwick, Mo Saghir, Dave Kersh and Dr. David Duncan are all thanked for their help and friendship during this PhD.

During the collection of the data presented in this thesis significant time was spent at synchrotrons. Firstly Prof. Philip Hofmann and his group particulary, Dr. Marco Bianchi, Dr. Richard Hatch, Dr. Ed Perkins, at Aarhus University, Denmark, for their excellent technical assistance, introduction to synchrotron ARPES, and mostly for their friendly welcome to their group while conducting experiments. At Diamond Light Source, UK, Dr. Tien-Lin Lee, Dr. F. Venturini and Dr. P.K. Thakur are thanked for there technical assistance and warm welcome while collecting data at beamline I09.

Prof. Russ Egdell, Dr. David Payne, Dr. Phil King, Dr. Tim Veal, Dr. Gavin Bell, and Prof. Phil Woodruff are all thanked for helpful scientific discussions, and pointing me in the right direction, resulting in the completion of this thesis.

Finally I would like to thank my family, my Mum and Dad, brother Mat and sisters Ali and Jen for their support throughout my studies, without which I would have not made it to this point, and especially Ellie who has put up with living with me through this PhD, while all the time being very supportive, and making life outside work very enjoyable.

I would like to dedicate this thesis to my Mum who
passed away during the final weeks of this PhD.

Thanks all!

# Declarations

I declare that this thesis contains an account of my research work carried out at the Department of Physics, University of Warwick, between October 2010 and June 2014 under the supervision of Prof. C. F. McConville. The research reported here has not been previously submitted, wholly or in part, at this or any other academic institution for admission to a higher degree.

The CdO samples investigated in this thesis were grown by Dr. Jesus Zúñiga-Pérez and Professor Vicente Muñoz-Sanjosé (Universitat de Valéncia, Spain), see section 2.4. Dr. Chris Burrows (University of Warwick) conducted the AFM measurements presented in figure 2.17. All the remaining data collection, simulations and analysis have been performed by the author.

James Mudd

June 2014

## Peer Reviewed Papers

**Published articles related to this work:**

1. **J. J. Mudd**, Tien-Lin. Lee, V. Muñoz-Sanjosé, J. Zúñiga-Pérez, D. Hesp, J. M. Kahk, D. J. Payne, R. G. Egdell, and C. F. McConville. *Hard x-ray photoelectron spectroscopy as a probe of the intrinsic electronic properties of CdO,* Phys. Rev. B **89**, 035203 (2014).[1,2]

2. **J. J. Mudd**, Tien-Lin Lee, V. Muñoz-Sanjosé, J. Zúñiga-Pérez, D.J. Payne, R.G. Egdell, C.F. McConville. *Valence-band orbital character of CdO: A synchrotron-radiation photoelectron spectroscopy and density functional theory study,* Phys. Rev. B **89**, 165305 (2014).

**Articles in preparation related to this work:**

1. **J. J. Mudd**, W. M. Linhart, T. D. Veal, V. Muñoz-Sanjosé, J. Zúñiga-Pérez, M. Bianchi, Ph. Hofmann, P. D. C. King, C. F. McConville. *Control of Surface Band gap and Q2DEG of CdO using Alkali Metal Deposition*, In preparation.

**Other published work contributed to by the author during this PhD:**

1. Dae-Sung. Park, **J. J. Mudd**, M. Walker, A. Krupski, D. Seghier, N. F. Saniee, C.-J. Choi, C.-J. Youn, S. R. C. McMitchell, and C. F. McConville, *Pinning effect on the band gap modulation of crystalline $Be_xZn_{1-x}O$ alloy films grown on $Al_2O_3(0001)$*, CrystEngComm **16**, 2136 (2014).

2. C. W. Burrows, A. Dobbie, M. Myronov, T. P. A Hase, S. B. Wilkins, M. Walker, **J. J. Mudd**, I. Maskery, M. R. Lees, C. F. McConville, D. R. Leadley,

[1]This work also appears in the Diamond Light Source Annual Report 2013/2014.
[2]This was also featured as Diamond Light Sources 3000$^{th}$, and I09's first, publication in the spring 2014 newsletter.

and G. R. Bell, *Heteroepitaxial Growth of Ferromagnetic MnSb(0001) Films on Ge/Si(111) Virtual Substrates*, Cryst. Growth Des. **13**, 4923 (2013).

3. **J. J. Mudd**, N. J. Kybert, W. M. Linhart, L. Buckle, T. Ashley, P. D. C. King, T. S. Jones, M. J. Ashwin, and T. D. Veal, *Optical absorption by dilute GaNSb alloys: Influence of N pair states*, Appl. Phys. Lett. **103**, 042110 (2013).[3]

4. N. R. Wilson, A. J. Marsden, M. Saghir, C. J. Bromley, R. Schaub, G. Costantini, T. W. White, C. Partridge, A. Barinov, P. Dudin, A. M. Sanchez, **J. J. Mudd**, M. Walker, and G. R. Bell, *Weak mismatch epitaxy and structural Feedback in graphene growth on copper foil,* Nano Res. **6**, 1 (2013).

5. I. Hancox, L. A. Rochford, D. Clare, M. Walker, **J. J. Mudd**, P. Sullivan, S. Schumann, C. F. McConville, and T. S. Jones, *Optimization of a High Work Function Solution Processed Vanadium Oxide Hole-Extracting Layer for Small Molecule and Polymer Organic Photovoltaic Cells,* J. Phys. Chem. C **117**, 49 (2013).

6. J. D. Aldous, C. W. Burrows, I. Maskery, M. Brewer, D. Pickup, M. Walker, **J. Mudd**, T. P. A. Hase, J. A. Duffy, S. Wilkins, C. Sánchez-Hanke, and G. R. Bell, *Growth and characterisation of NiSb(0001)/GaAs(111)B epitaxial films* J. Cryst. Growth **357**, 1 (2012).

7. W. M. Linhart, Ö. Tuna, T. D. Veal, **J. J. Mudd**, C. Giesen, M. Heuken, and C. F. McConville, *Surface electronic properties of In-rich InGaN alloys grown by MOCVD,* Phys. Status Solidi **9**, 662 (2012).

[3]This work was undertaken as part of an undergraduate project at University of Warwick.

## Conference Contributions

### Oral Presentations

1. *Angle Resolved Photoemission of Quantized Subbands and Many Body Effects in CdO*, MRS Fall, Boston, USA, (December 2011).

2. *Angle Resolved Photoemission of CdO Quantized Subbands*, CMD-24, ECOSS-29, ECSCD-11, CMMP-12, Edinburgh, UK, (September 2012).

3. *Tuning of CdO quantised subbands studied with ARPES*, (Invited) Solid State Talks, University of Oxford, UK, (January 2013).

### Poster Presentations

1. *ARPES Investigation of CdO Quantised Subbands*, Vacuum Symposium, Coventy, UK (October 2012).

2. *Structure Determination of CdO(100): A Combined Quantitative LEED and DFT Study*, DPG Spring Meeting, Dresden, Germany, (April 2014).

# Abstract

In this thesis a variety of photoelectron spectroscopy techniques have been applied to study CdO, in order to gain a more detailed knowledge of both the bulk and surface electronic properties of this material. Hard x-ray photoelectron spectroscopy (HAXPES) has been used, relaxing the surface preparation requirements of conventional photoemission techniques. This allows CdO to be measured in an as-grown condition with the associated higher carrier concentrations. The effects of conduction band filling and final state screening have been observed, and a discussion of the bulk-like sensitivity of HAXPES is given. The use of synchrotron radiation allows variation of the photon energy used to excite photoelectrons, and this is combined with the associated changes in photoionisation cross-sections to study the orbital character of the CdO valence band (VB). These measurements have been compared to density functional theory (DFT) calculations, using three functionals. It was found that using LDA+$U$ and employing a theoretically calculated value of $U = 2.34$ eV can adequately reproduce the experimentally measured Cd $4d$ shallow core level position. The photon energy dependence of the shape of the VB, however, was not reproduced by the DFT calculations, indicating that additional Cd $5p$ character may be present within the VB, and that the O $2p$ photoionisation cross-sections may by underestimated at higher photon energies. The electron accumulation layer known to exist at the CdO surface has been tuned by the addition of Rb, which allowed the 2D electron density to be almost doubled. The effects of the increased 2D electron density on the surface band gap narrowing have been investigated by simulating the subband dispersion using the Poisson-Schrödinger model. The effective mass of the subband states has been extracted, and was found to be significantly lower than the reported bulk mass, which is discussed in the context of other recent results.

# Abbreviations

| | |
|---|---|
| *e-e* | electron-electron. |
| *e-i* | electron-ion. |
| *e-p* | electron-phonon. |
| 2DEG | 2D electron gas. |
| AFM | atomic force microscopy. |
| ARPES | angle resolved photoelectron spectroscopy. |
| BE | binding energy. |
| BGR | band gap renormalisation. |
| BZ | Brillouin zone. |
| CB | conduction band. |
| CBB | conduction band bending. |
| CBM | conduction band minimum. |
| CNL | charge neutrality level. |
| DFT | density functional theory. |
| DOS | density of states. |
| EDC | energy distribution curve. |
| EELS | electron energy loss spectroscopy. |
| EOS | equation of state. |
| ESCA | electron spectroscopy for chemical analysis. |
| fcc | face centred cubic. |
| FE | Fermi edge. |
| FL | Fermi level. |

| | |
|---|---|
| FLL | fully localised limit. |
| FWHM | full width at half maxium. |
| GGA | generalized gradient approximation. |
| HAXPES | hard x-ray photoelectron spectroscopy. |
| IBA | ion bombardment and annealing. |
| IMFP | inelastic mean free path. |
| KE | kinetic energy. |
| LAPW | linearised augmented-plane wave. |
| LDA | local density approximation. |
| LEED | low energy electron diffraction. |
| MDC | momentum distribution curve. |
| ML | monolayer. |
| MOVPE | metalorganic vapor-phase epitaxy. |
| MTFA | modified Thomas-Fermi approximation. |
| NFE | nearly free electron. |
| PDOS | partial density of states. |
| PES | photoelectron spectroscopy. |
| Q2DEG | quantised 2D electron gas. |
| RMS | root mean square. |
| SR-PES | syncrotron radiation photoelectron spectroscopy. |
| SXPES | soft x-ray photoelectron spectroscopy. |
| TCO | transparent conducting oxide. |
| TOA | take-off angle. |
| TPD | temperature programmed desorption. |
| TSP | titanium sublimation pump. |
| UHV | ultra high vacuum. |
| UPS | ultraviolet photoelectron spectroscopy. |

| | |
|---|---|
| VB | valence band. |
| VBB | valence band bending. |
| VBM | valence band maximum. |
| ViGS | virtual gap states. |
| VUV | vacuum ultraviolet. |
| XPS | x-ray photoelectron spectroscopy. |
| XRD | x-ray diffraction. |

# CHAPTER 1

# Introduction

## 1.1 Overview

Oxide electronics are a rapidly developing area in materials science as industry looks to move beyond silicon and III-Vs for both higher performance and novel functionality [1]. In particular, the surfaces and interfaces of oxide materials offer a host of novel functional properties, such as a 2D electron gas (2DEG) [2, 3]. This potential has lead to increased interest in oxide materials, both for their fundamental physical properties, and with a strong view to applications which currently include solar cells, organic electronics, gas sensors, display technologies, catalysis, solar water splitting, batteries, and fuel cells [4–6]. The current progress in oxide materials appears to be driven by the ability to accurately control the growth of these materials at the atomic level. As an example of the high quality of oxide materials now being produced, the quantum Hall effect has recently been observed in a $ZnO/Mg_xZn_{1-x}O$ heterostructure by Tsukazaki *et al.* [7], an effect which until recently had only been observed in high quality conventional semiconductor materials (Si, Ge, III-Vs). Atomic level control over oxide interfaces has resulted in the discovery of many unexpected properties. For example, the lanthanum aluminate ($LaAlO_3$) / strontium titanate ($SrTiO_3$) interface, consisting of two non-magnetic band insulators, has been shown to host a high-mobility 2DEG [8, 9] which can be-

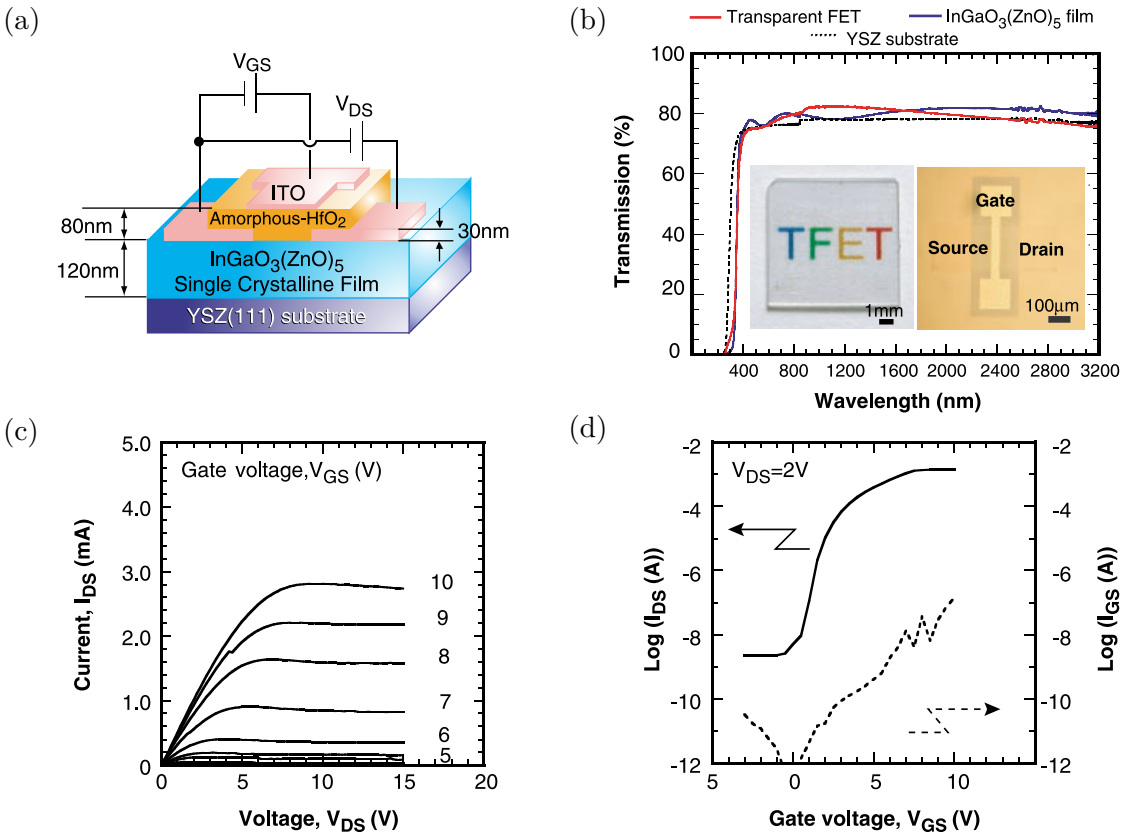


**Figure 1.1.** A transparent field effect transistor (TFET). (a) Schematic of the TFET device structure (b) Optical transmission spectra of the TFET, the YSZ substrate and $InGaO_3(ZnO)_5$ layer for comparison. (c) and (d) Output characteristics of the TFET indicating an on-off current ratio of $\sim 10^6$. Figure adapted from [13].

come superconducting [10, 11], and which in addition displays unexpected magnetic effects such as a large negative magnetoresistance [12]. Progress is also being made in producing fully transparent electronic devices. Nomura *et al.* [13] have produced a transparent field effect transistor (TFET) where $InGaO_3(ZnO)_5$ is used as the channel layer, as shown in figure 1.1. This begins to demonstrate the potential of oxide electronics for new applications such as transparent displays, or invisible solar cell coatings on windows.

Currently oxide materials are commonly used in electronics as transparent contacts. This class of materials, known as transparent conducting oxides (TCOs), exhibit the normally mutually exclusive properties of optical transparency and electrical conductivity. This combination of properties makes this class of materials desirable for many of the applications listed above. Currently, the most widely used TCO

material is Sn-doped $In_2O_3$ (ITO), however, there is a desire to move away from this material due to the scarcity and associated cost of indium [14, 15]. Possible alternatives include CdO, ZnO, $Ga_2O_3$ and $SnO_2$, all of which can be doped to give transparent films with high conductivity. The source of the high conductivity observed in this class of materials is still the subject of considerable debate, with almost all TCO samples exhibiting high *n*-type carrier concentrations without intentional doping. The source of this conductivity has, historically, been assigned to oxygen vacancies which are thought to be difficult to prevent during the growth of these materials. However, with the advent of advanced oxide growth techniques the role of other defects, defect complexes, and the incorporation of hydrogen are now also thought to play a crucial role [16]. The reason for these defects appearing to be electron donors which increase the carrier concentration, instead of compensating or forming *p*-type material, can be understood in terms of the charge neutrality level (CNL) which will be discussed further in section 1.4.

## 1.2 Outline of the Thesis

This thesis aims to investigate the electronic properties of epitaxial thin films of CdO by employing a variety of different photoemission and other associated surface science techniques. In the remainder of this chapter a brief introduction to CdO is given followed by an introduction to the CNL. Finally, an introduction to the surface electronic properties of CdO as known to date are briefly reviewed. Chapter 2 introduces the experimental techniques used in the course of this thesis, in particular photoelectron spectroscopy is described, along with the supporting techniques of Hall effect and low energy electron diffraction (LEED). An outline of the key experimental facilities at University of Warwick (Coventry, UK), ISA (Aarhus, Denmark), and Diamond Light Source (Didcot, UK) that were used within this thesis are also given in this chapter. This is followed in chapter 3 by an overview of the theoretical methods and background required for analysing the data in the

thesis; including models of semiconductor band structure and space charge layers. In chapter 4 hard x-ray photoelectron spectroscopy (HAXPES) is used to allow the intrinsic properties of as-grown CdO to be investigated without the need for surface preparation. In chapter 5, synchrotron radiation is again employed to allow photoemission data to be obtained using a wide range of photon energies. This allowed the valence band orbital character of CdO to be investigated in detail by taking advantage of varying photoionisation cross-sections. In chapter 6, angle resolved photoelectron spectroscopy (ARPES) has been used to measure the quantised 2D electron gas (Q2DEG) at the CdO surface. This Q2DEG is then modified by the addition of Rb to the surface and the effects investigated. Finally in chapter 7 the main conclusions resulting from this work are brought together and an outlook for future work is presented.

## 1.3 Cadmium Oxide

Cadmium oxide (CdO) was the first TCO to be discovered (in 1902 by F. Streintz [17]), and the first to be produced as a thin film (in 1907 by K. Badeker [18]). This was some 40 years before the now commonplace TCOs $SnO_2$ and $In_2O_3$ were developed [4]. A recent review article [19], however, suggested interest in CdO has rapidly increased since 2005, with the growth of higher quality films and nanomaterials opening up new fundamental studies and application possibilities. CdO can be produced by a wide variety of growth processes including: MOVPE [20, 21]; MBE [22, 23]; PLD [24, 25]; sol-gel [26, 27] and sputtering [28]. It has been suggested that CdO is potentially an ideal TCO for use in solar cells [29] as it allows optical transmission extending into the infrared ($>$ 1500 nm) combined with extremely low resistivity. Recent growth of nano-structured CdO has led to potential gas-sensing applications including detection of liquid petroleum gas (LPG) [30], $CO_2$ [31] and $NO_x$ [32, 33], all of which have uses in environmental monitoring applications.

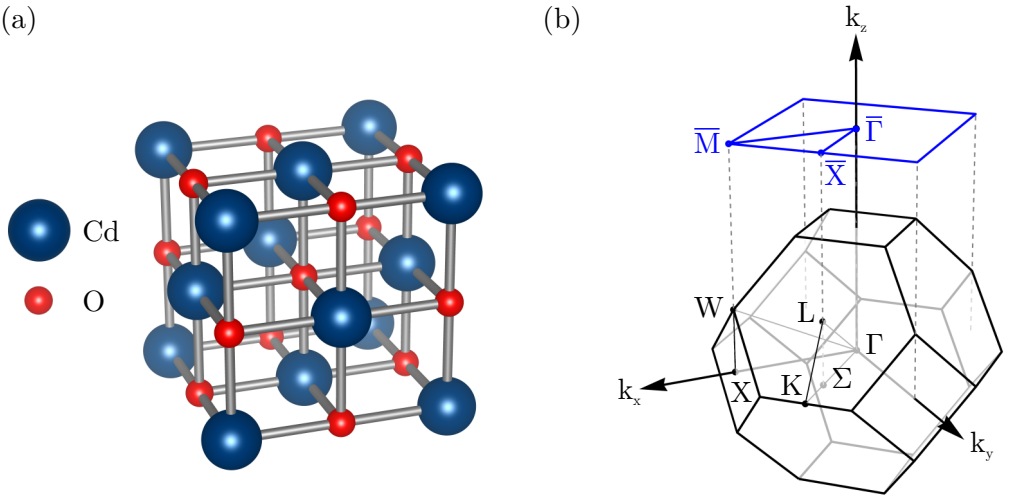


**Figure 1.2.** (a) The real space crystal structure of CdO [40] (b) The fcc BZ of CdO and the surface BZ for the (001) surface. The bulk and surface high symmetry points are labeled.

CdO crystalises in the rock-salt structure ($Fm\bar{3}m$) consisting of a face centred cubic (fcc) lattice with a two atom basis, Cd at (0,0,0) and O at ($^1/_2$, $^1/_2$, $^1/_2$), with a lattice parameter of 4.695 Å [20, 34] as shown in figure 1.2 (a). The Brillouin zone (BZ) for CdO is therefore the fcc BZ as shown in figure 1.2 (b), where the (001) surface projection is also shown. The fundamental band gap of CdO is $\sim$ 0.9 eV ($\sim$ 1400 nm) [35–37], and while this is much too low for optical transparency (400 to 700 nm), this gap is indirect and therefore significant optical absorption is suppressed until the direct band gap of $\sim$ 2.2 eV ($\sim$ 560 nm) [38, 39]. While this band gap is still insufficient for full optical transparency, CdO can be heavily doped, with the resulting Moss-Burstein shift leading to optical band gaps $>$ 3.1 eV ($\sim$ 400 nm). This make CdO fully optically transparent, along with extremely high carrier concentrations ($> 10^{21}$ cm$^{-3}$) [21, 29], which result in high conductivity.

## 1.4 Charge Neutrality Level

When the Schrödinger equation is solved for a periodic crystalline structure in terms of Bloch functions (as will be described in section 3.1), the application of periodic boundary conditions requires that the wavevectors are real [41]. When the period-

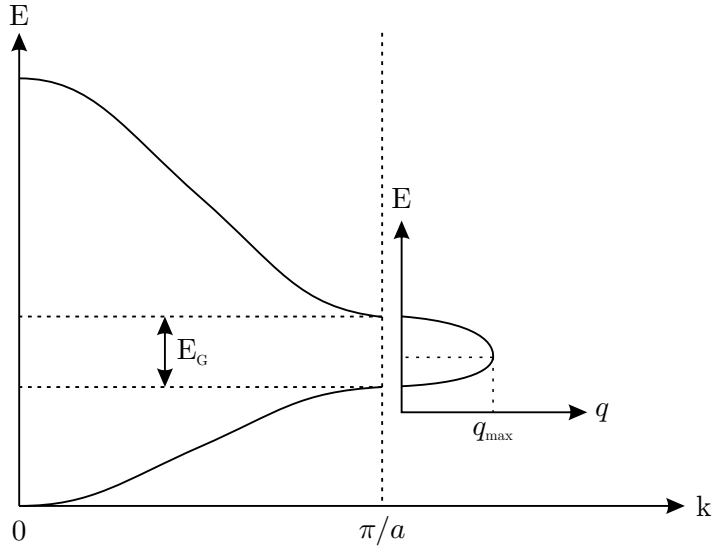


**Figure 1.3.** Complex band structure for a 1D lattice in the nearly free electron model. Within the band gap at the BZ boundary the imaginary component of the band structure is plotted. The maximum complex wavevector $q_{max}$ occurs just below mid-gap. Reproduced from [43].

icity of a crystal is broken by a surface, states with imaginary wavevectors become valid solutions of the Schrödinger equation. The imaginary nature of these states ensure they are evanescent, that is they decay exponentially both into the vacuum and into the bulk of the solid i.e. they are states localised at the surface, these states are commonly referred to as Shockley states [42].

The most simple approach to understand such states is to consider the complex band structure of a 1D lattice within the nearly free electron (NFE) model. Despite the relative simplicity of this model, it provides significant insight into the nature of these surface states. An excellent discussion is given by Mönch [43], and is summarised here. In the NFE model, solving for the dispersion including a periodic potential opens an energy gap at the BZ boundary, as shown in figure 1.3. Additionally, solutions of the form $k = \pi/a + iq$, with real energies are found within this gap. These states are meaningless in the bulk (as they cannot be normalised), and hence are termed virtual gap states (ViGS) [44]. Although described here in 1D, the same ideas can be extended with considerable complexity into 3D [45, 46].

As ViGS derive from bulk states their character changes from predominantly donor-

like close to the VB to predominantly acceptor-like close to the CB. The energy at which a state has equal probability of being either donor or acceptor in nature is termed the branch-point energy or alternatively the charge neutrality level (CNL) [47, 48]. In the 1D case this energy is located at $q_{max}$ which is just below the mid-gap energy. Although the argument presented above is for surface states, Inkson [49] showed that the properties of localised defects can similarly be understood in terms of the complex band structure. As ViGS are localised in real space they are extended in reciprocal space and consequently their character is dependent on the band structure throughout the BZ, making the theoretical calculation of the CNL demanding. Consequently several theoretical approaches have been developed to predict the location of the CNL. Mönch [50] used empirical tight-binding calculations to show a linear relationship between the branch-point energy and dielectric band gap with a least squares-fit obtaining a value of $0.449 \pm 0.007$ which is just below the mid-gap position and in agreement with the results of the 1D model above. Tersoff [51] developed a semi-empirical method to determine the average mid-gap energy as

$$\bar{E}_{mid} = \frac{1}{2}(\bar{E}_C + \bar{E}_V), \tag{1.1}$$

where $\bar{E}_V$ is the valence band maximum (VBM) excluding spin-orbit splitting and $\bar{E}_C$ is the indirect conduction band minimum (CBM) (i.e. excluding $\Gamma$). This approach gives a simple way to estimate the CNL position and is reasonably accurate for most materials.

The band lineup of a number of TCOs and conventional semiconductors relative to the CNL are shown in figure 1.4 (b). From the previous discussion it would seem that the CNL should lie within the band gap for most semiconductors, and this is the case for Si and GaAs, explaining the ability to dope these materials either $n$-type or $p$-type. However, in contrast to conventional semiconductors, metal oxides have a large size mismatch between the metal cation and the oxygen anion, and combined with the high electronegativity of oxygen [52, 53], this results in a band

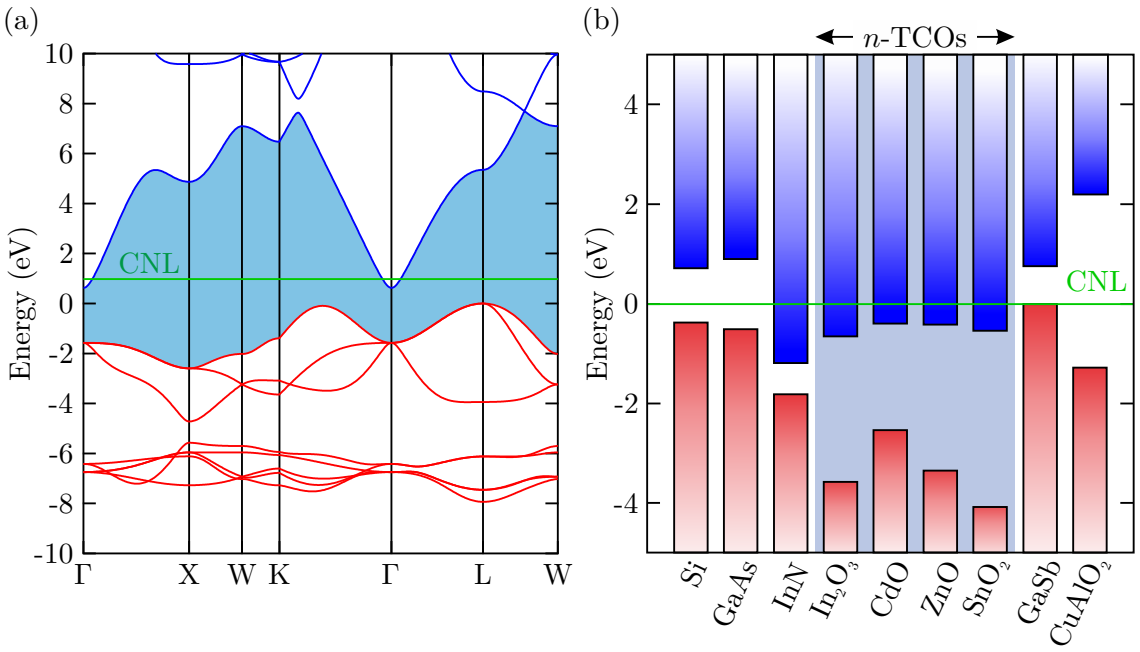


**Figure 1.4.** (a) Band gap corrected local density approximation (LDA) band structure of CdO. The VBs are shown in red and the CBs in blue, the band gap is indicated by the blue shading. The CNL is shown at 2.55 eV above the Γ VBM [54] which places it in the CB. (b) The band lineup of TCOs and other semiconductors relative to the CNL, figure adapted from [16] data from [54, 59–65].

structure with a single low lying CB at the Γ point. This can be seen in figure 1.4 (a) where the calculated CdO band structure is shown. This results in the CNL lying above the CBM in TCOs, explaining why TCOs typically show *n*-type conductivity despite no intentional doping, as any defects which form are likely to be donors. This idea has been explored in CdO both by high energy particle irradiation to induce defects, and by infusing hydrogen into the material [54–56]. The creation of these additional defects drives the Fermi level towards the CNL. The CNL concept is now thought to be widely applicable across different families of semiconductors [57], and has recently been used to explain the formation of a 2DEG at the surfaces of the topological insulators such as $Bi_2Se_3$ and $Bi_2Te_3$ [58].

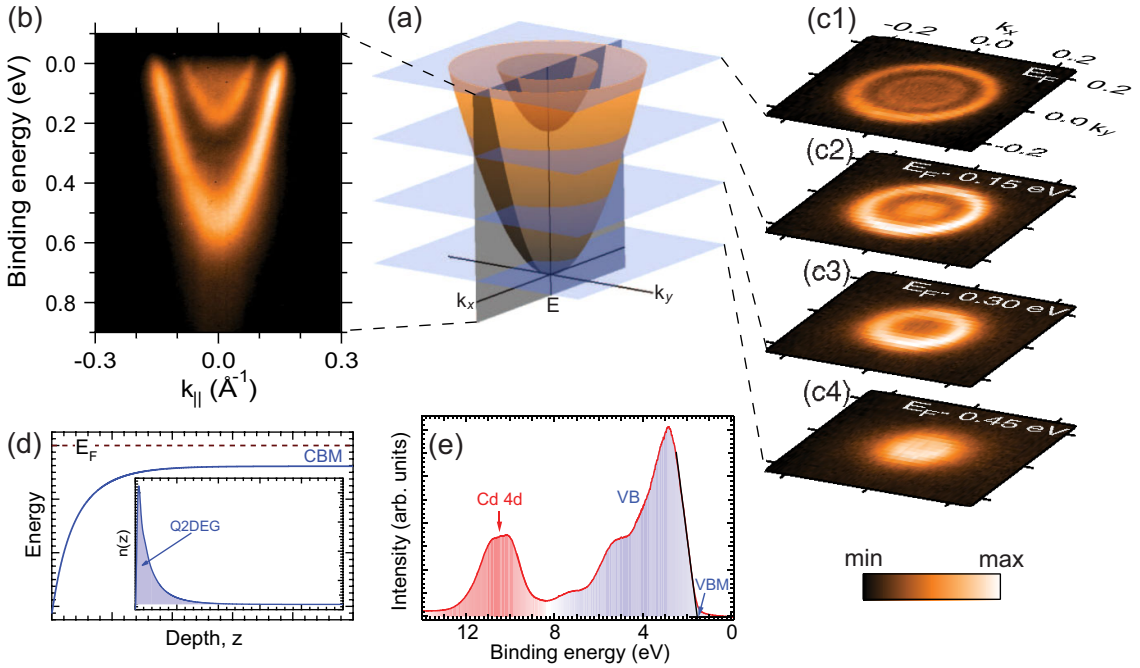


**Figure 1.5.** ARPES of CdO showing the subband states within the Q2DEG at the surface. (a) 3D schematic of the Q2DEG states, (b) $E$ vs $k_{||}$ dispersion of the subband states, (c) constant energy slices through the subbands. (d) Schematic of the downwards band bending, (e) angle integrated Cd $4d$ and VB spectra. Reproduced from reference [66].

### 1.4.1 Surface Electronic Properties

CdO exhibits interesting surface electronic properties, as discussed previously the CNL in CdO is above the CBM and is often significantly above the Fermi level. The creation of a surface therefore leads to the formation of intrinsic defects which are donors, and as the Fermi level is below the CNL some of these donor states will be unoccupied (i.e. positively charged). This charge necessitates the formation of a space-charge layer which screens this positive charge and so leads to charge neutrality. This results in an accumulation of electrons close to the surface, which occurs over a distance defined by the Thomas-Fermi screening length (typically $\sim 5$ nm), and this is discussed in more detail in section 3.2. This region of surface confined electron density is a 2DEG, and in the case of CdO this 2DEG is sufficiently confined to form quantised subband states, resulting in a quantised 2D electron gas (Q2DEG), as displayed in figure 1.5. This makes CdO an intriguing system with

which to study the properties of oxide 2DEGs. As the 2DEG forms intrinsically at the surface, it is more readily accessible to surface-sensitive experimental techniques than 2DEGs which form at buried interfaces (such as $LaAlO_3/SrTiO_3$). Additionally, it offers opportunities to modify the 2DEG by surface treatments and to observe their effects.

Finally, the electron accumulation and Q2DEG present at the CdO surface has only a minor influence over the electrical conductivity of thin films. However, with the recent developments of nanomaterials [67–69], the influence of the surface on the overall macroscopic electronic properties becomes crucial. In particular, the electronic properties of nanowires may be dominated by surface conduction and, for example, in gas sensors the surface electronic properties define the sensitivity of the device. For these reasons, a detailed understanding of the surface electronic properties of CdO, and other TCOs, is crucial for future device applications. To this end, obtaining a more detailed understanding of the electronic properties of CdO through the use of a variety of photoemission measurements is the subject of this thesis.

# CHAPTER 2

# Experimental Techniques

This chapter discusses the key experimental techniques employed throughout this thesis. In particular, the basics of photoelectron spectroscopy techniques (section 2.1) which are used throughout this thesis are discussed in detail. A description of the ultra high vacuum (UHV) photoemission systems used to obtain the data presented in this thesis at the University of Warwick (Coventry, UK), ISA (Aarhus, Denmark), and Diamond Light Source (Didcot, UK) is also given. The supporting techniques of Hall effect, for transport measurements (section 2.2), and low energy electron diffraction (LEED), used to check the surface periodicity (section 2.3) are also described.

## 2.1 Photoelectron Spectroscopy

The photoelectric effect, first discovered by H. R. Hertz in 1887 [70], provides the basis for a range of experimental techniques collectively known as photoelectron spectroscopy (PES). The effect was only fully explained by A. Einstien in 1905 by introducing the concept of photons [71], work for which he received the Nobel Prize for Physics in 1921. The modern technique of x-ray photoelectron spectroscopy (XPS) was founded by K. M. Siegbahn, earning him the Nobel Prize for Physics in 1981 [72]. He contributed to the design and development of a high resolution

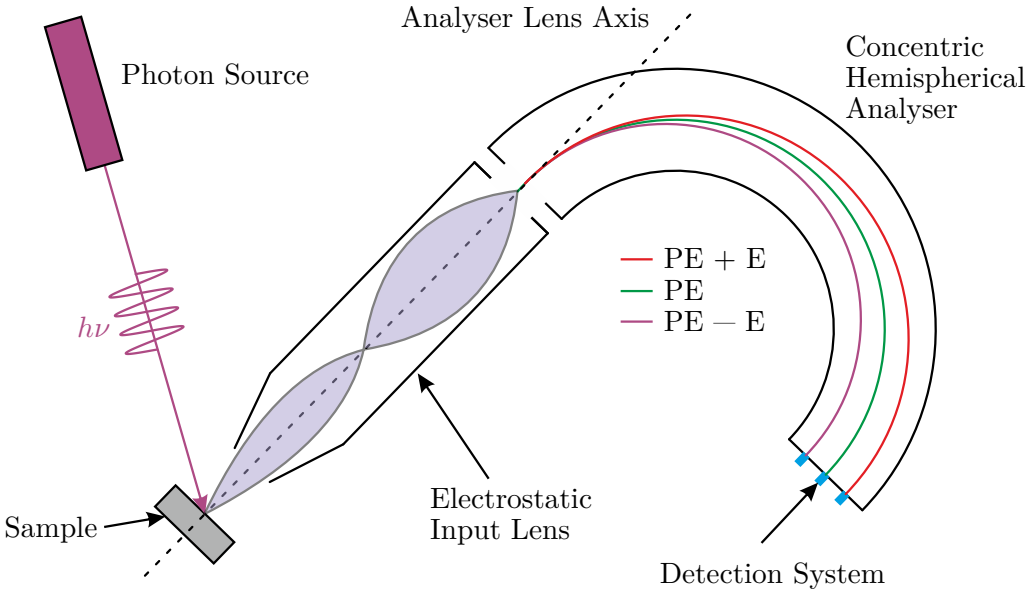


**Figure 2.1.** Schematic of a photoemission experiment. The key components are a photon source and a electron analyser. The electron analyser is made up of an electrostatic input lens, a hemisphere, and a detection system as discussed in the text.

x-ray source and electron analyser enabling the observation of core levels with resolvable chemical shifts, and giving the technique the alternative name of electron spectroscopy for chemical analysis (ESCA). This paved the way for photoemission to become one of the most successful techniques for the study of the chemical and electronic properties of materials, by allowing direct access to the density of states (DOS) at the surface.

The experimental setup for a typical photoemission experiment is shown in figure 2.1. The key components are a photon source and electron analyser. Dependent on the type of photoemission experiment the photon source can be a x-ray gun, gas discharge lamp, synchrotron or laser. Typically the photon source needs to have a line width of $< 1$ eV, as this limits the overall experimental resolution. There are a few different designs of electron analyser, however, only the concentric hemispherical analyser (CHA) is discussed here, as this is most commonly used in modern photoemission experiments, including those in this thesis. The electron analyser consists of an electrostatic input lens, a concentric hemisphere, and an

electron detection system. The design and voltages applied to the electrostatic input lens can be chosen to allow the electron analyser to be operated in different modes. These include defining the acceptance angle or area, or operating in an angle resolved mode for use with 2D detection. The lens includes an ability to accelerate or retard the electrons by a voltage ($R$), allowing a kinetic energy (KE) spectrum to be obtained. The hemisphere is used as an energy filter, so only electrons with the pass energy ($PE$) will pass along the central path of the hemisphere. However, electrons with differing energies ($PE \pm \delta E$) will be dispersed by the hemisphere leading to an energy distribution at the detector. This effect is exploited both to increase the count rate, with multiple channels, and to allow "single-shot" spectra to be taken. For 1D detection channeltrons are used, whereas for 2D detection a micro-channel plate (MCP) combined with a phosphor screen, or a delay line detector (DLD) can be used.

The photoemission process is shown schematically in figure 2.2. An incoming mono-energetic photon, which must have an energy ($h\nu$) greater than the work function of the sample ($\phi_{sample}$), excites an electron out of the sample, leaving behind a hole. As the electron leaves the sample it loses KE related to the work function of the sample. This results in the DOS of the sample being projected into the vacuum, from where it can be measured using an electron analyser. This simple picture of photoemission, i.e. the measured spectra directly reflects the sample's DOS, of course neglects several other important factors including many-body effects such as relaxation, photoionisation cross sections, and inelastic scattering. These effects are always present in a real experiment, but this simplified picture still serves as an intuitive view of the technique.

Although the data obtained from a photoemission experiment is the number of electrons emitted at each KE, it is often more convenient to display data on a binding energy scale as this removes several experimental factors, such as the photon energy and analyser work function, as can be seen in figure 2.2. KE and binding energy

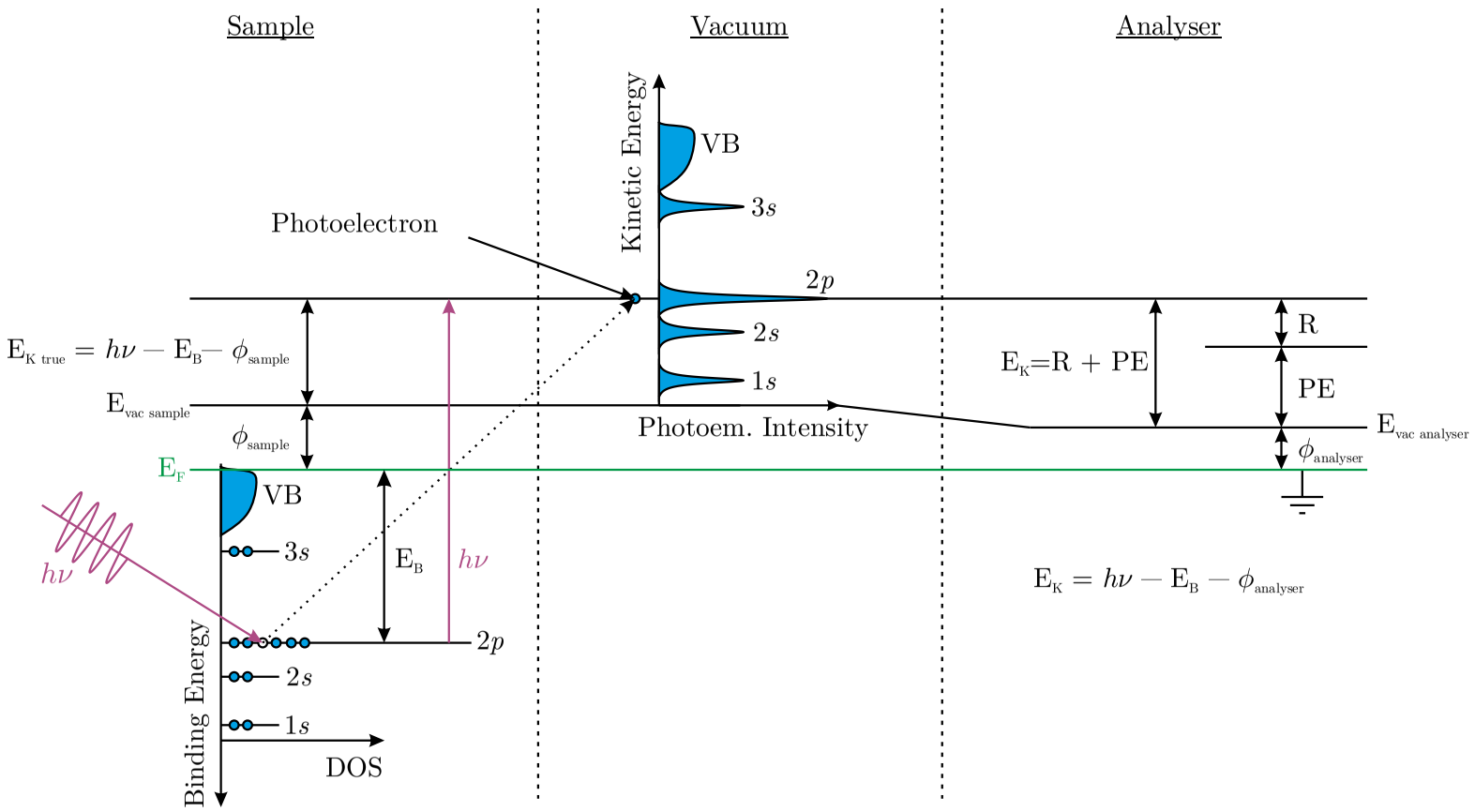


**Figure 2.2.** Schematic illustrating the electron energy levels in a photoemission experiment. An electron is excited from the sample by an incoming photon ($h\nu$) leaving a hole. It then travels through the vacuum to the electron analyser, where it is detected. Experimentally the Fermi level (FL) ($E_F$) of the sample and analyser are aligned by connecting both to ground. Figure inspired by [73–75].

(BE) can easily be converted using

$$E_K = h\nu - E_B - \phi_{analyser}, \tag{2.1}$$

where $h\nu$ is the energy of the incoming photon, $E_B$ is the binding energy of the electron, and $\phi_{analyser}$ is the work function of the analyser. This equation also illustrates that the technique is not dependent on knowing the work function of the sample, provided the system is calibrated. However, photoemission can be used to measure the work function of the sample by observing the low KE cut-off where electrons can only just escape from the sample [76]. Due to this equivalence photoemission data is commonly plotted with increasing KE or decreasing BE in the positive x direction.

The photoemission technique is divided into subsections dependent on the energy of the incident photons. For example, XPS uses x-rays as the incident photons (typically $h\nu \sim 1000$ eV) and is useful for looking at the strongly bound core electrons for elemental analysis. Ultraviolet photoelectron spectroscopy (UPS) utilises UV light (typically from gas discharge lines $h\nu < 50$ eV) and is useful for investigating the valence and weakly bound core electrons. The typical energy resolution of UPS is significantly higher than XPS making it better suited to investigation of the VB states. If the photon energy used is higher than available from typical lab x-ray sources ($h\nu > 2$ keV) the technique is commonly called hard x-ray photoelectron spectroscopy (HAXPES). This photoemission technique utilises an increased photoelectron inelastic mean free path (IMFP) (discussed further in section 2.1.3) obtained at higher energy to increase the probing depth and therefore obtain more bulk-like sensitivity. Further information can be obtained using these techniques if the photoelectron emission angle, in addition to the KE, is also measured. This technique is referred to as angle resolved photoelectron spectroscopy (ARPES) and is discussed further in section 2.1.5.

Photoemission techniques discussed here require UHV conditions, principally due to

the following factors:

- Photoemission is a surface sensitive technique, therefore a stable surface condition must be maintained for the duration required to make a photoemission measurement. Typical PES experiments are conducted over a few hours, therefore requiring pressures of $< 10^{-10}$ mbar.
- High voltages are required for both the generation of x-rays and the detection of electrons. An x-ray gun requires an anode voltage of 10 to 20 kV to accelerate electrons and generate a flux of x-rays. High voltages are required on the analyser lenses, hemisphere, and channeltrons/MCP/screen to deflect and detect electrons. These high voltages are typically applied across small gaps ($\sim$mm), therefore vacuum conditions are required to support these high electric field strengths without arcing.
- The electrons need to travel from the sample surface through the electron analyser without scattering from gas molecules. This requires electron mean free paths of the order of 1 m or a pressure of $< 10^{-6}$ mbar.

The requirements of UHV conditions are discussed further, with particular focus on the systems used to perform the experiments presented in this thesis, in sections 2.1.6, 2.1.7, and 2.1.8.

### 2.1.1 Core Levels

Core levels are one of the most prominent features of a survey photoemission spectrum, and each element produces a characteristic set of core level lines. Thus they provide a robust approach to the identification of elements present at the surface of the sample. In photoemission, core levels are labeled according to the spectroscopic convention $Xn\ell_j$, where $X$ is the elemental symbol, $n$ is the principle quantum number, $\ell$ is the orbital angular momentum quantum number label ($s = 0$, $p = 1$,

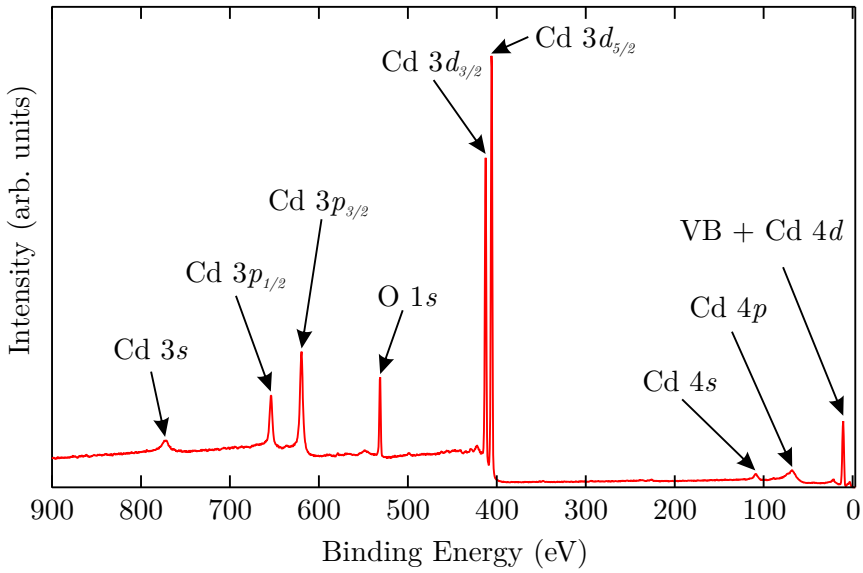


**Figure 2.3.** An example XPS survey spectra of a clean CdO surface, obtained at the Warwick XPS facility. The sample was illuminated by monochromated Al $K_\alpha$ ($h\nu$ = 1486.6 eV) radiation. An analyser angular acceptance of ±7° and a pass energy of 50 eV were employed.

$d = 2$, $f = 3$, ...), and $j$ is the total orbital angular momentum quantum number ($j = \left|\ell \pm \frac{1}{2}\right|$). This labeling scheme can be seen in the CdO survey spectrum shown in figure 2.3. For $s$ shells, $\ell = 0$ so $j$ only takes the value $\frac{1}{2}$ and is commonly omitted. For orbitals other than $s$, $j$ can take two possible values, due to spin-orbit splitting, resulting in the doublet peak structure commonly observed in photoemission spectra. The energy separation of a doublet ($\Delta E_{SO}$) is given by

$$\Delta E_{SO} \propto \xi(nl)[j(j+1) - \ell(\ell+1) - s(s+1)], \tag{2.2}$$

where $\xi(n\ell)$ is the spin-orbit coupling constant. After considering the background and experimental factors, the doublet intensity ratio should be given by the ratio of the relative degeneracy of the states $(2j+1)$.

$$I = \frac{2j_- + 1}{2j_+ + 1}. \tag{2.3}$$

Therefore, the intensity ratio for $p$, $d$, and $f$ doublets are $\frac{1}{2}$, $\frac{2}{3}$ and $\frac{3}{4}$, respectively.

### 2.1.2 Background

Photoemission spectra contain a background formed principally by inelastic scattering of photoelectrons. This effect is typically observed as a step-like increase in the baseline after passing through a core level peak. This can be observed on the Cd $3d$ and Cd $3p$ peaks in figure 2.3. In order to perform a qualitative elemental analysis, peak shape analysis, or a comparison to a theoretical DOS, background subtraction must be performed. The most commonly applied backgrounds are linear, Shirley [77] or Tougaard [78]. The Shirley background is calculated iteratively depending on the integral of the spectrum at lower binding energy, and a constant parameter is then adjusted to align the ends of the background with the data at points chosen to enclose the feature of interest. This results in a step-like background and is the approach used throughout this thesis.

### 2.1.3 Inelastic Mean Free Path

The surface sensitivity of photoemission experiments is due to the short escape depth of photoelectrons, typically $< 10$ nm, which arises from the short inelastic mean free path (IMFP) of electrons in solids. This is illustrated by the "universal curve" in figure 2.4. As can be seen, an electron with a KE of $\sim 70$ eV has an IMFP of $\lesssim 10$ Å or $\sim 3$ atomic layers, therefore an observed electron which has not undergone an inelastic scattering event, must have originated from the top few atomic layers.

The universal curve suggests two possible approaches to increase the depth probed by a photoemission experiment. These approaches are to utilise either extremely low or relatively high KE electrons, both of which are areas of current research interest in photoemission [79, 80]. The most promising approach to the low KE range is laser-ARPES [81], with photon energies $\sim 6$ eV which provide the additional advantages of exceptionally high energy and momentum resolution [82, 83]. The alternative approach is to move to the higher KE range, as employed by hard x-ray photoelectron spectroscopy (HAXPES) [84, 85]. This approach is used in chapter 4

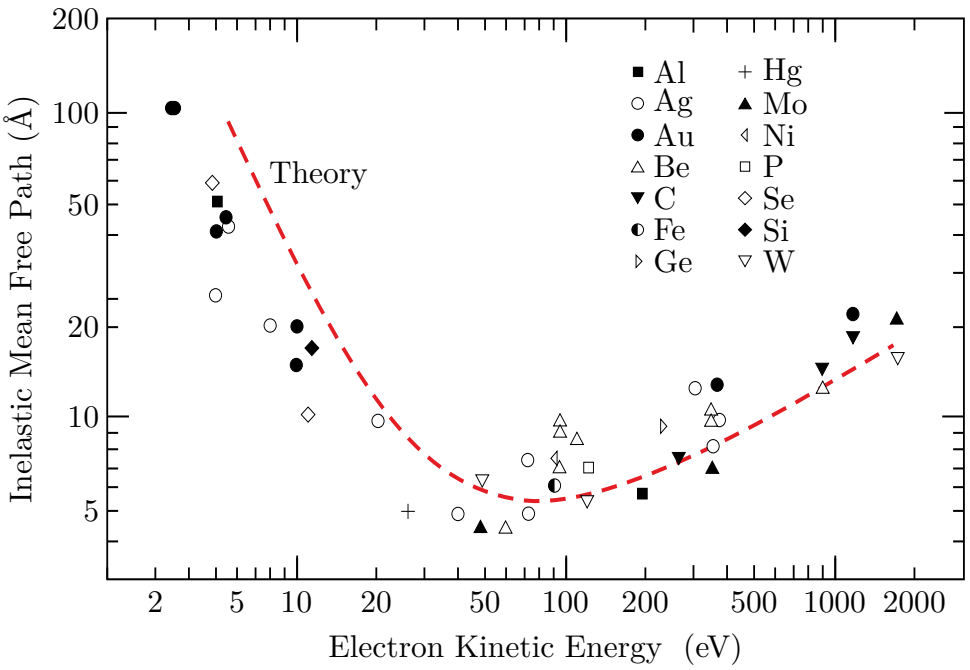


**Figure 2.4.** The inelastic mean free path (IMFP) of electrons in solids as a function of their KE, known as the universal curve. The points are experimental data and the curve is a theory fit. Note the log-log scale. Adapted from [73, 86, 87].

where the surface sensitivity of the technique is investigated in more detail.

Although the universal curve qualitatively explains the surface sensitivity of photoemission techniques it can be seen that not all the experimental data fit on the curve. Additionally it is common to measure compounds as well as elements, and therefore more advanced models have been developed to predict the IMFP of electrons in a wide range of materials. One of these approaches is TPP-2M which is described in section 2.1.3.1.

#### 2.1.3.1 The TPP-2M Approach

A commonly adopted approach to calculating the IMFP for photoemission analysis is the semi-empirical TPP-2M formula [88]. This is the second modification of a formula proposed by Tanuma, Powell and Penn for the calculation of IMFP [89]. The functional form of the expression is a modified Bethe equation

$$\lambda_{IMFP} = \frac{E_K}{E_P^2 \left[\beta \ln(\gamma E_K) - C E_K^{-1} + D E_K^{-2}\right]}, \tag{2.4}$$

where $E_K$ is the outgoing photoelectron KE in eV. $E_P$ is the free electron plasmon energy in eV given by

$$E_P = 28.8\sqrt{N_V \rho / M}, \tag{2.5}$$

where $N_V$ is the number of valence electrons per atom, $M$ is the atomic or molecular mass in g/mol, and $\rho$ is the material density in g/cm$^3$. This leaves $\beta, \gamma, C$ and $D$ as free parameters which are set by the following empirically derived relations

$$\beta = -0.10 + 0.944(E_P^2 + E_G^2)^{-1/2} + 0.069\rho^{0.1}, \tag{2.6}$$

$$\gamma = 0.191\rho^{-1/2}, \tag{2.7}$$

$$C = 1.97 - 0.91U, \tag{2.8}$$

$$D = 53.4 - 20.8U, \tag{2.9}$$

with

$$U = \frac{N_V \rho}{M} = \frac{E_P^2}{829.4}, \tag{2.10}$$

where $E_G$ is the band gap in eV, for insulators and semiconductors. This formula can be applied to elements, inorganic and organic materials, and is typically accurate to within 10% [90]. The TPP-2M formula has been used to calculate all IMFPs used throughout this thesis.

### 2.1.4 Photoionisation Cross-Sections

To perform quantitative analysis of photoemission spectra, it is necessary to know the probability of a specific photoemission event occurring, which is described by the photoionisation cross-section. The photoemission process can be described by optical absorption of the incoming photon which promotes an electron from an occupied initial state to an unoccupied final state, when this final state is significantly above the Fermi level it can be approximated by a free electron state, with a large DOS. The joint density of states therefore depends only on the occupation if the initial state which for core levels depends only on the elemental electron configuration,

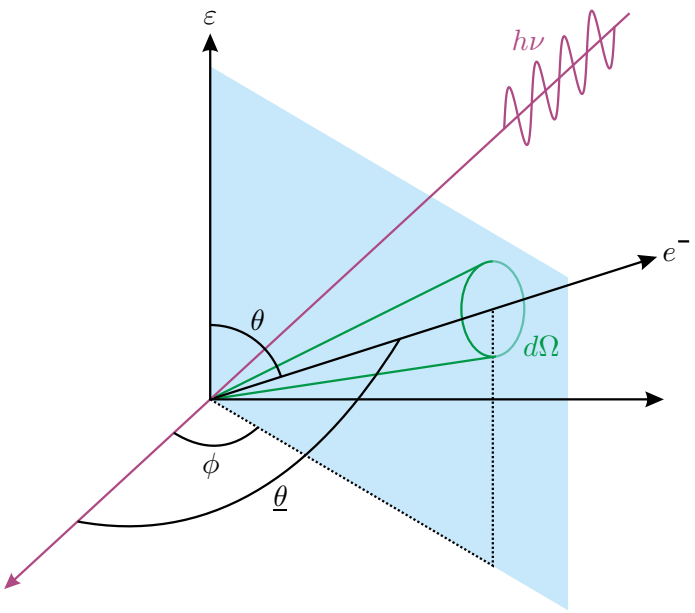


**Figure 2.5.** Schematic showing the geometry relevant for applying photoionisation asymmetry corrections, the key directions are labeled as: the photoelectron emission direction ($e^-$), the solid angle of electron collection ($d\Omega$), and the photon polarization vector ($\varepsilon$) (in the case of linear polarization). The angles are labeled as: the angle between the polarisation vector and the electron emission direction ($\theta$), the angle between the photon propagation direction and the plane containing both the electron emission direction and the electric polarization vector (blue plane) ($\phi$), the angle between the photon propagation direction and the photoelectron emission direction ($\underline{\theta}$), relevant for unpolarised or circularly polarized light. Figure adapted from [91].

allowing cross-sections to be calculated and tabulated which are independent of the bonding environment. Photoemission is further complicated by the anisotropic nature of photoemission events, resulting in a geometrical dependence on the number of photoelectrons emitted, which is characterised by asymmetry parameters. Accounting for these asymmetry effects is more complex than the cross-sections, as the geometry of the experiment needs to be considered, illustrated in figure 2.5.

For linearly polarised photons, the photoelectron angular distribution can be written as [92]

$$\frac{d\sigma_i}{d\Omega} = \frac{\sigma_i}{4\pi}\left[1 + \underbrace{\beta P_2(\cos\theta)}_{\text{dipolar}} + \underbrace{(\delta + \gamma\cos^2\theta)\sin\theta\cos\phi}_{\text{non-dipolar}}\right], \tag{2.11}$$

whereas for unpolarised or circularly polarized photons the expression is

$$\frac{d\sigma_i}{d\Omega} = \frac{\sigma_i}{4\pi}\left[1 - \underbrace{\frac{\beta}{2}P_2(\cos\underline{\theta})}_{\text{dipolar}} + \underbrace{\left(\frac{\gamma}{2}\sin^2\underline{\theta} + \delta\right)\cos\underline{\theta}}_{\text{non-dipolar}}\right]. \tag{2.12}$$

Here $P_2$ is the second order Legendre polynomial

$$P_2(x) = \frac{1}{2}(3x^2 - 1), \tag{2.13}$$

and the angles $(\phi, \theta, \underline{\theta})$ are defined in figure 2.5. $\frac{d\sigma_i}{d\Omega}$ is the differential cross-section, $\sigma_i$ is the photoionisation cross-section, $\beta$ is the dipole asymmetry parameter, $\gamma$ and $\delta$ are non-dipolar asymmetry parameters. In the case of a typical lab XPS experiment, where an unpolarised source is used and the photon energies are quite low, which allows the dipole approximation to be sufficient ($\gamma \approx \delta \approx 0$) equation 2.12 can be simplified to

$$\frac{d\sigma_i}{d\Omega} = \frac{\sigma_i}{4\pi}\left[1 - \frac{\beta}{4}(3\cos^2\underline{\theta} - 1)\right]. \tag{2.14}$$

In this case the asymmetry correction is only dependent on the angle between the photon propagation direction and the electron emission direction $\underline{\theta}$ in figure 2.5.

Photoionisation cross-sections and asymmetry parameters have been calculated, within certain approximations, and tabulated. Sources of these cross-sections and asymmetry parameters, including those used in this thesis, are given in table 2.1. The Yeh and Lindau cross-sections [93] are calculated using the Hartree-Fock-Slater one-electron central potential model, from which they present the photoionisation cross-section and dipole asymmetry parameters. This includes data at specific energies relevant for discrete line sources (H, $\mathrm{Ne_{I,II}}$, $\mathrm{He_{I,II}}$, Y $\mathrm{M}_\zeta$, Zr $\mathrm{M}_\zeta$, Na $\mathrm{K}_\alpha$, Mg $\mathrm{K}_\alpha$, Al $\mathrm{K}_\alpha$, Cu $\mathrm{K}_\alpha$). The Scofield cross-sections [94, 95] extend the approach of Yeh and Lindau by performing relativistic calculations, and significantly extending the energy range. The cross-sections are presented for the most commonly used lab sources, and up to extremely high energy. More recently Trzhaskovskaya has published a

**Table 2.1.** Tabulated sources of photoionisation and asymmetry parameters.

| Reference | Elements | Photon energies (eV) | Asymmetry |
|---|---|---|---|
| Yeh and Lindau [93] | $Z \leq 103$ | $10.2 \leq h\nu \leq 8047.8$ | Dipole |
| Scofield [94] | $Z \leq 96$ | $h\nu = 1254, 1486$ | None |
| Scofield [95] | $Z \leq 101$ | $1000 \leq h\nu \leq 1500000$ | None |
| Trzhaskovskaya et al. [91, 96, 97] | $Z \leq 100$ | $100 \leq h\nu \leq 10000$ | Quadrupole |

series of papers [91, 96, 97] of particular interest as they cover the energy range of most photoemission experiments, including HAXPES, and also include non-dipolar asymmetry parameters which are increasingly important at higher photon energies.

### 2.1.5 Angle Resolved Photoelectron Spectroscopy

Angle resolved photoelectron spectroscopy (ARPES) can be seen as an extension to conventional (or angle integrated) photoemission, where the emission angle of the photoelectrons is recorded in addition to their KE. This allows additional information about the momentum of electrons inside the sample to be obtained. A schematic of an ARPES experiment is shown in figure 2.6, where the blue segment illustrates a range of emission angles which can be recorded simultaneously using an angle resolving analyser with 2D detection. Additionally, the sample can then be moved either in $\theta$ to access higher angles/momentum, or in $\beta$ or $\phi$ to allow a 3D map (intensity as a function of KE and two angles) to be obtained. Most ARPES experiments are conducted in the UV energy range ($h\nu < 100$ eV) as the photoionisation cross-sections associated with the VB are typically much higher at low energies, dramatically enhancing the number of photoelectrons. Additionally, the momentum resolution of an ARPES experiment is defined as

$$\Delta k_{||} = \sqrt{\frac{2m_e E_K}{\hbar^2}} \cos(\theta) \Delta\theta, \tag{2.15}$$

where $\Delta\theta$ is the angular resolution of the electron analyser [98]. Examination of this equation shows it is possible to achieve higher momentum resolution when working at low energies. Despite the advantages of low phonon energies, there has been some

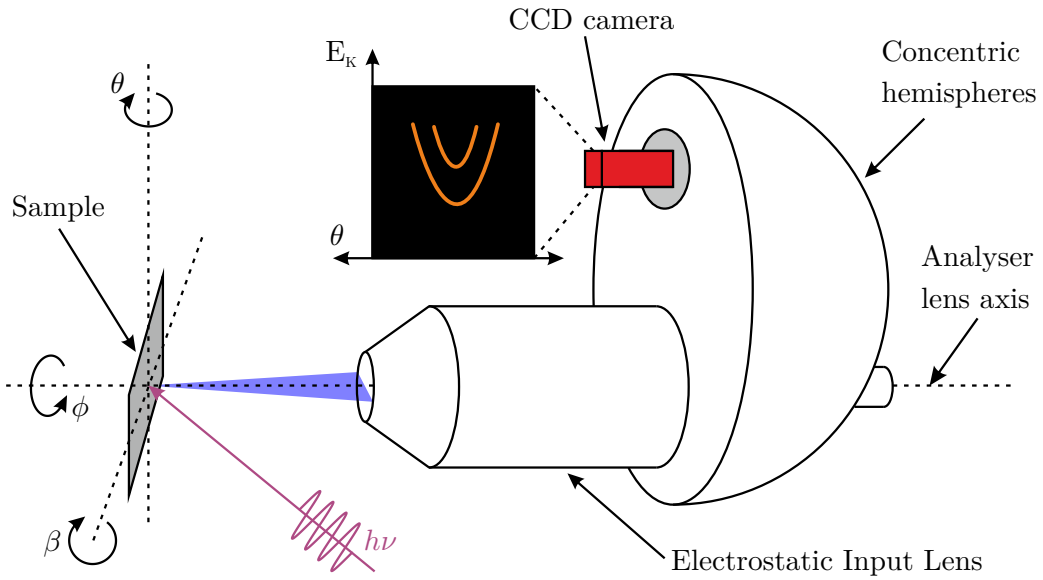


**Figure 2.6.** Schematic of an angle resolved photoelectron spectroscopy (ARPES) experiment, showing how the angles can be varied to allow an angle resolved measurement to be made. The blue segment illustrates the range of emission angles which can be recorded simultaneously with a 2D detector.

recent progress in performing ARPES at high photon energies in order to achieve enhanced bulk sensitivity [99, 100].

In an ARPES experiment, photoemission intensity spectra are recorded as a function of angle and KE. However, to allow for comparison to theoretical calculations, and to extract meaningful physical parameters, transforming the data into a function of wavevector ($\boldsymbol{k}$) and BE is required, a process known as "$k$-warping". Due to the breaking of the crystal symmetry imposed by the surface, $k_\perp$ is not conserved by the photoemission process. This makes ARPES particulary well suited to studying 2D electronic systems, such as the quantised 2D electron gas (Q2DEG) investigated in chapter 6. ARPES can be used to probe 3D electronic states such as the band structure but some additional assumptions need to be made regarding the electron final state (commonly free electron final states are assumed), and knowledge of the inner potential of the material is required (or can be extracted for a large enough data set). $k$-warping including $k_\perp$ is therefore not discussed here as it is beyond the scope of this thesis, however, excellent discussions can be found in references [73, 76, 101]. Returning to 2D electronic systems, as both $k_{||}$ and energy are conserved by the

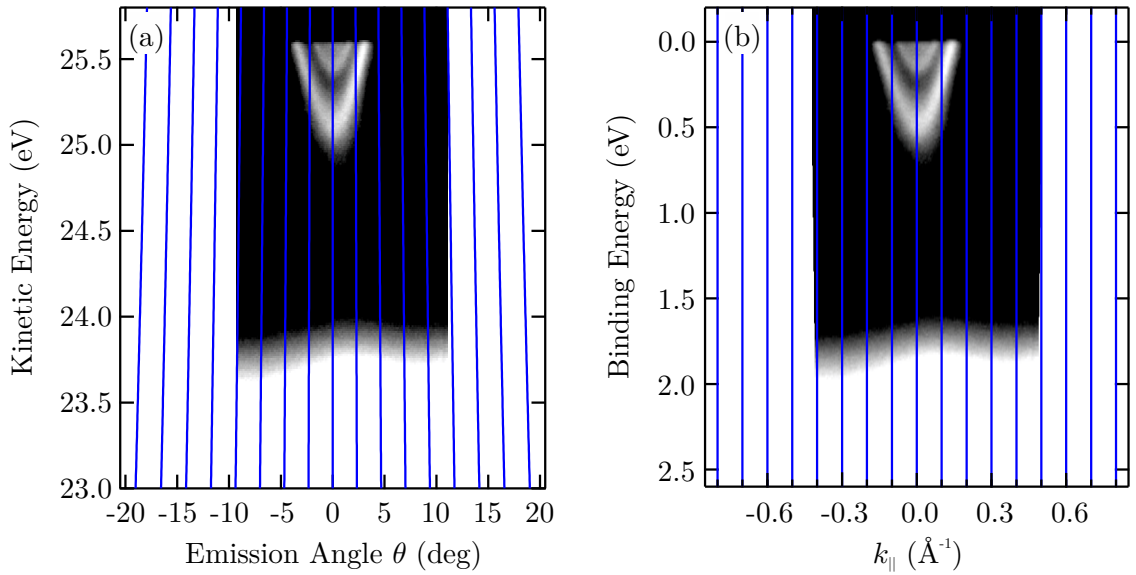


**Figure 2.7.** Example of $k$-warping of a 2D data set, obtained from a clean CdO surface with a photon energy of 30 eV. Emission angles exceeding the data are shown to allow the effects of the $k$-warping to be more clearly visible. (a) ARPES data set before $k$-warping, intensity (shown by the colour scale, black low intensity, white high intensity) as a function of KE and emission angle ($\theta$). (b) the same data set shown after $k$-warping and conversion to BE, intensity as a function of BE and momentum ($k_{||}$). The blue lines are contours of constant momentum at 0.1 Å$^{-1}$ intervals, note they are not parallel in (a).

photoemission process, parallel momentum can be calculated from the emission angle and KE by the relation

$$k_{||} = \sin(\theta)|\boldsymbol{k}| = \sin(\theta)\sqrt{\frac{2m_e E_K}{\hbar^2}}, \tag{2.16}$$

where $\theta$ is the electron emission angle with respect to the surface normal [73]. By geometry this can be extended to allow 3D data sets (of 2D electronic states) to be $k$-warped resulting in a data set of $I(k_x, k_y, BE)$. Constant energy slices, such as the Fermi surface, can then be obtained from this 3D data set. An example of $k$-warping of a 2D data set is shown in figure 2.7, where constant momentum contours are indicated by the blue lines. The $k$-warping process takes the angular data which are non-linear in momentum and interpolates onto a new grid which is linear in momentum. As the subband features investigated in this thesis are very close to normal emission, the effect of performing $k$-warping causes only a minor distortion of

the bands. In practice, $k$-warping is performed using an computer algorithm which calculates a mesh using equation 2.16, and then interpolates the original data onto the new mesh. Throughout this thesis the Igor Pro (Wavemetrics, Inc.) software was used for this purpose.

### 2.1.6 University of Warwick Photoemission System

The University of Warwick photoemission system consists of three connected UHV chambers, for sample preparation, XPS and ARPES as shown in figure 2.8. The system was manufactured by Omicron Nanotechnology GmbH. The three chambers are connected with a UHV sample transfer system to allow easy exchange and storage of multiple samples. The base pressure of the system is $< 3 \times 10^{-11}$ mbar, measured using Bayard-Alpert type ionisation gauges, and is achieved using a combination of turbomolecular, sputter ion and titanium sublimation pumps (TSPs). The system is equipped with bakeout cases and automated bakeout controllers, allowing the system to be baked at 120 °C for several days to achieve UHV conditions.

The preparation chamber is equipped with a sample manipulator for heating up to $\sim$ 900 °C, a three cell UHV evaporator (Omicron Triple EFM), and a thermal gas cracker (Oxford Research TC 50) to allow in-situ sample cleaning and controlled deposition. A low energy ion gun (LK Technologies NGI 3000) is also attached to the chamber enabling sample cleaning via ion bombardment and annealing. Connected to the preparation chamber is a fast entry lock (FEL) which allows samples to be loaded into UHV conditions in $\sim$ 1.5 hours. A 12 sample storage carousel is located between the preparation and XPS chambers to allow samples to be stored in vacuum. The system also includes a vacuum suitcase allowing in vacuum transfer of samples to other chambers at pressures $< 1 \times 10^{-9}$ mbar. This allows complementary techniques to be used while maintaining the current sample surface condition.

The XPS capabilities of the system are delivered by a monochromated Al $K_\alpha$ x-ray source ($h\nu$ = 1486.6 eV, Omicron XM 1000), coupled to an Omicron Sphera

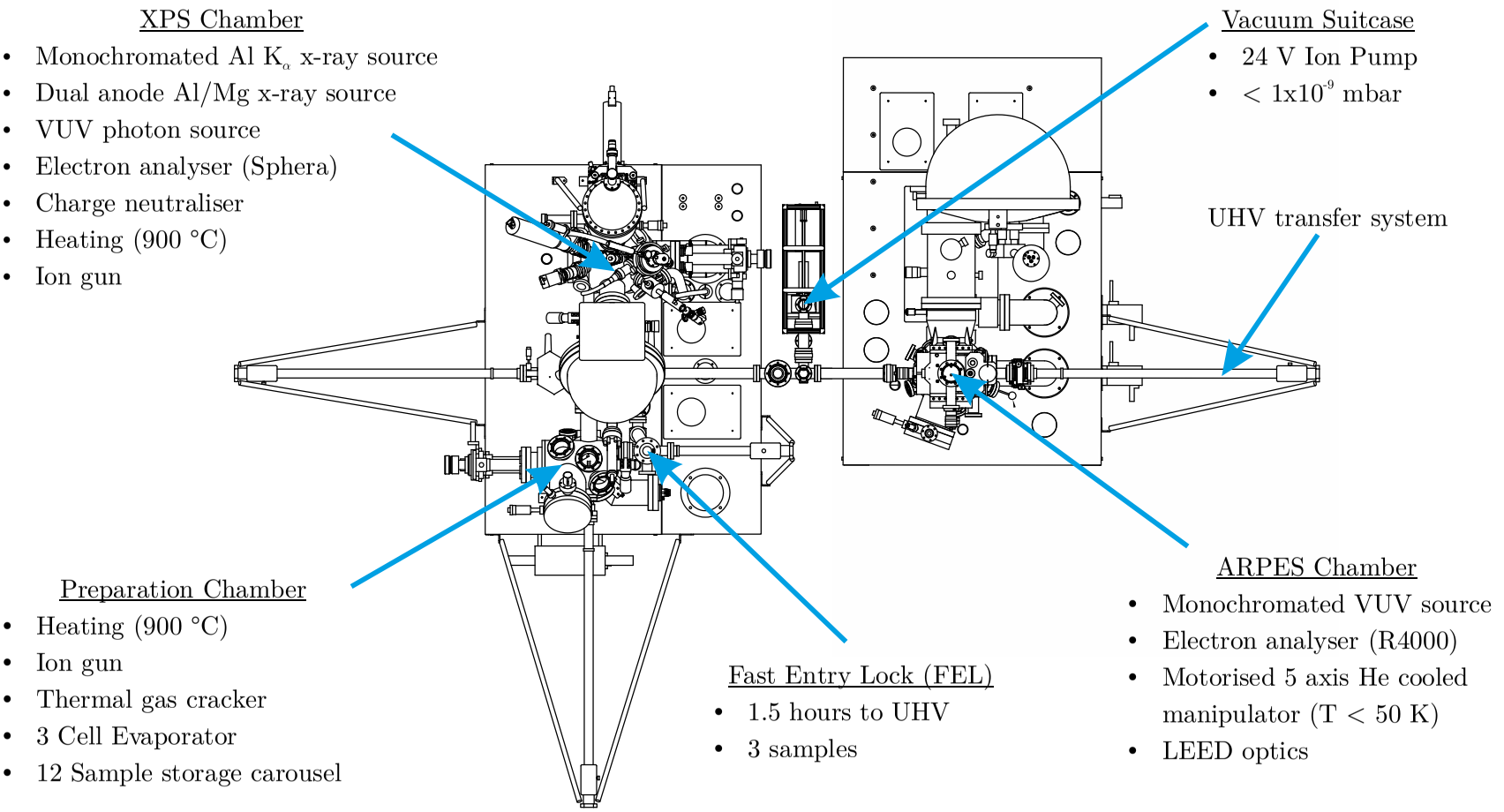


**Figure 2.8.** Technical drawing of the Warwick photoemission system, with the key chambers and components labeled. Some supporting framework has been omitted for clarity. Adapted from Omicron GmbH technical drawings.

electron analyser, with a source-to-analyser angle of 80°. The XM 1000 x-ray source can be operated at up to 600 W in either focused or de-focused modes, giving spot sizes on the sample of 1 mm × 2 mm and 2 mm × 5 mm respectively. The focused mode is most commonly used as it delivers a higher flux density into a spot size approximately matched to the spatial acceptance of the analyser. The x-ray source is monochromated by diffraction from the $(10\bar{1}0)$ face of quartz crystals arranged on a 500 mm Roland Circle, resulting in a photon line width of $\sim 0.25$ eV free from x-ray satellites.

The Omicron Sphera hemispherical electron analyser has a radius 125 mm and is equipped with a focused lens system to enable analysis of small areas down to 60 $\mu m$. For routine analysis it is operated with an spatial acceptance of $\varnothing = 1.4$ mm, approximately matched to the source illuminated area. The detector consists of 7 channeltrons which are optically coupled to the counting electronics. The analyser is normally operated in constant analyser energy (CAE) mode to give consistent energy resolution across the KE range. A pass energy of 50 eV is typically used for recording a survey spectrum, achieving an overall energy resolution of $\sim 1.5$ eV. For detailed core-level and VB spectra, a pass energy of 10 eV is typically used providing an overall energy resolution of $< 0.5$ eV. The energy scale of the spectrometer is regularly calibrated with a sputter cleaned polycrystalline silver sample, this is done by measuring the position of the Fermi edge (FE), and additionally checked with the positions of Ag, Au and Cu core-levels.

In addition to the XPS capabilities, the analysis chamber includes a differentially pumped ion gun (Omicron FIG 05) to enable sample preparation and XPS depth profiling. A gas discharge lamp (Omicron HIS 13) is also attached allows for UPS to be performed alongside XPS, and obtain detailed VB spectra or work function measurements. A low energy electron flood gun (Omicron CN 10) can be used to avoid sample charging when measuring insulating samples, and works by providing a beam of low energy electrons to neutralise the sample surface. The 5-axis sample

manipulator allows for heating up to 900 °C or biasing of the sample.

The ARPES chamber includes a monochromated high intensity vacuum ultraviolet (VUV) source (VG Scienta VUV 5K), allowing the sample to be illuminated by either He I$\alpha$ (21.2 eV) or He II$\alpha$ (40.8 eV) photons. The He plasma is generated by electron cyclotron resonance (ECR) driven by microwaves, this results in a photon flux $\sim$ 500 times higher than a conventional VUV discharge lamp. The VUV light is focused on to the sample by a capillary resulting in a spot size $\sim$ 0.5 mm. The VUV source is differentially pumped allowing operating chamber pressures below $5 \times 10^{-10}$ mbar. The photoelectrons are detected by an angle resolving analyser (VG Scienta R4000) with 2D detection, allowing an angular range of $\pm 15°$ to be recorded simultaneously. The 5-axis manipulator includes motorized polar and azimuthal rotations to allow automated 3D ARPES maps to be collected. The manipulator includes liquid nitrogen or liquid helium cooling, allowing sample temperatures of $< 50$ K to be acheived. The ARPES chamber also features a LEED optic (Omicron SpectaLEED), which not only allows the periodicity of the sample to be observed, but also acts as a tool for performing alignment along principle azimuthal directions prior to obtaining ARPES data.

### 2.1.7 SGM-3 Aarhus ISA

ARPES experiments were performed on the SGM-3 beamline of the ASTRID synchrotron radiation source in Aarhus, Denmark. The synchrotron is a 40 m circumference, 580 MeV storage ring consisting of four bending magnets and one undulator [103, 104]. The SGM-3 beamline provides photons in the energy range of 16 eV to 130 eV, and a schematic of the beamline optics is shown in figure 2.9 [102]. The photon beam is monochromated using one of three spherical gratings chosen depending on the photon energy required. For photon energies below 32 eV the low energy grating (LEG) is used, in the range $30 < h\nu < 60$ eV the medium energy grating (MEG) is chosen, and above 60 eV the high energy grating (HEG) is used. As the synchrotron and beam optics are not optimised for small spot sizes, which

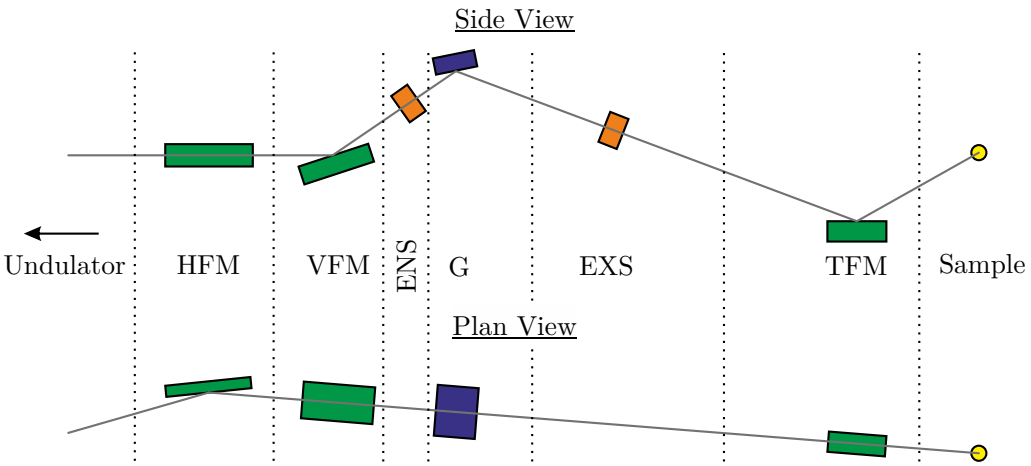


**Figure 2.9.** The layout of the beamline optics at SGM-3 beamline of ASTRID 1, ISA (Aarhus, Denmark). The key optical components are labeled as follows, horizontal focusing mirror (HFM), vertical focusing mirror (VFM), entrance slit (ENS), grating (G), exit slit (EXS), and a toroidal focusing mirror (TFM). Figure adapted from [102].

are desirable to obtain high angular resolution, the beam is passed through a pinhole inside the endstation, resulting in a spot size of $< 0.5$ mm.

The photoelectrons emitted by the sample are collected by a SPECS Phoibos 150 electron analyser, equipped with a 2D detector. This configuration allows simultaneous detection of a range of emission angles up to $\pm 13°$. The analyser slit is parallel to the polar rotation axis of the manipulator, which is motorised allowing automated collection of 3D ARPES maps. The sample is mounted on a four degrees of freedom manipulator, which is cooled with a closed circuit liquid helium cryostat maintaining a constant sample temperature of $\sim$ 70 K. Control of the beamline energy is also fully integrated allowing automatic collection of photon energy scans. For further information regarding the beamline design and performance, see reference [102].

The UHV endstation is pumped using a combination of turbo molecular pumps, ion pumps and TSPs, and following baking achieves a base pressure of $< 1 \times 10^{-10}$ mbar. In addition to the PES capabilities, the endstation offers conventional surface science facilities including sample heating, ion bombardment, gas dosing, evaporation sources and alkali metal sources. Complementary analytical techniques available include LEED and Auger electron spectroscopy (AES).

### 2.1.8 I09 of Diamond Light Source

The experiments discussed in chapters 4 and 5 were conducted at the I09 beamline of the Diamond Light Source (DLS), Oxfordshire, UK. The DLS is a third generation 3 GeV synchrotron, 561.6 m in circumference and hosts $\sim$ 30 separate beamlines providing a wide range of experimental techniques. The I09 beamline, opened in 2013, uniquely offers both hard and soft x-rays photons onto the same sample focus, while providing an incident photon energy range of 230 eV to 18 keV, with a choice of polarization. This allows a wide variety of different types of experiments to be performed, and within photoemission the possibilities are; XPS, HAXPES, soft and hard x-ray ARPES, photoelectron diffraction (PhD, XPD) and resonant photoemission.

The optical layout of the beamline at I09 is shown in figure 2.10, the hard and soft x-rays are generated by two undulators canted by 1.3 mrad. The hard x-ray optics feature a silicon double crystal monochromator (DCM), which provides an energy resolution of $\Delta E \sim 1$ eV. An additional silicon channel-cut high resolution monochromator can also be used, improving the energy resolution to $\Delta E \sim 50$ meV. The soft x-ray optics utilises a standard plane grating monochromator (PGM), offering an energy resolution of $< 300$ meV in the photon energy range 230 eV to 2 keV.

The photoelectrons emitted from the sample are detected using a VG Scienta EW4000 electron spectrometer equipped with a 2D detector. This spectrometer can operate at KEs up to 10 keV and has a very wide angle lens ($\pm 30^\circ$), allowing efficient collection of electrons. This is important in the hard x-ray regime, where the photoionisation cross-sections are typically much smaller [95, 97]. The lens system can also be operated in an angle resolved mode allowing take-off angle (TOA) XPS or ARPES to be performed. The energy resolution of the spectrometer is $< 30$ meV for all KEs, which when combined with the beamline and sample

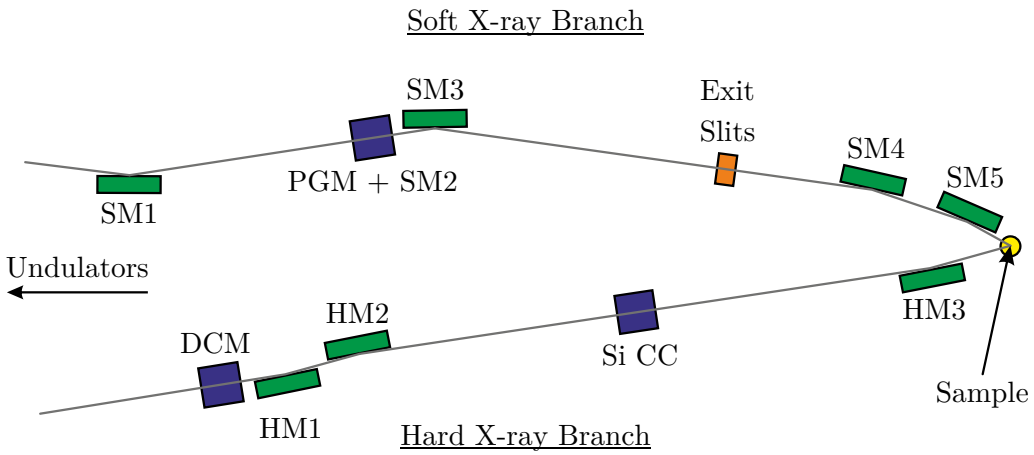


**Figure 2.10.** Simplified plan view schematic of the beamline optics at I09, DLS. The hard and soft beams are both focused onto the sample at the focus of the electron analyser in the end station. Key optical components are labeled, including; soft and hard mirrors (SM, HM), the monochromators, plane grating for soft x-rays (PGM) and a double crystal (DCM) followed by a Si channel cut (Si CC) for hard x-rays.

temperature allows total experimental energy resolutions of $<$ 100 meV to be achieved.

The endstation is pumped with a combination of turbomolecular, sputter ion, and sublimation pumps, which combined with baking achieve UHV conditions. In addition to hard and soft x-ray beams, the endstation has a monochromated VUV source to allow offline UPS/ARPES measurements to be performed. The endstation also provides all standard surface science facilities including: a fast entry lock, ion bombardment, sample heating, gas dosing, evaporation cells, mass spectrometers and LEED optics.

The experimental geometry at I09 is shown in figure 2.11. The incident photon beam is perpendicular to the analyser axis, which allows a grazing incidence geometry to be used. Grazing incidence is beneficial in HAXPES as it allows the beam footprint to be matched to the analyser acceptance area, significantly increasing the data acquisition rate.

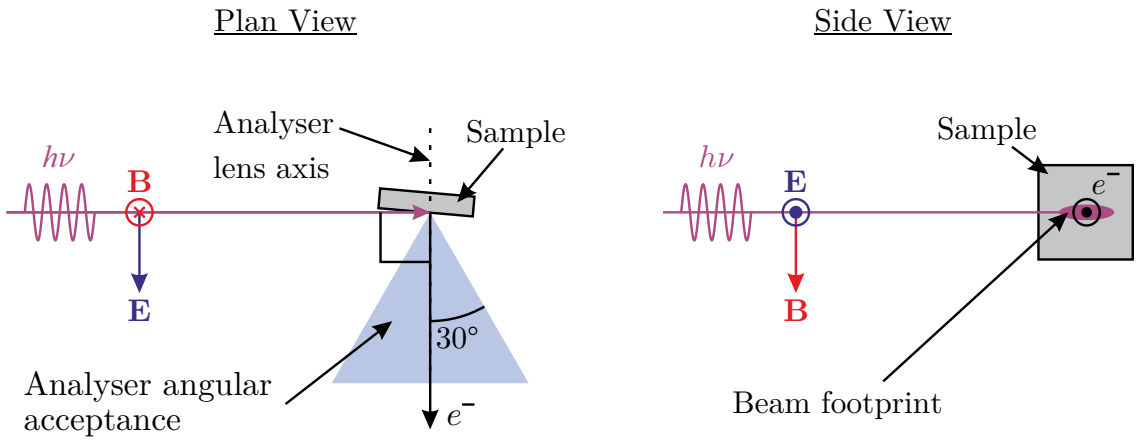


**Figure 2.11.** The experimental geometry at I09 in the case of linear horizontal polarisation. The plan view shows the sample placed in a grazing incidence geometry. The analyser ±30° angular acceptance is shown by the blue slice. The beam footprint in the side view is exaggerated to illustrate the effects of grazing incidence. The analyser lens axis is perpendicular to the photon beam, and the electric field vector is parallel with the analyser lens axis.

## 2.2 Hall Effect Measurements

The Hall effect was discovered by E.H. Hall in 1879 [105] and has become one of the most widely used characterisation techniques to investigate the electrical transport properties of materials, as well as finding many applications in magnetic sensors [106]. Principally, Hall effect measurements are used to obtain the bulk carrier concentration and mobility of a material. A schematic of a typical Hall effect experiment is shown in figure 2.12. When a current flows through a material placed in a magnetic field, a force is generated on the carriers perpendicular to both the magnetic field and the direction of current flow due to the Lorentz force ($\mathbf{F}$)

$$\mathbf{F} = q(\mathbf{E} + \mathbf{v} \times \mathbf{B}), \tag{2.17}$$

where $q$ is the charge, $\mathbf{E}$ is the electric field, $\mathbf{v}$ is the velocity and $\mathbf{B}$ is the magnetic field. The Lorentz force causes carriers to drift in the $y$ direction, but once they reach the edge of the sample they can no longer flow, and accumulate at the edges. This continues until the build up of charge generates an electric field opposing this,

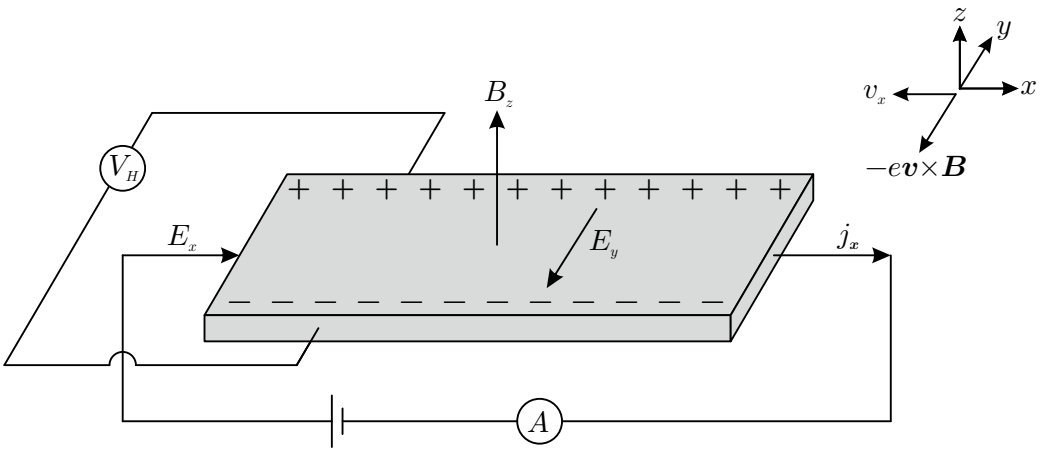


**Figure 2.12.** Schematic showing the Hall effect using the Hall bar geometry. An electric field ($E_x$) is applied along the bar, the motion of carriers then sets up and electric field ($E_y$) generating a Hall voltage ($V_H$) measured across the bar.

resulting in a equilibrium given by

$$E_y = v_x B_z. \tag{2.18}$$

As the applied magnetic field ($B_z$) and applied current density ($j_x$) are set by the experiment, and the electric field is measured, it is useful to define a quantity known as the Hall coefficient ($R_H$)

$$R_H = \frac{E_y}{j_x B_z} = \frac{v_x}{j_x}. \tag{2.19}$$

If the conductivity of the sample is dominated by electrons, then $v_x = \mu_e E_x$ and $j_x = n\mu_e e E_x$, where $n$ is the carrier density and $\mu_E$ is the electron mobility. This allows the Hall coefficient to be expressed as

$$R_H = \frac{\mu_e E_x}{n\mu_e e E_x} = \frac{1}{ne}, \tag{2.20}$$

and from this the carrier density can be determined directly from the Hall coefficient. In semiconductors however, the situation can be more complicated as there may be conduction by both electrons and holes. In this case the Hall Coefficient is given by

$$R_H = \frac{E_y}{j_x B_z} = \frac{p\mu_p^2 - n\mu_e^2}{e(p\mu_p + n\mu_e)^2}, \tag{2.21}$$

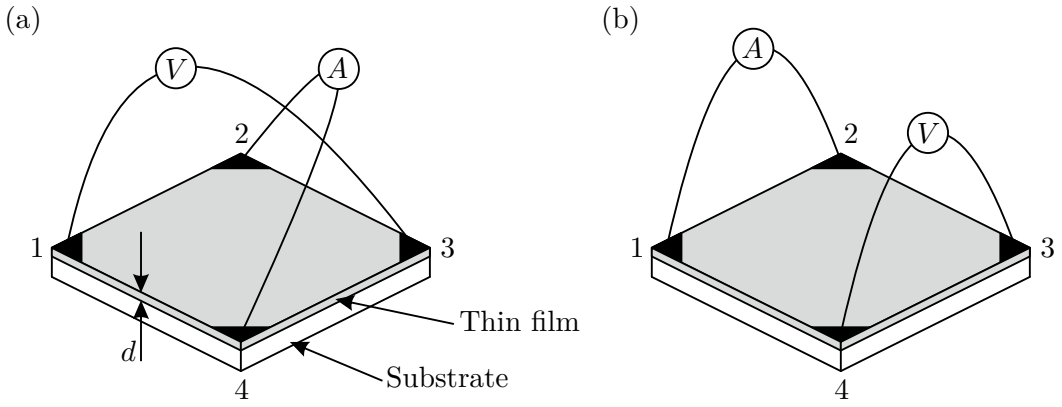


**Figure 2.13.** Diagram of the Van der Pauw geometry for thin film Hall effect measurements. (a) shows the geometry used for Hall measurement, while (b) shows the geometry used for resistance measurement. The thin film of thickness $d$ must be on an insulating substrate.

where $p$ and $\mu_p$ are the hole concentration and mobility respectively. However, as all the CdO samples considered in this thesis are degenerately $n$-type it can be assumed that $p \ll n$ in all cases and therefore equation 2.20 is applicable.

In the actual experiment the applied current ($I$) and measured Hall voltage ($V_H$) are known rather than the current density ($j_x$) and electric field strength ($E_y$). Therefore the experiment yields a sheet carrier density ($n_s$), which can be converted to the bulk carrier density ($n$) through the sample thickness ($d$)

$$n = n_s/d. \tag{2.22}$$

### 2.2.1 Van der Pauw Geometry

A limiting factor in Hall effect measurements, as described above, is that the sample needs to be in the Hall bar geometry to carry out the experiment. The CdO samples discussed in this thesis are thin films on an insulating substrate, therefore an alternative geometry known as the Van der Pauw geometry is used [107]. Four contacts are made to the top surface of the sample, as shown in figure 2.13, allowing both Hall measurements (shown by panel (a)), and resistance measurements (shown by panel (b)) to be made.

To minimize the error in the Hall voltage that may be present due to non-perpendicular current flow in the Van der Pauw geometry, it is common to measure with positive ($B$), negative ($-B$) and zero (0) magnetic field. Applying this methodology the Hall coefficient is given by [107, 108]

$$R_H = \frac{[V_{1,3}(B) - V_{1,3}(0)]d}{I_{2,4}B} = \frac{[V_{1,3}(B) - V_{1,3}(-B)]d}{2I_{2,4}B}, \tag{2.23}$$

where $d$ is the film thickness, the voltage is measured across contacts 1 and 3 ($V_{1,3}$) and the current across contacts 2 and 4 ($I_{2,4}$). The current and voltage contacts can then be switched, allowing repeat measurements and averaging to improve the accuracy of the final result.

For resistivity measurements, a current can be passed between contacts 1 and 2 ($I_{12}$) while the voltage is measured across contacts 3 and 4 ($V_{34}$), as shown in figure 2.13 (b). The resistance is then given by [109]

$$R_{12,34} = \frac{|V_{34}|}{I_{12}}. \tag{2.24}$$

The contacts can then be switched to allow a measurement of $R_{23,41}$ to be obtained. From these two measurements the resistivity can be calculated using

$$\rho = \frac{\pi d}{\ln(2)} \frac{R_{12,34} + R_{23,41}}{2} f, \tag{2.25}$$

where $f$ depends on the ratio $R_{12,34}/R_{23,41}$ via

$$\frac{R_{12,34} - R_{23,41}}{R_{12,34} + R_{23,41}} = f \operatorname{arccosh}\left(\frac{\exp\left(\frac{\ln 2}{f}\right)}{2}\right). \tag{2.26}$$

In practice, $R_{12,34}/R_{23,41} > 2$ suggests poor contacts or an inhomogeneous sample. By the measurement of the resistivity through equation 2.25 and the Hall coefficient

through equation 2.23, the carrier mobility can be determined by the equation

$$\mu = \frac{1}{ne\rho} = \frac{R_H}{\rho}. \tag{2.27}$$

The van der Pauw geometry provides many benefits over a Hall bar geometry, especially in the examination of thin film samples, and allows several complementary measurements to be taken and averaged in order to reduce uncertainties. For these reasons all the Hall effect measurements in this thesis are carried out in the van der Pauw geometry.

### 2.2.2 Ecopia HMS-3000 Hall Effect System

The Hall effect measurements reported in this thesis were obtained using an Ecopia HMS-3000 Hall effect measurement system, operating in the van der Pauw sample geometry. The system can apply currents from 1 nA to 20 mA and measure carrier concentrations from $10^7$ cm$^{-3}$ to $10^{21}$ cm$^{-3}$. A 0.55 T permanent magnet is used to apply the magnetic field. The system allows $I$-$V$ measurements to be made across all of the contact pairs to ensure Ohmic contacts have been made to the sample before carrying out a Hall measurement. The data acquisition software automatically performs the Hall measurements, including repeat measurements and field reversal. The system can also be operated at 77 K using liquid nitrogen if low temperature measurements are required.

## 2.3 Low Energy Electron Diffraction

Low energy electron diffraction (LEED) is one of the most widely used surface science techniques and is responsible for solving more surface structures than any other technique [74, 110]. At the simplest level it is used as a complementary experiment to check the surface periodicity and orientation before employing other surface sensitive techniques. It can also be used to image the azimuthal orientation of the sample, which can be especially useful for aligning the sample prior to ARPES

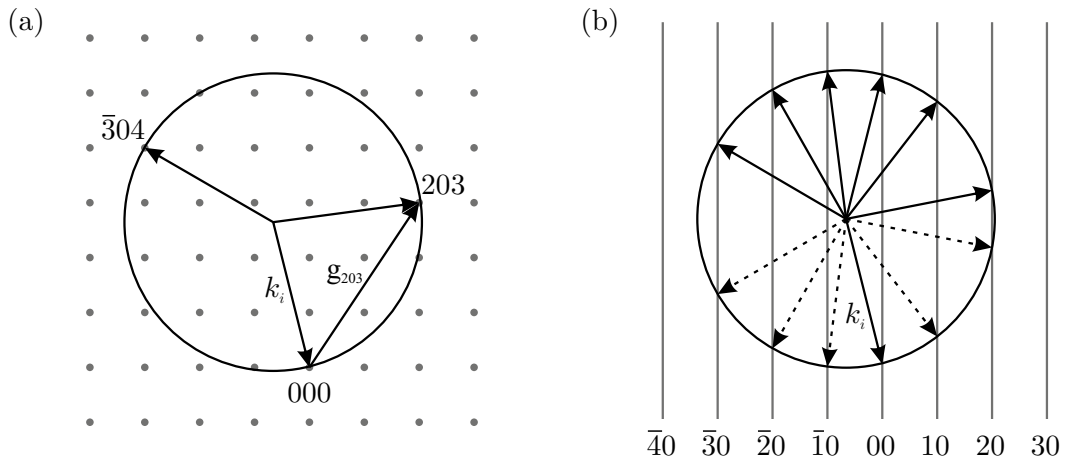


**Figure 2.14.** Ewald sphere construction for (a) bulk and (b) surface cases. The incident wavevector is labeled $k_i$, the other vectors indicate possible diffracted wavevectors. For the bulk case the reciprocal lattice vector $g_{203}$ is also shown. For the surface case the dashed vectors indicate wavevectors diffracted into the crystal bulk which are therefore not observable. Adapted from [110].

measurements. At a more sophisticated level, LEED can be used quantitatively by measuring the intensity of diffracted beams as a function of beam energy, a technique known as LEED-IV [111, 112]. The surface sensitivity of LEED is due to the short IMFP of low energy electrons in solids, discussed previously in relation to photoemission in section 2.1.3.

LEED is based on the diffraction of low energy electrons (20 to 500 eV). A 50 eV electron has a de Broglie wavelength of $\sim$ 1.7 Å, comparable to typical atomic spacings, making it suitable for diffraction. Diffraction can be understood in terms of the conservation of energy and momentum (including the addition of any reciprocal lattice vector) and this gives

$$k_i^2 = k_f^2, \tag{2.28}$$

$$\boldsymbol{k}_f = \boldsymbol{k}_i + \boldsymbol{g}_{hkl}, \tag{2.29}$$

where $\boldsymbol{k}_i$ and $\boldsymbol{k}_f$ are the incident and final wavevectors respectively, and $\boldsymbol{g}_{hkl}$ is a bulk reciprocal lattice vector. This is illustrated graphically by the Ewald sphere construction shown in figure 2.14 (a). Moving from bulk to surface diffraction greatly

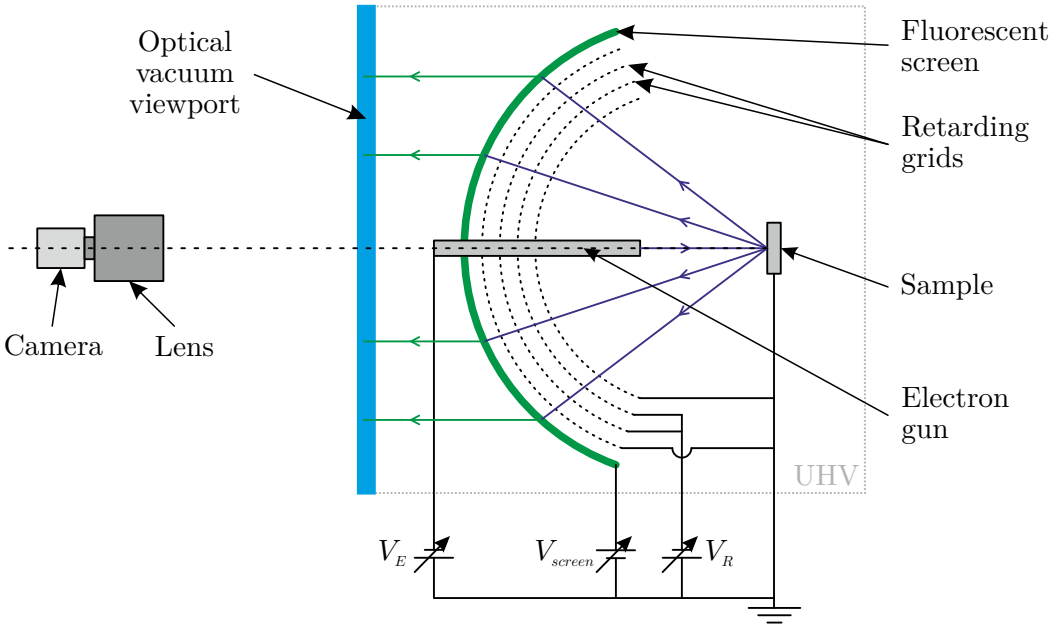


**Figure 2.15.** Schematic of a reverse-view LEED optics, with the key components labeled. The electron gun provides an incident beam of electrons at an energy set by ($V_E$). These electrons travel through the field free region, established by grounding both the sample and inner most grid, and diffract from the sample surface. To filter out the inelastically scattered electrons, a retarding voltage ($V_R$) is applied just below the beam energy. The elastically diffracted electrons are then accelerated into the fluorescent screen, from where they can be imaged using a camera. The optics need to be operated in UHV conditions.

relaxes these constraints as $\mathbf{k}_\perp$ is no longer conserved, and therefore equation 2.29 becomes

$$\mathbf{k}_{f||} = \mathbf{k}_{i||} + \mathbf{g}_{hk}. \tag{2.30}$$

This is illustrated by figure 2.14 (b), where the reciprocal lattice points have been replaced by reciprocal lattice rods. A consequence of this is that changing $\boldsymbol{k}_i$ will now cause shifts in the diffracted beams, rather than the disappearance and appearance of new beams as in the bulk case.

A schematic of a typical reverse-view LEED optic is shown in figure 2.15. The optic consists of a low energy electron gun, a series of grids used to apply potentials, and a phosphor screen. Electrons, which are typically supplied by a heated tungsten or $LaB_6$ filament, are focused and accelerated towards the sample (all of which occurs within the electron gun), resulting in a electron beam with a well defined KE. The

sample and innermost grid are held at ground in order to provide an electric field-free region between the sample and the optics. Many of the electrons impacting the surface will undergo inelastic scattering and will therefore not contribute to the diffraction pattern. The retarding grids are used as a high pass energy filter only allowing elastically scattered electrons to reach the screen. After the retarding grids, a high positive voltage (3 to 7 kV) is applied to the phosphor screen to accelerate the electrons and make the diffraction pattern visible. Modern LEED optics are of the reverse view type, where the pattern is viewed through a viewport behind the screen. For analysis, LEED patterns have been recorded using a CCD camera.

## 2.4 CdO Samples

The CdO samples investigated throughout this thesis were grown at the Universitat de València (Spain) using metalorganic vapor-phase epitaxy (MOVPE). The epitaxial CdO(100) single crystal thin films were grown on *r*-plane $(01\bar{1}2)$ sapphire ($Al_2O_3$) substrates. In MOVPE, reactive precursor gasses are exposed to the heated substrate where they react to produce the film. In the case of CdO, dimethylcadmium [$(CH_3)_2Cd$] and 2-methylpropan-2-ol [$(CH_3)_3COH$] are used as the cadmium and oxygen precursors respectively. These are transported to the substrate by a nitrogen carrier gas. The substrate growth temperature was varied between 308 °C and 405 °C to optimise the film quality. The quality of the films were investigated by atomic force microscopy (AFM) and x-ray diffraction (XRD). The best films exhibited XRD peaks with full width at half maxium (FWHM) of 0.14° and an AFM root mean square (RMS) surface roughness of $\sim$ 2 nm. The film thicknesses of the samples studied in this thesis ranged from 400 nm to 900 nm. Further details of the sample growth and characterisation can be found in reference [20].

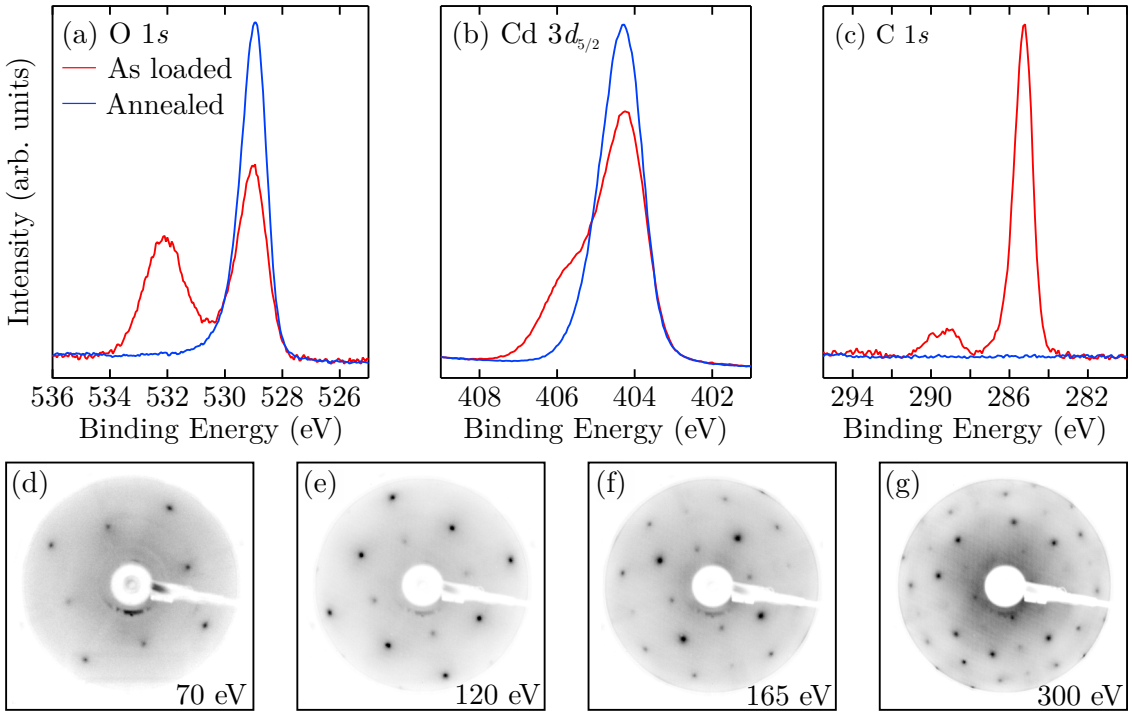


**Figure 2.16.** (a-c) A comparison of XPS spectra for as-loaded and UHV annealed CdO(100) samples, taken with $h\nu = 1486.6$ eV. The spectra have been normalised to the Cd $3d_{5/2}$ area, and the annealed spectra shifted by -1.08 eV to align the peaks, allowing the cleaning effect to be clearly observed. (d-g) show typical LEED images taken from an UHV annealed CdO(100) sample, with the sharp $(1 \times 1)$ pattern indicating a well ordered surface. The images have been inverted to improve contrast.

### 2.4.1 Surface Preparation in UHV

In order to perform surface sensitive photoemission measurements on CdO, the sample needs to be prepared with a clean and ordered surface in UHV conditions. There are several commonly used approaches to UHV surface preparation including; ion bombardment and annealing (IBA), chemical etching and cleaving. IBA has previously been used to prepare CdO samples [113]. However, an annealing temperature of 420 °C was used, resulting in the photoemission spectra still displaying a small amount of surface contamination.

Several previous studies [66, 114–116] have prepared CdO samples in UHV just by annealing. Figure 2.16 shows the effect of a half hour 600 °C UHV anneal on a CdO(100) sample. The O $1s$ XPS spectra of the as-loaded CdO(100) sample (fig-

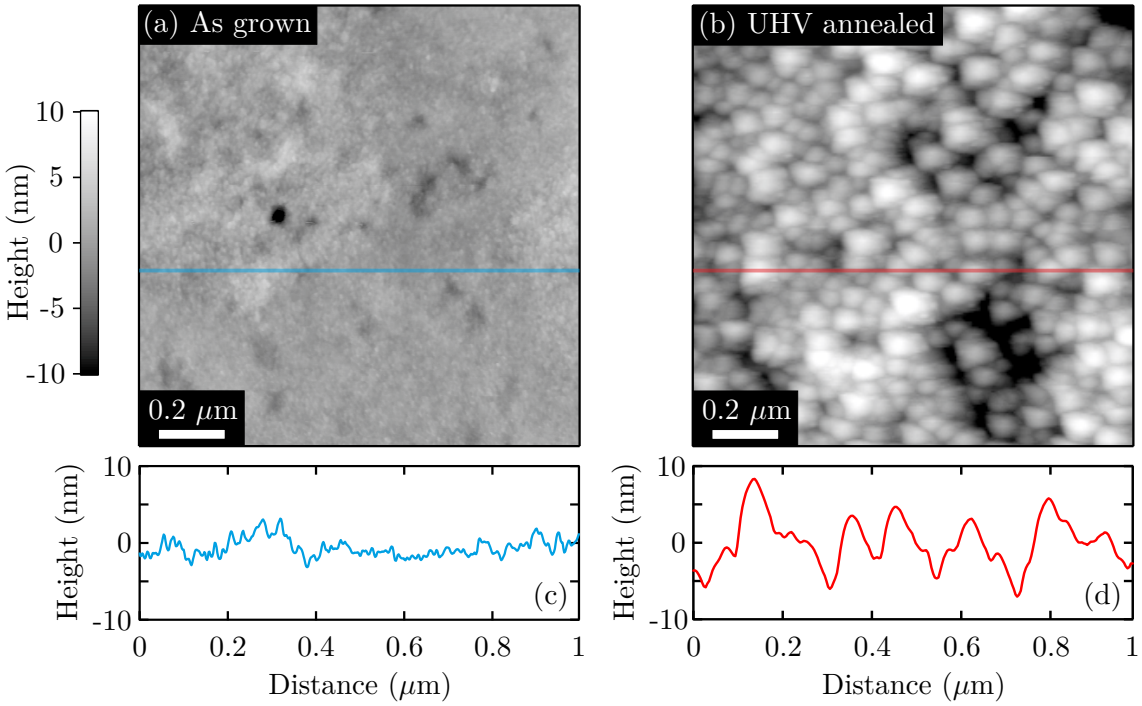


**Figure 2.17.** AFM data illustrating the effect of UHV annealing on the CdO(100) surface. (a) and (b) show 1 $\mu$m $\times$ 1 $\mu$m AFM height images of an as-grown and UHV annealed CdO(100) sample, showing the surface roughening and recrystallisation following UHV annealing. Both images are shown with the same indicated colour scale to allow the difference to be observed. (c) and (d) show line profiles taken from the positions indicated across images (a) and (b) to allow the surface roughness to be observed.

ure 2.16 (a)) shows a large contamination peak at $\sim$ 532 eV which is assigned to hydroxide and carbonate species, possibly related to the growth, or atmospheric contamination [113, 115]. The Cd $3d_{5/2}$ spectra (figure 2.16 (b)) also shows a large contamination component at $\sim$ 406 eV which is principally assigned to $CdCO_3$. These components are fully removed by annealing in UHV. Additionally the C $1s$ region (figure 2.16 (c)) shows a significant peak associated with atmospheric contamination on the as loaded sample which is fully removed by the annealing. Typical LEED patterns observed from the cleaned CdO(100) surface are shown in figure 2.16 (d-g), exhibiting a sharp $(1 \times 1)$ pattern which indicates a well-ordered surface.

To investigate the effects of UHV annealing on the CdO(100) surface, AFM was taken of both the as-grown surface and following annealing in UHV, shown in figure 2.17. The AFM measurements were performed using a Asylum Research MFP-3D

at the University of Warwick. The as-grown CdO(100) surface exhibits an RMS roughness of $\sim$ 2 nm, broadly in agreement with similar measurements performed immediately after the film growth [20]. However, following UHV annealing the surface shows much more texture and a RMS roughness of $\sim$ 5 nm. This increase in surface roughness may to be related to a recrystallisation of the surface, possibly associated with a loss of oxygen during the annealing process. An oxygen deficient surface is supported by analysis of the XPS shown in figure 2.16 which indicates a surface composition of 56% cadmium to 44% oxygen. This AFM result appears to be contradictory to the LEED measurement which shows the annealed CdO surface is well ordered. This suggests two possibilities, either, the newly formed annealed surface contains grains all of which have the same orientation, or, the outermost layer is disordered and therefore produce only background intensity and the diffraction pattern is generated by ordered underlying layers. It would be of interest to conduct a more through study into the effects of annealing on the surface morphology to better understand this process. These results show that clean, well-ordered CdO(100) surfaces can be successfully prepared in UHV by controlled annealing at 500 °C to 600 °C. This approach results in no observable contamination in XPS and sharp a $(1 \times 1)$ LEED pattern.

This chapter has described the experimental techniques and equipment used to obtain the results presented in this thesis. The key experimental technique used is photoemission which has been described in detail, and the associated surface science technique of LEED has also been described which is used to confirm successful surface preparation where required. Hall effect measurements are described, which are used throughout this thesis to obtain information about the bulk electronic properties of CdO samples. Finally a introduction of the samples studied is given, this included a summary of the growth technique, and a overview of the surface preparation approach used throughout this thesis when a clean CdO(100) surface is required.

# CHAPTER 3

# Theoretical Background

This thesis is concerned with the electronic properties and structure of CdO, therefore a number of theoretical approaches are required to understand the CdO band structure. Additionally, CdO exhibits strong downward band bending and significant electron accumulation at its surface. In order to investigate these phenomena it is therefore necessary to develop a model of the space charge layer at the surface of CdO. In this chapter an outline of the theoretical methods used throughout this thesis are described. Specifically, approximations to semiconductor band structure, density functional theory, space charge regions, and quantised subband states are outlined and discussed.

## 3.1 Semiconductor Band Structure

The band structure of a semiconductor is a theoretical framework that enables the understanding of the electronic properties of a material. In general this problem is fully expressed by the Schrödinger equation

$$\mathcal{H}|\Psi\rangle = E|\Psi\rangle, \tag{3.1}$$

where $E$ is the electron energy, $\Psi(\mathbf{r}_1, \mathbf{r}_2, \cdots, \mathbf{r}_n)$ is the many body wave function, and the Hamiltonian ($\mathcal{H}$) is given by [108]

$$\mathcal{H} = \sum_i \frac{p_i^2}{2m_i} + \sum_j \frac{P_j^2}{2M_j} + \frac{1}{2}\sum_{j',j}{}' \frac{Z_j Z_{j'} e^2}{|\mathbf{R}_j - \mathbf{R}_{j'}|} - \sum_{i,j} \frac{Z_j e^2}{|\mathbf{r}_i - \mathbf{R}_j|} + \frac{1}{2}\sum_{i,i'}{}' \frac{e^2}{|\mathbf{r}_i - \mathbf{r}_{i'}|}. \quad (3.2)$$

Where $i$ and $j$ label the electrons and nuclei respectively, $\mathbf{p}_i$ and $\mathbf{P}_j$ are the electron and nuclei momentum operators respectively, and $\mathbf{r}_i$ and $\mathbf{R}_j$ are the position of the $i^{\text{th}}$ electron and $j^{\text{th}}$ nucleus respectively. $\sum'$ denotes the sum over non-equivalent indices only.

However, solving this equation for all the electrons in a material is impractical and the only way forward is to make a series of simplifications. Firstly the electrons are separated into two groups, core and valence. The core electrons are localised around the nuclei and can therefore be combined with the nuclei to form ion cores. Secondly the Born-Oppenheimer [117], or adiabatic approximation is applied, which states that the ion cores appear to be stationary to the electrons as the ion cores are much heavier ($M_j \gg m_i$). Conversely, to the ions, the electrons move so quickly they only see a time-averaged potential. These approximations allow the Hamiltonian to be written as a sum of three terms

$$\mathcal{H} = \mathcal{H}_{ions}(\mathbf{R}_j) + \mathcal{H}_e(\mathbf{r}_i, \mathbf{R}_{j0}) + \mathcal{H}_{e-ion}(\mathbf{r}_i, \delta\mathbf{R}_j), \quad (3.3)$$

where $\mathcal{H}_{ions}(\mathbf{R}_j)$ is the Hamiltonian of the ions moving within their own potential and the time-averaged electron potential, $\mathcal{H}_e(\mathbf{r}_i, \mathbf{R}_{j0})$ is the electronic Hamiltonian of the electrons moving in the potential established by the frozen ion cores, and $\mathcal{H}_{e-ion}(\mathbf{r}_i, \delta\mathbf{R}_j)$ is the Hamiltonian resulting from the ions being displaced from their equilibrium positions by $\delta\mathbf{R}_j$, commonly referred to as the electron-phonon interaction. The electronic properties are dominated by the electronic Hamiltonian

and are given by

$$\mathcal{H}_e = \sum_i \frac{p_i^2}{2m_e} + \frac{1}{2}\sum_{i,i'}{}' \frac{e^2}{|\mathbf{r}_i - \mathbf{r}_{i'}|} - \sum_{i,j} \frac{Z_j e^2}{|\mathbf{r}_i - \mathbf{R}_{j0}|}. \tag{3.4}$$

Physically these three terms represent the KE of the electrons, the electron-electron and electron-ion interactions. Even solving this simplified electronic Hamiltonian remains impractical due to the large number of electrons present in a real material ($> 10^{23}$ electrons cm$^{-3}$), so a further approximation is required. This is achieved by assuming that each electron experiences the same averaged potential $V(\mathbf{r})$, known as the mean-field approximation. Applying this approximation results in the one-electron Hamiltonian ($\mathcal{H}_{1e}$) which is given by

$$\mathcal{H}_{1e} = \frac{p^2}{2m_e} + V(\mathbf{r}). \tag{3.5}$$

Substituting this Hamiltonian into equation 3.1 results in the one-electron Schrödinger equation

$$\mathcal{H}_{1e}\psi_n(\mathbf{r}) = \left(\frac{p^2}{2m_e} + V(\mathbf{r})\right)\psi_n(\mathbf{r}) = E_n\psi_n(\mathbf{r}). \tag{3.6}$$

The eigenstates of this equation are Bloch electrons, which are independent electrons moving within a periodic potential. This is discussed in the next section.

### 3.1.1 Bloch Therom

In a periodic crystal, the form of the potential $V(\mathbf{r})$ must also be periodic such that $V(\mathbf{r}) = V(\mathbf{r} + \mathbf{R})$, where $\mathbf{R}$ is a Bravais lattice vector. Therefore by applying Bloch's theorem [41], the eigenstates of equation 3.6 can be written as a plane wave multiplied by a function with the periodicity of the lattice

$$\psi_{n\boldsymbol{k}}(\mathbf{r}) = e^{i\boldsymbol{k}\cdot\mathbf{r}} u_{n\boldsymbol{k}}(\mathbf{r}), \tag{3.7}$$

where $n$ is the band index, and $\boldsymbol{k}$ is the electron's wavevector in the first BZ, and $u_{n\boldsymbol{k}}(\mathbf{r})$ is given by

$$u_{n\boldsymbol{k}}(\mathbf{r}) = u_{n\boldsymbol{k}}(\mathbf{r} + \mathbf{R}). \tag{3.8}$$

The solution of Schrödinger's equation (3.1), even with the simplified one-electron Hamiltonian (equation 3.5) and the requirement of periodicity is still non-trivial. However, as many of the properties of semiconductors depend only on the bands nearest the Fermi level, it can be sufficient to approximate only these bands. These approximations are described in the following sections.

### 3.1.2 Parabolic Bands Approximation

The most simple model is that of parabolic bands, which is recovered when the one-electron potential is zero ($V(\mathbf{r}) = 0$) i.e. the free electron case [41]. In this model the dispersion relation is given by

$$E_{C,V}(\boldsymbol{k}) = E_{C,V}(0) \pm \frac{\hbar^2 \boldsymbol{k}^2}{2m^*}, \tag{3.9}$$

where $E_{C,V}(\boldsymbol{k})$ is the conduction or valence band dispersion, $\boldsymbol{k}$ is the wavevector, and $m^*$ is the effective mass of the band. $E_{C,V}(0)$ defines the band edge energy positions, where the band gap is given by $E_G = E_C(0) - E_V(0)$.

This approximation typically works well for direct-gap semiconductors, where the VBM and CBM are at the BZ centre ($\Gamma$). It requires that there is only a weak interaction between the CB and VB, typically fulfilled by a large band gap. As CdO is an indirect semiconductor, which is typically degenerate, the parabolic bands model is not sufficient and the effects of non-parabolicity need to be included.

### 3.1.3 $\boldsymbol{k}\cdot\boldsymbol{p}$ Perturbation Method

Originally proposed by Kane [118] the $\boldsymbol{k}\cdot\boldsymbol{p}$ perturbation method is a more accurate band structure approximation and allows for the inclusion of non-parabolic effects. The $\boldsymbol{k}\cdot\boldsymbol{p}$ method can be derived from the one-electron Hamiltonian (equation 3.6) solution of the Schrödinger equation (equation 3.1) [119].

$$\left[\mathcal{H}_{1e}+\frac{\hbar}{m}\boldsymbol{k}\cdot\boldsymbol{p}+V_{so}\right]u_{n\boldsymbol{k}}=E'_{n\boldsymbol{k}}u_{n\boldsymbol{k}}. \tag{3.10}$$

Here $\mathcal{H}_{1e}$ is given by equation 3.5, and $E'_{n\boldsymbol{k}}=E_{n\boldsymbol{k}}-\frac{\hbar^2\boldsymbol{k}^2}{2m}$. At the BZ centre, ($\Gamma$), $\boldsymbol{k}=0$, therefore this simplifies to

$$\left[\mathcal{H}_{1e}+V_{so}\right]u_{n\mathbf{0}}=E_{n\mathbf{0}}u_{n\mathbf{0}}. \tag{3.11}$$

The solutions of equation 3.11 form an orthonormal set, therefore the eigenvalues at points close to $\Gamma$ can be found by treating the $\boldsymbol{k}\cdot\boldsymbol{p}$ term as a perturbation, which represents the interaction of the CB and VB.

In Kane's original theory applied to zincblende InSb, the top three VBs and the CB are all doubly degenerate, giving a $8\times 8$ Hamiltonian of the form

$$\mathcal{H}=\begin{pmatrix}\mathcal{H}_{sub} & 0\\ 0 & \mathcal{H}_{sub}\end{pmatrix} \tag{3.12a}$$

$$\mathcal{H}_{sub}=\begin{pmatrix}E_C(0) & 0 & kP & 0\\ 0 & E_V(0)-\frac{\Delta_{so}}{3} & \frac{\sqrt{2}\Delta_{so}}{3} & 0\\ kP & \frac{\sqrt{2}\Delta_{so}}{3} & E_C(0) & 0\\ 0 & 0 & 0 & E_V(0)+\frac{\Delta_{so}}{3}\end{pmatrix} \tag{3.12b}$$

where $E_C(0)$ and $E_V(0)$ are the conduction and valence band energies at the $\Gamma$ point.

$\Delta_{so}$ is the spin orbit splitting and $P$ is Kane's matrix element given by

$$P^2 = \frac{3\hbar^2(1/m_0^* - 1/m_0)}{2[2/E_G + 1/(E_G + \Delta_{so})]}. \tag{3.13}$$

In the case of CdO, the crystal is assumed to be isotropic and $\Delta_{so} \approx 40$ meV [34], and therefore spin-orbit splitting can be neglected as $\Delta_{so} \ll E_G$. Consequently equation 3.12 reduces to

$$\mathcal{H} = \begin{pmatrix} E_C(0) & kP \\ kP & E_V(0) \end{pmatrix}. \tag{3.14}$$

The conduction band dispersion is given by

$$E_C(k) = E' + E_k = E' + \frac{\hbar^2 k^2}{2m_0}, \tag{3.15}$$

where $E'$ is the largest eigenvalue of equation 3.14. By setting $E_C(0) = 0$ and $E_V(0) = -E_G$ defines the energy zero at the CBM. Then the analytic form of the CB dispersion is given by

$$E_C(k) = \frac{1}{2}\left[-E_G + \sqrt{E_G^2 + 4k^2P^2}\right] + \frac{\hbar^2 k^2}{2m_0}, \tag{3.16}$$

where the simplified Kane matrix element is given by

$$P^2 = \frac{\hbar^2}{2m_0}\left(\frac{m_0}{m_0^*} - 1\right) E_G. \tag{3.17}$$

Although the theory proposed by Kane is for a zinc-blende structure, after the simplifications applied here the resulting CB dispersion provides a general approach to model the non-parabolicity of the CB. This can be seen in figure 3.1, where a comparison is made between parabolic and $\boldsymbol{k} \cdot \boldsymbol{p}$ CB dispersions.

The analytic form of the CB dispersion given by equation 3.16 additionally allows

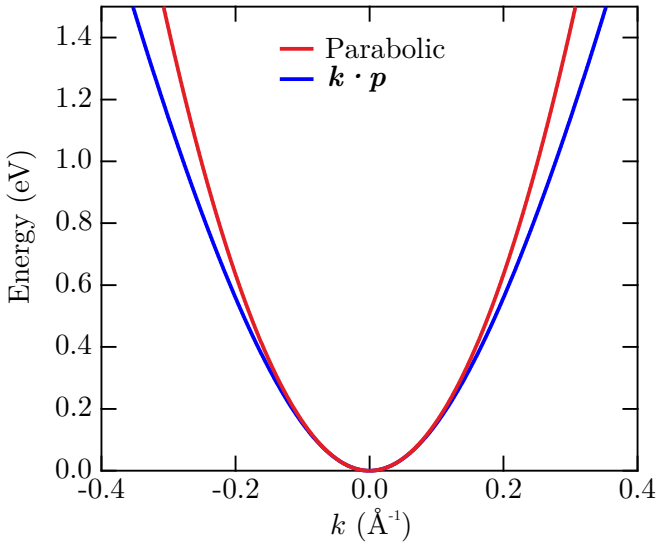


**Figure 3.1.** Comparison of the CB dispersion obtained from the parabolic and $\boldsymbol{k \cdot p}$ band structure approximations for CdO. Calculation parameters were set to values typical for CdO ($E_G = 2.2$ eV, $m^* = 0.24$ [38, 120]).

for both analytical expressions for the CB DOS, which can be expressed as

$$g_c(k) = \frac{k}{\pi^2}\left[\frac{dE_C(k)}{dk}\right]^{-1} = \frac{k^2}{\pi^2}\left[2P^2[E_G^2 + 4k^2P^2]^{-\frac{1}{2}} + \frac{\hbar^2}{m_0}\right]^{-1}, \tag{3.18}$$

and the energy dependent effective mass

$$m^*(E) = \hbar^2 k\left[\frac{dE_C(k)}{dk}\right]^{-1} = \hbar^2\left[2P^2[E_G^2 + 4k^2P^2]^{-\frac{1}{2}} + \frac{\hbar^2}{m_0}\right]^{-1}, \tag{3.19}$$

to be derived.

### 3.1.4 Density Functional Theory

In some cases the band structure approximation schemes described in this chapter, although convenient, may not be sufficient. Examples include when the band dispersion away from the BZ centre or an orbitally resolved partial density of states is required. A more sophisticated approach is required to obtain more detailed knowledge of the electronic structure of a material. One of the most successful approaches for the calculation of material properties is density functional theory (DFT). DFT itself is a very large topic and is applied across many fields including; materials sci-

ence, physics, chemistry, geology, and astrophysics. There are many excellent text books on the subject, so only a brief outline of the technique is provided here, as is relevant to the material in this thesis [121–125].

DFT is founded on two key principles expressed by Hohenberg and Kohn in 1964 [126], in which they state that the total energy of a non-spin-polarised system of interacting electrons in an external potential is given exactly by a functional of the ground state density ($\rho$)

$$E = E[\rho]. \tag{3.20}$$

Additionally, they realised that the true ground state density is the one which minimizes this total energy. However, the Hohenberg and Kohn theory doesn't provide any insight into the form of $E[\rho]$.

In 1965, Kohn and Sham started the modern field of DFT by realising that a system of many interacting electrons in an external potential can be mapped exactly into a system of noninteracting particles in an effective external potential [127]. This results in a set of self-consistent single particle equations known as the Kohn-Sham equations

$$\{T + V_{e-i}(\mathbf{r}) + V_H(\mathbf{r}) + V_{xc}(\mathbf{r})\}\, \varphi_i(\mathbf{r}) = \epsilon_i \varphi_i(\mathbf{r}), \tag{3.21}$$

where $T$ is the single electron KE, $V_{e-i}$ is the electron-ion Coulomb potential (i.e. the lattice potential), $V_H$ is the Hartree potential, and $V_{xc}$ is the exchange-correlation potential. The $\varphi_i$ are single electron Kohn-Sham orbitals and the $\epsilon_i$ are the corresponding Kohn-Sham eigenvalues. From this the density can be found by a sum over the occupied orbitals

$$\rho(\mathbf{r}) = \sum_{occu.} \varphi_i^*(\mathbf{r})\varphi_i(\mathbf{r}). \tag{3.22}$$

Two terms in equation 3.21 depend on the density, $V_H(\mathbf{r})$ and $V_{xc}(\mathbf{r})$,

$$V_H(\mathbf{r}) = e^2 \int d^3\mathbf{r'} \frac{\rho(\mathbf{r'})}{|\mathbf{r'} - \mathbf{r}|}, \tag{3.23}$$

$$V_{xc}(\mathbf{r}) = \frac{\delta E_{xc}[\rho]}{\delta \rho}. \tag{3.24}$$

It is therefore possible to solve this set of equations self-consistently. An initial guess is made for the density ($\rho(\mathbf{r})$), then equation 3.21 can then be solved for the Kohn-Sham orbitals ($\varphi_i(\mathbf{r})$). These can then be inserted back into equation 3.22 to obtain a new density. If this is different, then the new and initial densities can be mixed and the process repeated until it is self-consistent. That is, a density that when used to solve the Kohn-Sham equations results in Kohn-Sham orbitals that reproduce it. By the application of this approach, the problem of solving the many-body Schrödinger equation is reduced to solving a set of single particle equations, with a self-consistency requirement. This theory is exact, however, the form of the exchange-correlation functional ($E_{xc}[\rho]$) is not known in general, and this is where the application of DFT depends on the development of accurate approximations.

There are various approximations to the exchange-correlation functional which have had surprising success in reproducing many real systems. The first is the LDA which defines the exchange-correlation for a uniform electron gas. Obviously this is not the case for a crystalline solid. However, despite this the LDA has still had much success in modeling real systems. The next most commonly applied approximation to the exchange-correlation is generalized gradient approximation (GGA). This approach assumes the system can be more accurately approximated if the gradient of the density, as well as the density itself is taken into account. Unlike LDA, however, there are several different implementations of GGA, the two most common are PBE (and its derivatives) [128], and BLYP [129, 130].

The largest problem in the application of these functionals to CdO is the under-estimation of the band gap. In fact, these basic functionals predict CdO to be

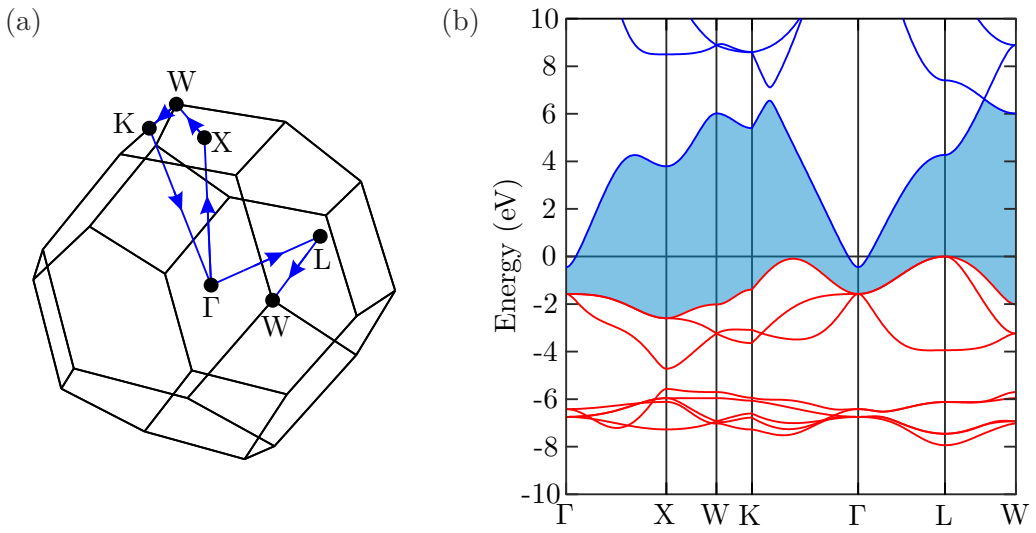


**Figure 3.2.** Example DFT LDA band structure, (a) shows the $k$-path through the BZ used to generate panel (b) which shows the band dispersion. Blue and red lines represent CBs and VBs respectively, the blue shaded region indicates the band gap. Note that the CBM at the Γ point is below the VBM at L, this indicates semi-metallic behaviour. Also note the CB dispersion is very isotropic.

semi-metallic, which can be seen in the LDA calculation shown in figure 3.2. To overcome this issue several more advanced techniques, including hybrid functionals and quasiparticle corrections [131] have been developed but these are beyond the scope of the discussion here. This issue is revisited in chapter 5.

#### 3.1.4.1 Linearised Augmented-Plane Wave Method

The DFT calculations performed in this thesis make use of the ELK DFT code. This code is open source (GNU General Public Licence) and is available at `http://elk.sourceforge.net`. The code uses the full-potential linearised augmented-plane wave (FP-LAPW) method with local orbitals [124]. The linearised augmented-plane wave (LAPW) is one of the most accurate approaches to electronic structure calculation. In this method the crystal is partitioned into two regions, a spherical muffin-tin region surrounding the atomic cores and an interstitial region elsewhere [132, 133]. Plane waves are used as the basis in the interstitial region. These are augmented with spherical harmonic functions within the spheres to account for the rapidly varying

wavefunctions there. In terms of this basis, the wavefunctions can be expressed as

$$\varphi(\mathbf{r}) = \begin{cases} \Omega^{-\frac{1}{2}} \sum_{\mathbf{G}} c_{\mathbf{G}} e^{i(\mathbf{G}+\boldsymbol{k})\cdot\mathbf{r}} & \mathbf{r} \in I \\ \sum_{\ell m} [A_{\ell m} u_\ell(r) + B_{\ell m} \dot{u}_\ell(r)] Y_{\ell m}(\hat{\mathbf{r}}) & \mathbf{r} \in S \end{cases} \tag{3.25}$$

where $\Omega$ is the cell volume, $u_\ell(r)$ is the radial solution of the Schrödinger equation at the energy of interest. $c_{\mathbf{G}}$, $A_{\ell m}$ and $B_{\ell m}$ are expansion coefficients and $Y_{\ell m}$ is the spherical harmonic function. The values of $A_{\ell m}$ and $B_{\ell m}$ are fixed by matching the value and the derivative of the wavefunctions at the muffin-tin boundary, to ensure the wavefunctions are smooth and continuous, which leaves only $c_{\mathbf{G}}$ as a variational coefficient. The LAPW basis set can be very efficient as the slowly varying wavefunctions in the interstitial region can be accurately represented by only a small number of plane wave coefficients, and near the atomic cores where the wavefunction is changing rapidly it can be represented in terms of radial functions.

## 3.2 Space Charge Layers

Several sections of this thesis discuss the electron accumulation layer present at CdO(100) surfaces. This electron accumulation layer can be formed either by the surface itself, which leads to dangling bonds which can act as electron donors, or by adsorbates which can contribute electrons into the surface region. This accumulation layer is spatially confined and so results in the electronic states becoming quantised. In this section a calculation scheme for modeling this accumulation layer and the resulting quantised states is outlined.

### 3.2.1 Poisson's Equation

In order to model this system the potential and electron density as a function of depth into the sample is required. This is described by Poisson's equation, and in 1D this can be written as

$$\frac{d^2V}{dz^2} = -\frac{e}{\epsilon(0)\epsilon_0}[N_D^+ - N_A^- - n(z) + p(z)], \tag{3.26}$$

where $\epsilon(0)$ is the static dielectric constant of the material, $N_D^+$ ($N_A^-$) is the bulk ionised donor (acceptor) density, and $n(z)$ [$p(z)$] is the depth dependent electron [hole] density [43]. For materials such as CdO which are degenerately n-type, the hole and acceptor densities can be assumed to be zero [$p(z) = N_A^- = 0$]. As there cannot be any band bending in the bulk of the material the potential must satisfy

$$V(z) \to 0 \text{ as } z \to \infty, \tag{3.27}$$

and the potential gradient at the surface is related to the surface state density ($N_{ss}$) by

$$\left.\frac{dV}{dz}\right|_{z=0} = -\frac{e}{\epsilon(0)\epsilon_0}N_{ss}. \tag{3.28}$$

By applying the MTFA, Poisson's equation (equation 3.26) can be solved obeying the boundary conditions (equation 3.27 and 3.28) [134]. The electron density will be given by

$$n(z) = \int_0^\infty g_c(E) f_{FD}(E) f(z) dE, \tag{3.29}$$

where $g_c(E)$ is the conduction band density of states, $f_{FD}(E)$ is the Fermi-Dirac distribution including the depth dependent potential which is given by

$$f_{FD}(E) = (1 + \exp[E - E_F + V(z)])^{-1}, \tag{3.30}$$

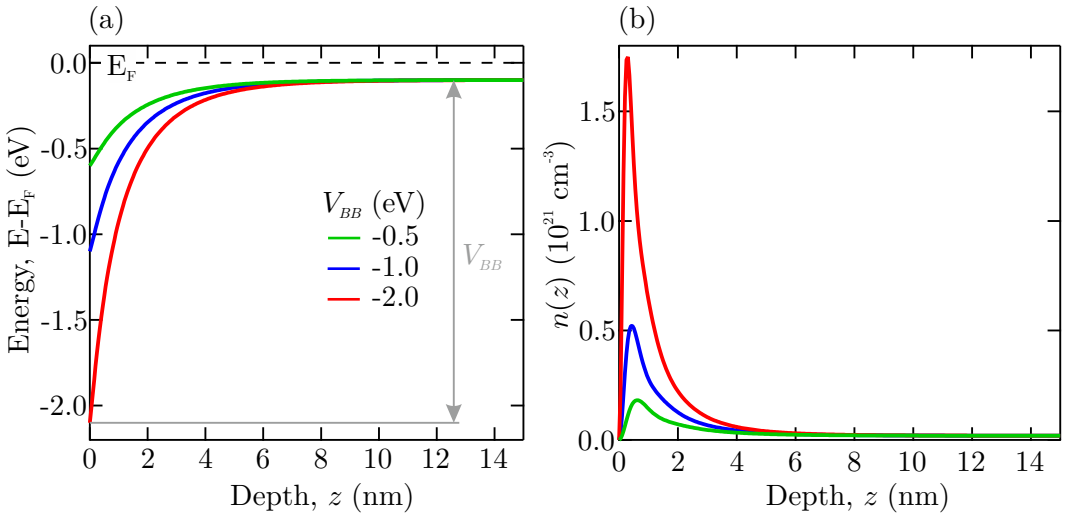


**Figure 3.3.** Example results from the Poisson-MTFA calculations for three values of $V_{BB}$. (a) shows the CB bending profile as a function of depth. (b) Shows the carrier density as a function of depth $n(z)$. Calculation parameters were set to values typical for CdO ($n = 2 \times 10^{19}$ cm$^{-3}$, $E_G = 2.2$ eV, $m_0^* = 0.24$, $\epsilon(0) = 18$, $T = 300$ K). This results in a FL $\sim 0.1$ eV above the bulk CBM.

and $f(z)$ is the MTFA factor accounting for the potential barrier created by the surface [135], given by

$$f(z) = 1 - \text{sinc}\left[\frac{2z}{L}\left(\frac{E}{k_B T}\right)^{\frac{1}{2}}\left(1 + \frac{E}{E_G}\right)^{\frac{1}{2}}\right]. \tag{3.31}$$

Here sinc $= \frac{\sin(x)}{x}$, and $L$ is the characteristic screening length. For degenerate semiconductors, such as CdO, this can be given by the uncertainty principle, $\Delta z \Delta p \approx \hbar$, where $\Delta z = L$ and $\Delta p = \hbar k_F$, and therefore $L = \frac{1}{k_F}$ [134]. Physically this factor serves to represent the interference of wavefunctions reflected by the surface potential barrier. It also ensures that the carrier density tends smoothly to zero at the surface.

This system of equations can be solved numerically by first specifying either the surface state density ($N_{SS}$) or equivalently the band bending potential ($V(0) = V_{BB}$), and varying the other until a solution is found where the potential goes smoothly to zero in the bulk (equation 3.27). Examples of the results of these calculations are shown in figure 3.3 for parameters typical of CdO. The increased band bending

results in a larger electron density within the accumulation layer, which extends over a typical depth of $\sim 5$ nm in CdO.

### 3.2.2 Coupled Poisson-Schrödinger Equations

Once a potential profile has been obtained by solving the Poisson-MTFA equation, described in the previous section, Schrödinger's equation can be solved numerically including this potential. This method is described in full by King et al. [136] and is summarised here.

The one electron band bending potential destroys the crystal symmetry and it is therefore appropriate to express the Schrödinger equation in terms of Wannier Functions ($\Psi(\mathbf{r}_{||}, z)$) [137]. In this representation, Schrödinger's equation can be written as

$$[E_C(-i\nabla) + V(z)]\Psi(\mathbf{r}_{||}, z) = E\Psi(\mathbf{r}_{||}, z), \tag{3.32}$$

where $\mathbf{r}_{||}$ is the surface parallel component of the position vector. The eigenfunction for a subband $j$ and parallel wavevector $k_{||}$ are given by

$$\Psi_{\boldsymbol{k}_{||},j}(\mathbf{r}_{||}, z) = A^{-\frac{1}{2}} \exp[i\boldsymbol{k}_{||} \cdot \mathbf{r}_{||}]\psi_{\boldsymbol{k}_{||},j}(z), \tag{3.33}$$

where $A$ is a normalisation constant and $\psi_{\boldsymbol{k}_{||},j}(z)$ is the component of the eigenfunction normal to the surface. Imposing the boundary conditions that the wavefunction goes to zero at the surface and also decays to zero by a length $l$ into the bulk, as is required for a surface localised state, allows $\psi_{\boldsymbol{k}_{||},j}(z)$ to be expanded as a Fourier series

$$\psi_{\boldsymbol{k}_{||},j}(z) = \sum_{\nu=1}^{\infty} \left(\frac{2}{l}\right)^{\frac{1}{2}} a_{\nu}^{\boldsymbol{k}_{||},j} \sin\left(\frac{\nu\pi z}{l}\right). \tag{3.34}$$

Substituting this into the equation 3.32 gives a matrix representation of the problem for a given $\boldsymbol{k}_{||}$ where the matrix elements are given by

$$[\mathbf{M}]_{\nu\nu'} = E_C(k_\nu)\delta_{\nu\nu'} + \frac{2}{l}\int_0^l V(z) \sin\left(\frac{\nu\pi z}{l}\right) \sin\left(\frac{\nu'\pi z}{l}\right) \mathrm{d}z, \tag{3.35}$$

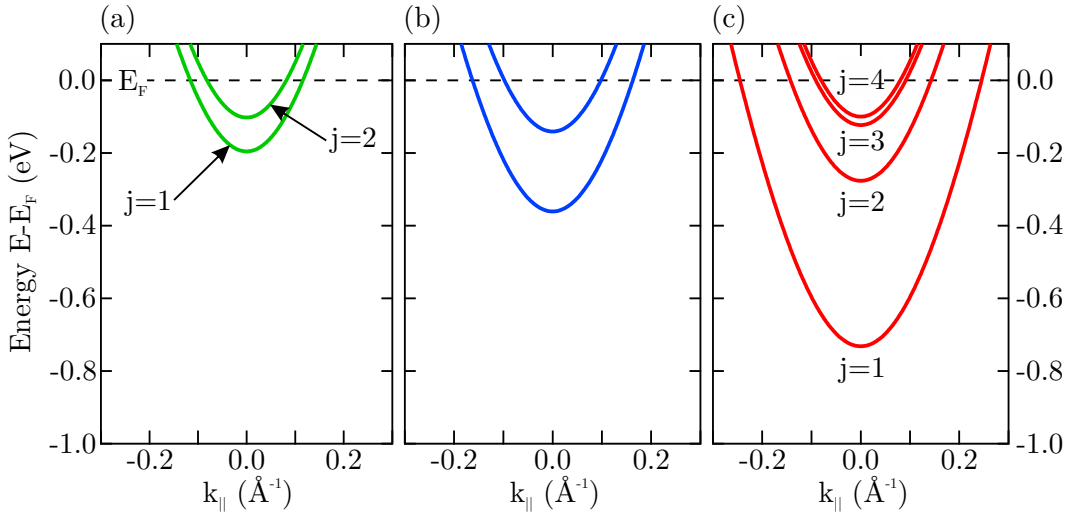


**Figure 3.4.** Example subband dispersions calculated using the coupled Poisson-MTFA/Schrödinger method. The band bending potentials and material parameters are the same as shown in figure 3.3. (a) $V_{BB} = -0.5$ eV, (b) $V_{BB} = -1.0$ eV, (c) $V_{BB} = -2.0$ eV.

where $\delta_{\nu\nu'}$ is the Kronecker delta function and $k_\nu$ is given by

$$k_\nu = \left( \boldsymbol{k}_{||}^2 + \left( \frac{\nu\pi}{l} \right)^2 \right)^{\frac{1}{2}} . \tag{3.36}$$

This matrix can then be solved for eigenvalues and eigenfunctions to determine the subband energies and wavefunctions normal to the surface respectively. Computationally the Fourier series given by equation 3.34 is truncated after an order $\nu_{max}$, resulting in a $\nu_{max} \times \nu_{max}$ matrix in equation 3.35. The value of $\nu_{max}$ used throughout this thesis is 500 and this was found to be sufficient for all calculations.

Example subband dispersions calculated using the coupled Poisson-MTFA/ Schrödinger approach are shown in figure 3.4. These are for the band bending profiles shown in figure 3.3, with typical CdO parameters. Increased band bending results in deeper subbands, and with sufficient band bending more quantised levels can be confined.

This coupled Poisson-MTFA/Schrödinger approach is significantly more simple and much less computationally demanding than a fully self-consistent non-parabolic Poisson-Schrödinger calculation. This is because the Schrödinger equation needs

to be solved only once for the potential generated by the Poisson-MTFA. The accuracy of the model was confirmed by comparison with fully self-consistent non-parabolic Poisson-Schrödinger for InAs [136, 138]. The agreement between the two approaches is excellent and the computational efficiency of the coupled Poisson-MTFA/Schrödinger approach make it possible to use the simulation within a fitting scheme to extract meaningful parameters from the photoemission experiments undertaken in this thesis.

# CHAPTER 4

# Intrinsic Electronic Properties of As-Grown CdO

## 4.1 Introduction

The electronic properties of single crystal CdO have previously been investigated by photoemission studies [66, 113–116], with all of these studies using a clean CdO surface prepared in UHV, typically by annealing the sample to high temperatures. This process results in a significant lowering of the bulk carrier concentration [54], making it impossible to study intrinsic CdO samples with high carrier concentrations using conventional photoemission techniques. In order to overcome the limitations of the surface preparation, the increased bulk sensitivity offered by HAXPES has been exploited to probe the electronic structure of CdO without the need for surface preparation [79, 139].

The IMFP of photoelectrons is significantly enhanced by using harder x-rays, a phenomenon illustrated by figure 4.1 (a). Here, the IMFP of electrons in CdO has been calculated for a wide range of photoelectron KEs using the TPP-2M formula, described in section 2.1.3.1. If the probing depth is considered to be three times the IMFP (a cut-off of 95% of the signal), then the sampling depth for valence

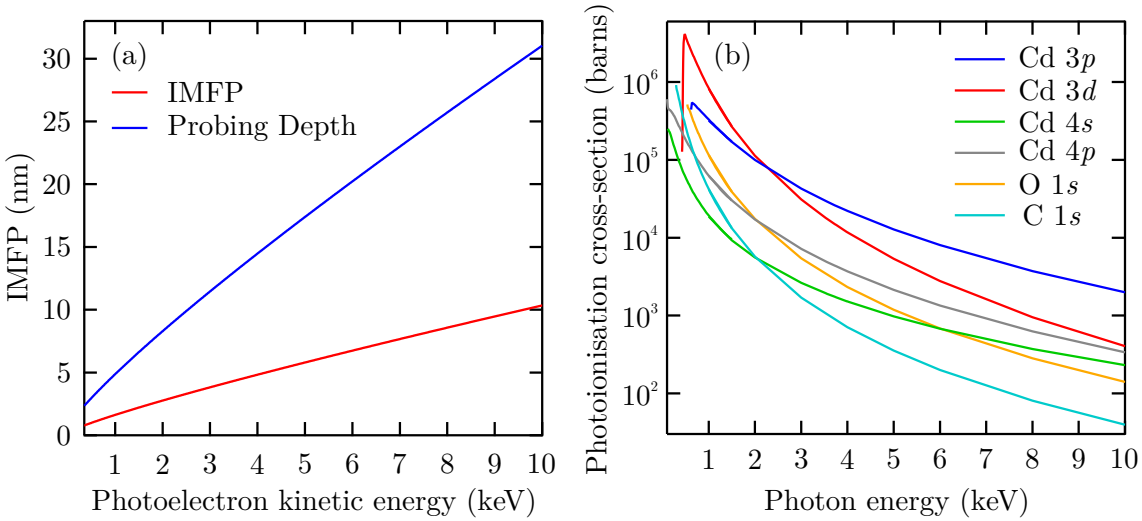


**Figure 4.1.** (a) CdO IMFP calculated using TPP-2M formula (section 2.1.3.1), a probing depth of three times the IMFP is also shown. For photoelectron energies ranging from soft x-ray photoelectron spectroscopy (SXPES) through to HAXPES. (b) The photoionisation cross-sections for the core levels of interest as a function of photon energy. Photoionisation cross-section data from references [93, 95].

electrons with a BE of 2 eV increases from $\sim$ 6 nm for an Al $K_\alpha$ laboratory source ($h\nu = 1486$ eV) to $\sim$ 20 nm using a photon energy of 6054 eV.

The advantage of the longer IMFP offered by HAXPES is offset by the reduction in photoionisation cross sections as the photon energy is increased. This is shown in figure 4.1 (b), where the photoionisation cross-sections of the core levels of interest are shown as a function of photon energy. The Cd $3d$ cross-section decreases by a factor of $\sim$ 100 on moving from a photon energy of 1486 eV to 6054 eV [95]. These smaller cross-sections can be overcome using a synchrotron source to provide extremely high photon fluxes, combined with recent advances in electron analyser design which enable more efficient photoelectron detection.

In this chapter the advantages of HAXPES are exploited in order to study CdO with high carrier concentration. With the enhanced probing depth, the effects of surface contamination are reduced, thereby eliminating the need for in-situ surface preparation. A comparison is made between HAXPES and conventional lab source XPS, and synchrotron SXPES.

## 4.2 Experimental Details

A single CdO sample grown as described in section 2.4, was split in half. One half was annealed in UHV at 600 °C for one hour to lower the carrier concentration, leaving the other in the as-grown condition. Both samples were then transported to the Diamond Light Source in air. The samples were loaded in to UHV at the I09 endstation and no further sample preparation was performed. Following the HAXPES measurements, the samples were transported back to Warwick, and Hall effect measurements were performed, as described in section 2.2.

All photoemission measurements reported in this chapter were performed on the I09 beamline, described in 2.1.8. To allow the depth sensitivity of HAXPES to be assessed, additional soft x-ray data was taken for comparison. For hard x-ray measurements, a channel cut Si(004) monochromator was used in addition to the double crystal monochromator, resulting in a photon energy of 6054 eV and an overall experimental resolution of $\sim$ 250 meV. For the soft x-ray measurements a photon energy of 600 eV was used as it provides an energy resolution comparable to the HAXPES data, while still allowing the O 1$s$ core level to be probed. The soft x-rays were monochromated using a plane grating monochromator, resulting in an energy resolution of $\sim$ 300 meV. All the measurements were performed in the grazing incidence geometry (see figure 2.11) to enhance the count rate, which is achieved by matching the illuminated area to the analyser acceptance. The measurements were performed and at room temperature. The binding energy scale has been referenced to the Fermi edge of each sample.

## 4.3 Results and Discussion

### 4.3.1 Hall Results / Carrier Statistics

Hall effect measurements revealed a bulk carrier concentration and mobility of $n = 2.4 \times 10^{20}$ cm$^{-3}$ and $\mu = 43$ cm$^2$V$^{-1}$s$^{-1}$, respectively, for the as-grown CdO sample. In contrast values of $n = 1.8 \times 10^{19}$ cm$^{-3}$ and $\mu = 110$ cm$^2$V$^{-1}$s$^{-1}$ were obtained from the CdO sample which had been annealed in UHV. This result illustrates the significant reduction in carrier concentration caused by UHV annealing, possibly due to the removal of hydrogen or cadmium interstitials [16]. The increased mobility following UHV annealing suggests an improvement in crystalline quality, supported by the recrystallisation observed by AFM in section 2.4.1, and investigated in more detail by optical spectroscopy measurements, where grain boundary scattering was found to dominate the mobility [38].

Using the two band $\boldsymbol{k} \cdot \boldsymbol{p}$ carrier statistics model (section 3.1.3), with a direct band gap of 2.20 eV, and a bulk conduction band effective mass of $0.24m_0$ [38, 118], the measured bulk carrier concentrations can be converted to a Fermi level position ($E_F$). For the as-grown sample the calculated Fermi level position is 0.52 eV above the CBM, and for the UHV annealed sample the Fermi level is calculated to be 0.09 eV above the CBM. This implies a Fermi level shift of 0.43 eV due to CB filling, this shift is illustrated schematically in panels (a) and (b) of figure 4.2.

#### 4.3.1.1 Band Gap Renormalisation

In degenerate semiconductors, such as CdO, electron-electron ($e$-$e$) and electron-ion ($e$-$i$) interactions cause a narrowing of the band gap, known as band gap renormalisation (BGR). This effect has been observed in single crystal CdO by optical spectroscopy, and in doped polycrystalline samples by photoemission experiments [120, 140]. Within the $\boldsymbol{k} \cdot \boldsymbol{p}$ model, the effects of BGR can be included by

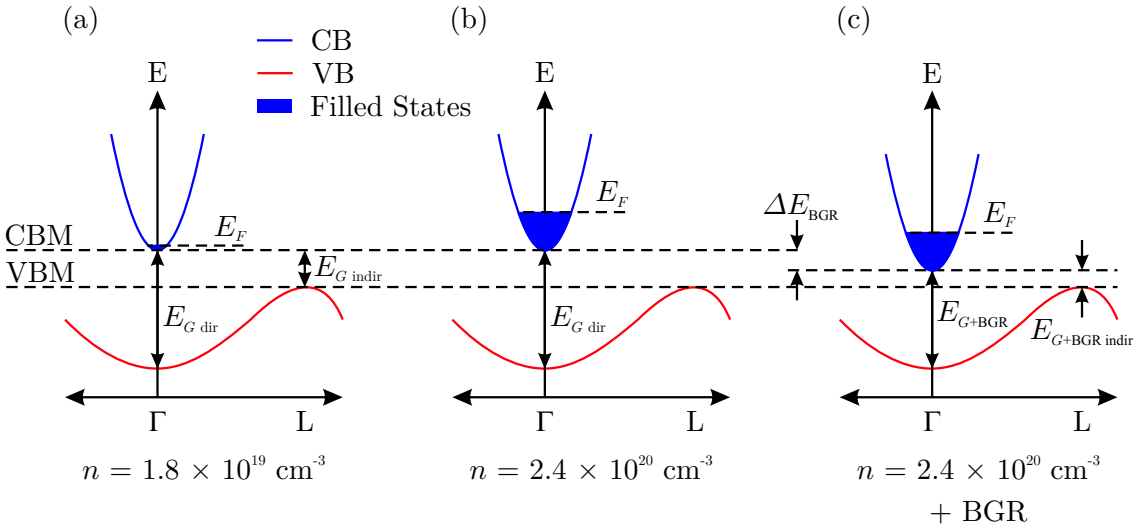


**Figure 4.2.** Band schematic showing the effects of CB filling and band gap renormalisation (BGR). (a) shows CdO with a low bulk carrier concentration, (b) shows a CdO sample with higher carrier concentration and therefore increased CB filling, and (c) shows the higher carrier concentration with BGR also applied. Note the indirect band gap of CdO.

adding interaction terms to the band gap such that

$$E_{G,BGR}(E_F) = E_G + \Delta E_{e\text{-}e}(E_F) + \Delta E_{e\text{-}i}(E_F), \tag{4.1}$$

where $\Delta E_{e\text{-}e}(E_F)$ and $\Delta E_{e\text{-}i}(E_F)$ are the corrections as a result of $e$-$e$ and $e$-$i$ interactions respectively. These are assumed to be negative, with the $e$-$e$ correction given by [141]

$$\Delta E_{e\text{-}e}(E_F) = -\frac{e^2 k_F}{2\pi^2 \epsilon_0 \epsilon_s} - \frac{e^2 k_{TF}}{8\pi \epsilon_0 \epsilon_s}\left[1 - \frac{4}{\pi}\arctan\left(\frac{k_F}{k_{TF}}\right)\right], \tag{4.2}$$

and the $e$-$i$ correction given by

$$\Delta E_{e\text{-}i}(E_F) = -\frac{e^2 n}{\epsilon_0 \epsilon_s r_B^* k_{TF}^3}, \tag{4.3}$$

where $E_F$ and $k_F$ are the Fermi energy and wavenumber respectively. $\epsilon_0$ is the permittivity of free space and $\epsilon_s$ is the static dielectric constant. $k_{TF}$ is the Thomas-

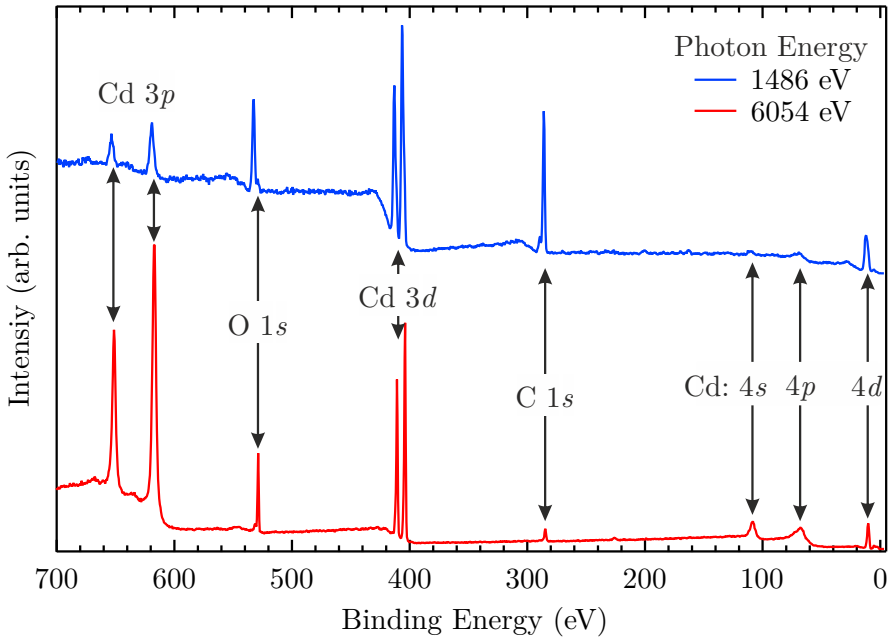


**Figure 4.3.** Comparison of XPS survey spectra taken at Warwick (blue) Al $K_\alpha$ ($h\nu$ = 1486.6 eV) and HAXPES taken at I09 DLS (red) ($h\nu$ = 6054 eV). The intensity of the Cd $3d_{5/2}$ peak has been used for normalisation.

Fermi wavenumber, and $r_B^*$ is the effective Bohr radius, given by

$$k_{TF} = 2\left(\frac{k_F}{\pi r_B^*}\right)^{\frac{1}{2}}, \tag{4.4}$$

$$r_B^* = \frac{4\pi\epsilon_0\epsilon_s\hbar^2}{e^2\langle m^*\rangle}, \tag{4.5}$$

where $\langle m^*\rangle$ is the density of states averaged effective mass. For CdO the effective Bohr radius is $\sim 3.5$ Å.

The effects of BGR are shown schematically in figure 4.2 (c). Performing this BGR calculation for the as-grown CdO sample, a band gap shrinkage of 0.20 eV is predicted, compared to a 0.07 eV shrinkage for the annealed sample. Combining these BGRs with the shifts of the Fermi level due to the Burstein-Moss effect of CB filling previously calculated, a shift in the VBM of 0.30 eV is predicted.

### 4.3.2 Surface sensitivity

A comparison of the survey spectra from the as-grown CdO sample, taken at Warwick using a typical monochromated lab x-ray source ($h\nu$ = 1486.6 eV) and at I09

taken using $h\nu = 6054$ eV are shown in figure 4.3. The spectra are normalised to the Cd $3d_{5/2}$ peak area to allow the relative peak intensities to be observed. It can be seen that the C $1s$ intensity is significantly suppressed at the higher photon energy due to the increased probing depth. This makes the surface a much less significant fraction of the total signal. The C $1s$ cross-section varies very similarly with photon energy as the Cd $3d$, thus making this direct comparison meaningful. The effects of the photoionisation cross-sections can be directly observed as the intensity of the Cd $3p$, $4s$ and $4p$ core levels are all strongly enhanced relative to the Cd $3d$ at the higher photon energy. This can be understood by referring to figure 4.1 (b) where the Cd $3d$ cross-section drops off much more strongly than Cd $3p$, $4s$ and $4p$ with increasing photon energy.

One significant advantage of I09 is the ability to provide both soft and hard x-rays onto the same focus point, this enables a direct comparison of the surface sensitivity of SXPES and HAXPES. Figure 4.4 shows a comparison between the O $1s$ and Cd $3d_{5/2}$ regions obtained using SXPES and HAXPES. At the lower photon energy, the SXPES ($h\nu = 600$ eV) data is much more surface sensitive than the HAXPES ($h\nu = 6054$ eV) data. For the O $1s$ region the sampling depth is estimated to be 18.8 nm for HAXPES compared to 1.3 nm in SXPES. The O $1s$ core level occurs at a KE of $\sim 70$ eV, and for a photon energy of 600 eV this coincides with the minimum escape depth at the bottom of the universal curve (figure 2.4). This results in a factor of $\sim 14$ increase in sampling depth between SXPES and HAXPES. This difference is most clearly illustrated by the contamination peak in the O $1s$ region at $\sim$531.5 eV - assigned principally to $CdCO_3$ and atmospheric contaminants [113], as this feature is strongly enhanced in the SXPES data on both the as-grown and annealed samples. With regards to the as-grown sample, shown in figure 4.4 (c), this contamination peak dominates the spectrum, making line shape analysis very difficult and somewhat unreliable. This situation is much improved by employing HAXPES where the sensitivity to the surface, and therefore

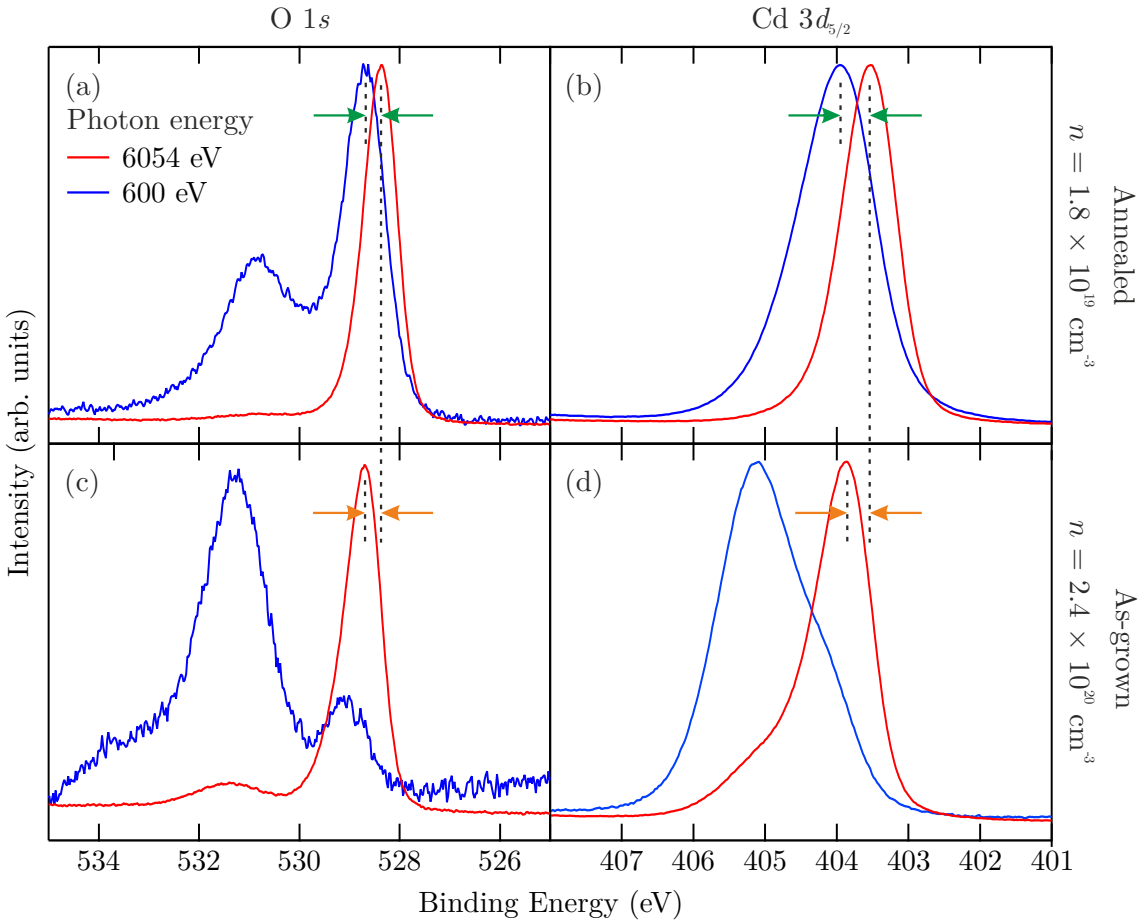


**Figure 4.4.** Comparison of HAXPES (red) and SXPES (blue) spectra taken with $h\nu = 6054$ eV and $h\nu = 600$ eV respectively. (a) O 1$s$, (b) Cd 3$d_{5/2}$ for the annealed sample ($n = 1.8 \times 10^{19}$ cm$^{-3}$). (c) O 1$s$, (d) Cd 3$d_{5/2}$ for the as-grown sample ($n = 2.4 \times 10^{20}$ cm$^{-3}$). The peak shifts indicated by the green arrows are assigned to surface band bending effects, and the orange arrows to CB filling as discussed in the main text.

the contamination component, is very much reduced. Hence by careful peak fitting the contamination component can straight forwardly be separated from the main peak.

The situation is very similar in the Cd 3$d_{5/2}$ region, shown in figure 4.4 (b) and (d). Although no significant contamination component is visible on the annealed sample, the as-grown sample displays a large contamination component at ∼405.1 eV, assigned to $CdCO_3$ or $Cd(OH)_2$ [115]. This component dominates the spectra, making the core level shape appear almost mirrored, and again it is much reduced at higher photon energies. This allows the core level line shape to be analysed while still

incorporating the reduced contamination component when performing peak fitting.

A peak shift of $\sim 0.4$ eV towards lower BE can be seen on moving from SXPES to HAXPES in the CdO components of the O $1s$ and Cd $3d_{5/2}$ regions indicated by the green arrows. These shifts are assigned to the band bending present at CdO surfaces. By using a higher photon energy the surface sensitivity is decreased, and as CdO exhibits downwards band bending, a peak shift to lower binding energy should be expected. This effect has recently been exploited in an investigation of $SnO_2$ in order to map out the band bending profile [142]. The peak shifts observed here are $\sim 0.4$ eV, consistent with the large downward band bending previously observed on CdO [66, 113].

The CdO components are also broader in the SXPES data than the HAXPES data this change is larger than the slightly reduced experimental resolution, and can be observed most clearly in figure 4.4 (b), where the peak FWHM is $\sim 1.2$ eV for SXPES compared to $\sim 0.9$ eV in HAXPES. This is also assigned to band bending which should result in an asymmetrical line shape, from Cd in differing electrical potentials, however it may also result from stoichiometry differences at the surface.

### 4.3.3 Valence Band

The VB spectra for the as-grown and annealed CdO samples are shown in figure 4.5. A binding energy shift due to CB filling is clearly visible, and by linear extrapolation of the leading edge [143], the VBM to $E_F$ separations ($\xi$) are found to be $1.29 \pm 0.07$ eV and $0.99 \pm 0.07$ eV for the as-grown ($n = 2.4 \times 10^{20}$ cm$^{-3}$) and annealed ($n = 1.8 \times 10^{19}$ cm$^{-3}$) samples respectively. This gives a VBM shift of $0.30 \pm 0.10$ eV, arising from the increased carrier concentration. This measured shift is less than the 0.43 eV predicted by CB filling in section 4.3.1. However, if BGR is also considered, as discussed in section 4.3.1.1, then a VBM shift of 0.30 eV is predicted, in excellent agreement with the experimental result. The success of this bulk model also serves to illustrate the bulk-like sensitivity of the HAXPES technique.

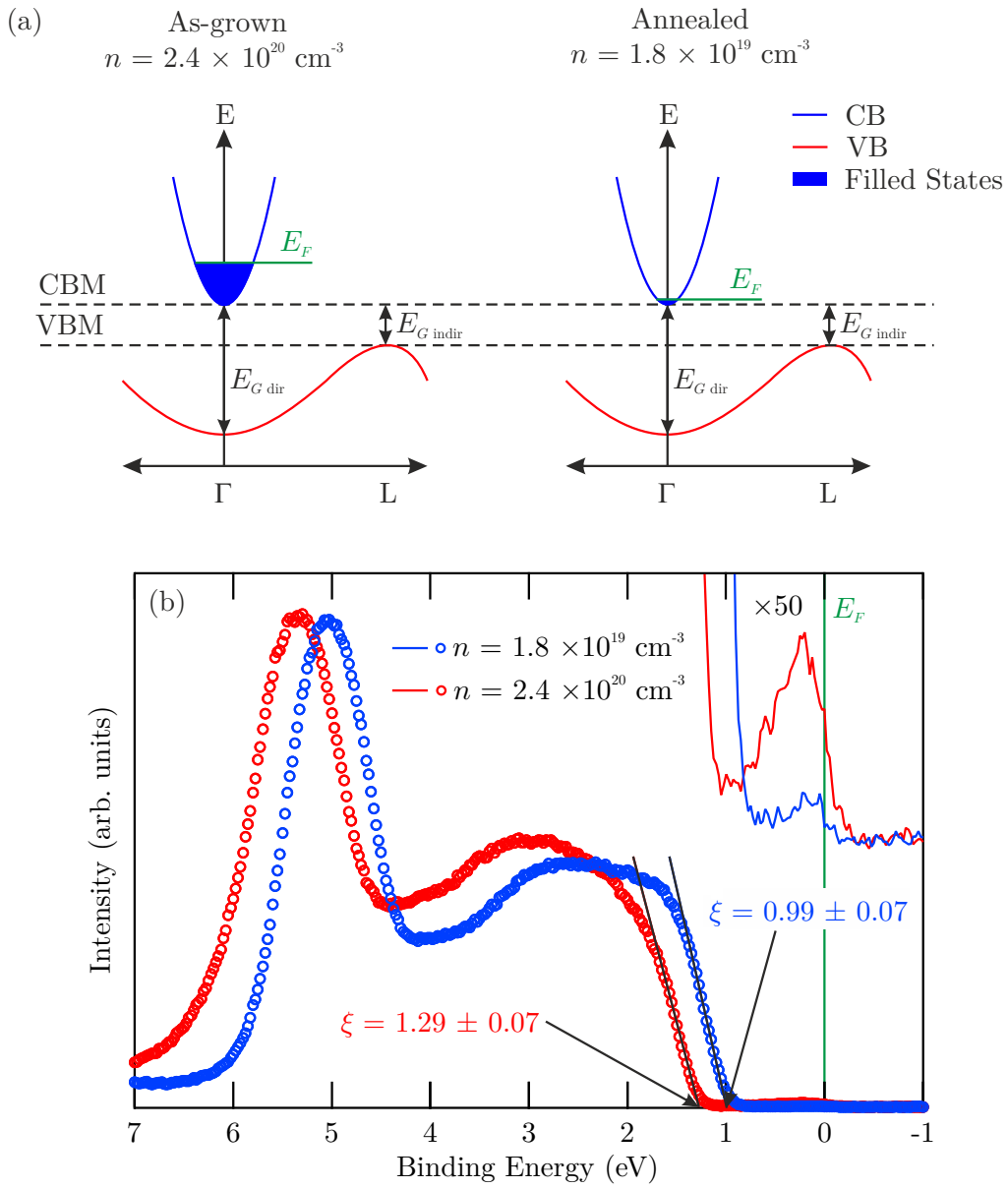


**Figure 4.5.** (a) A band schematic illustrating the band filling present in the as-grown sample. (b) HAXPES VB spectra for as-grown CdO ($n = 2.4 \times 10^{20}$ cm$^{-3}$) and annealed CdO ($n = 1.8 \times 10^{19}$ cm$^{-3}$) samples, a ×50 magnification of the CB region is shown to allow the CB states to be clearly observed. The extrapolations of the VB leading edge used to obtain the VBM are also shown. The data was taken with $h\nu = 6054$ eV.

Just below the Fermi level a small feature due to photoelectrons from filled CB states is clearly visible, shown magnified (×50) in figure 4.5. The intensity of this feature is significantly enhanced for the as-grown sample, as expected in the case of increased bulk CB filling. The bandwidth of this feature is 0.7±0.1 eV for the as-grown sample and 0.4±0.2 eV for the annealed sample. These values are both significantly in excess of the predicted CB filling using measured Hall carrier concentrations and carrier statistics, indicating that extra electrons at deeper binding energies are present. There are two possible explanations for this observation. Firstly the CB feature could incorporate a plasmon satellite, as has been observed previously for example in $Na_xWO_3$, and simple metals [144, 145]. Alternatively, clean CdO surfaces are known to exhibit downward band bending and associated electron accumulation, giving rise to quantized surface states at higher binding energies than are present in the bulk [66, 116]. These two possibilities are discussed later in the context of the core level line shapes. Both the CB state and valence feature at $\sim$ 5.5 eV are strongly enhanced relative to the top of the VB, compared to previous lower photon energy measurements [113, 115]. This is due to the pronounced Cd 5$s$ character of both states [37, 115] which exhibit a slower decrease in photoionisation cross-section with increasing photon energy than either the O 2$p$ or Cd 4$d$ states which compose the rest of the valence band. This is discussed in more detail in chapter 5 and reference [146].

### 4.3.4 Core Levels

The Cd 3$d$ peaks for the as-grown and annealed samples are shown in figure 4.6. In agreement with the VBM result, a $0.30 \pm 0.05$ eV peak shift is observed arising from the increased carrier concentration of the as-grown sample. The measured peak shapes also exhibit significant asymmetry, demonstrated by the inclusion of a symmetrical Voigt peak fitted to the low BE side of the Cd $3d_{5/2}$ peak. For the higher carrier concentration a more significant shoulder is observed on the high BE side of the peak, as observed previously on CdO [115]. This enhanced asymmetry is caused

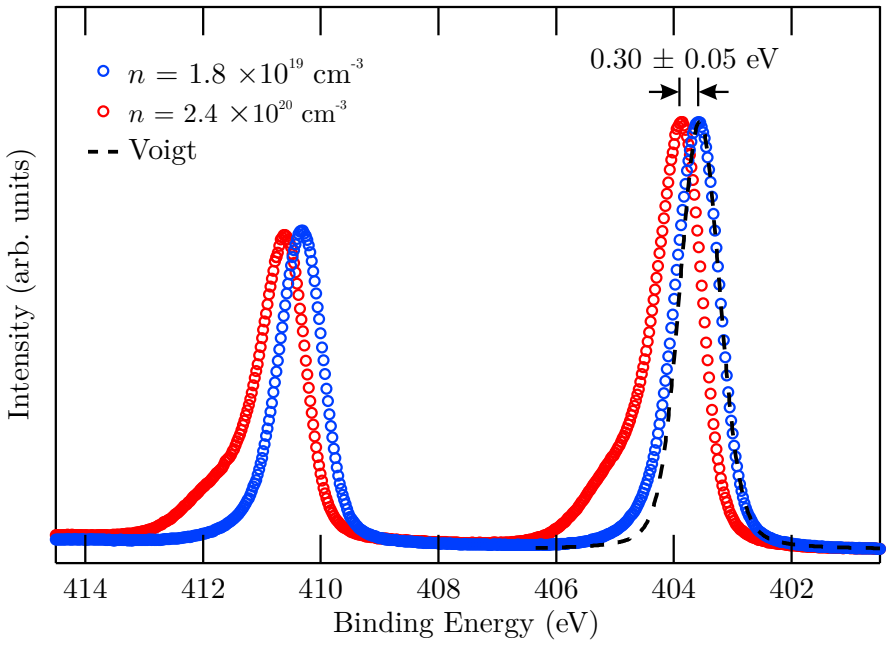


**Figure 4.6.** HAXPES Cd $3d$ spectra for both as-grown ($n = 2.4 \times 10^{20}$ cm$^{-3}$) and annealed ($n = 1.8 \times 10^{19}$ cm$^{-3}$) CdO samples. A symmetrical Voigt peak fitted to the low BE side of the Cd $3d_{5/2}$ is also shown to allow the asymmetry to be observed.

by final state screening effects which can be enhanced due to the downwards band bending and associated electron accumulation present at the surface, as previously observed for $SnO_2$, $In_2O_3$ and InN [147–150]. Peak fitting was performed in order to investigate these final state screening effects in more detail.

#### 4.3.4.1 Peak Fitting

Two different phenomenological models have been proposed in the literature to account for the core level lineshapes observed in photoemission spectra from metallic oxides [153]. The first model, developed by Kotani et al. [151, 152], attempts to account for core level lineshapes observed in transition metal compounds. This approach has been applied to a range of metal oxide compounds including; $Na_xWO_3$ [144, 154], $LiTi_2O_4$, $MoO_2$ [153], $PbO_2$ [155], Sn-doped $In_2O_3$ [156] and Sb-doped $SnO_2$ [157]. This model recognises that when the Coulomb interaction between a core hole and an orbital contributing to the CB, exceeds the occupied CB width. The potential associated with the core hole will then create a localised state on the ionised atom as shown in figure 4.7. Two different final states then become

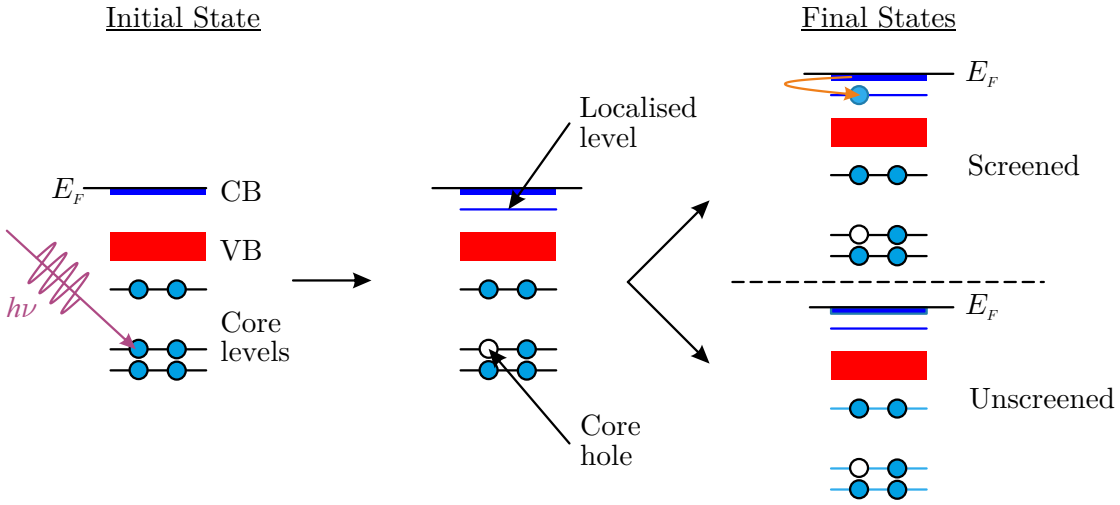


**Figure 4.7.** A schematic representation of the Kotani et al. [151, 152] core screening model described in the main text. The photoionisation event creates a core hole, the Coulomb interaction of this core hole creates a localised level, giving rise to two possible final states.

available, the first where an electron can drop from the CB into the localised state giving a screened final state, or secondly the localised level can remain empty giving an unscreened final state. Within this model, the probability of final state screening should increase with increasing carrier density. The peaks associated with an unscreened final state will be lifetime broadened to give a characteristically Lorentzian line shape.

The second possible lineshape model treats the low binding energy component as the "main" peak, and the higher binding energy peak as an unusually strong plasmon satellite broadened by the conduction electron scattering rate. The theory of plasmon satellites in low electron density metals suggests that the intensity of the high binding satellites should increase with decreasing electron density ($n$) according to an $n^{-1/3}$ power law [144]. For a number of closely related systems such as Sb-doped $SnO_2$, $PbO_{2-x}$ and Sn-doped $In_2O_3$, it has been shown that satellite energies are indeed close to plasmon energies measured by other techniques e.g. infrared reflectance spectroscopy or electron energy loss spectroscopy [147, 149, 158].

Both of these models predict very similar core level line shapes, i.e. two Lorentzian

**Table 4.1.** Numerical peak fitting results for Cd $3d_{5/2}$ and O $1s$ core levels shown in figure 4.8. BE and FWHM are in eV and have errors of ±0.05 eV. The contamination peaks have been excluded for the relative area (R.A.) calculation. $E_P$ is the plasmon energy, given by the separation between the screened and unscreened components, and has an error of ±0.07.

| Peak | $n$ ($cm^{-3}$) | Component | BE | FWHM | R.A. (%) | $E_p$ (meV) |
|---|---|---|---|---|---|---|
| Cd $3d_{5/2}$ | $1.8 \times 10^{19}$ | Screened | 403.43 | 0.67 | 24 | |
| | | Unscreened | 403.68 | 0.90 | 76 | 250 |
| Cd $3d_{5/2}$ | $2.4 \times 10^{20}$ | Screened | 403.79 | 0.71 | 55 | |
| | | Unscreened | 404.25 | 0.90 | 45 | 460 |
| O $1s$ | $1.8 \times 10^{19}$ | Screened | 528.33 | 0.66 | 45 | |
| | | Unscreened | 528.57 | 0.88 | 55 | 240 |
| O $1s$ | $2.4 \times 10^{20}$ | Screened | 528.64 | 0.69 | 57 | |
| | | Unscreened | 529.10 | 0.93 | 43 | 460 |

peaks representing either the screened and unscreened peaks of the localised level model, or the main and plasmon satellite peaks in the case of the plasmon model. To account for experimental resolution the peaks have been broadened by a Gaussian, resulting in Voigt line shapes. Additionally as the samples have not undergone surface preparation in UHV, a contamination component remains, which is represented by an additional Voigt peak. Combined with a Shirley background, this approach has been used to fit to the Cd $3d_{5/2}$ and O $1s$ core levels. In principle, the Cd $4d$ peak should exhibit a similar line shape. However, the Cd $4d$ levels in CdO are extremely shallow ($\sim$ 10 eV) and hybridise strongly with the O $2p$ levels, complicating detailed peak fitting [114, 115]. This is investigated further in chapter 5. Therefore the Cd $3d_{5/2}$ and O $1s$ core levels are used for performing the peak fitting in this instance, with the resulting fits shown in figure 4.8 and the numerical results in table 4.1.

Figure 4.8 (a) and 4.8 (b) show curve fits to the O $1s$ and Cd $3d_{5/2}$ core lines for the annealed sample while the corresponding fits for the as-grown sample are shown in 4.8 (c) and 4.8 (d). As expected, the contamination component is much weaker in both the O $1s$ and Cd $3d_{5/2}$ for the annealed sample, as was observed when

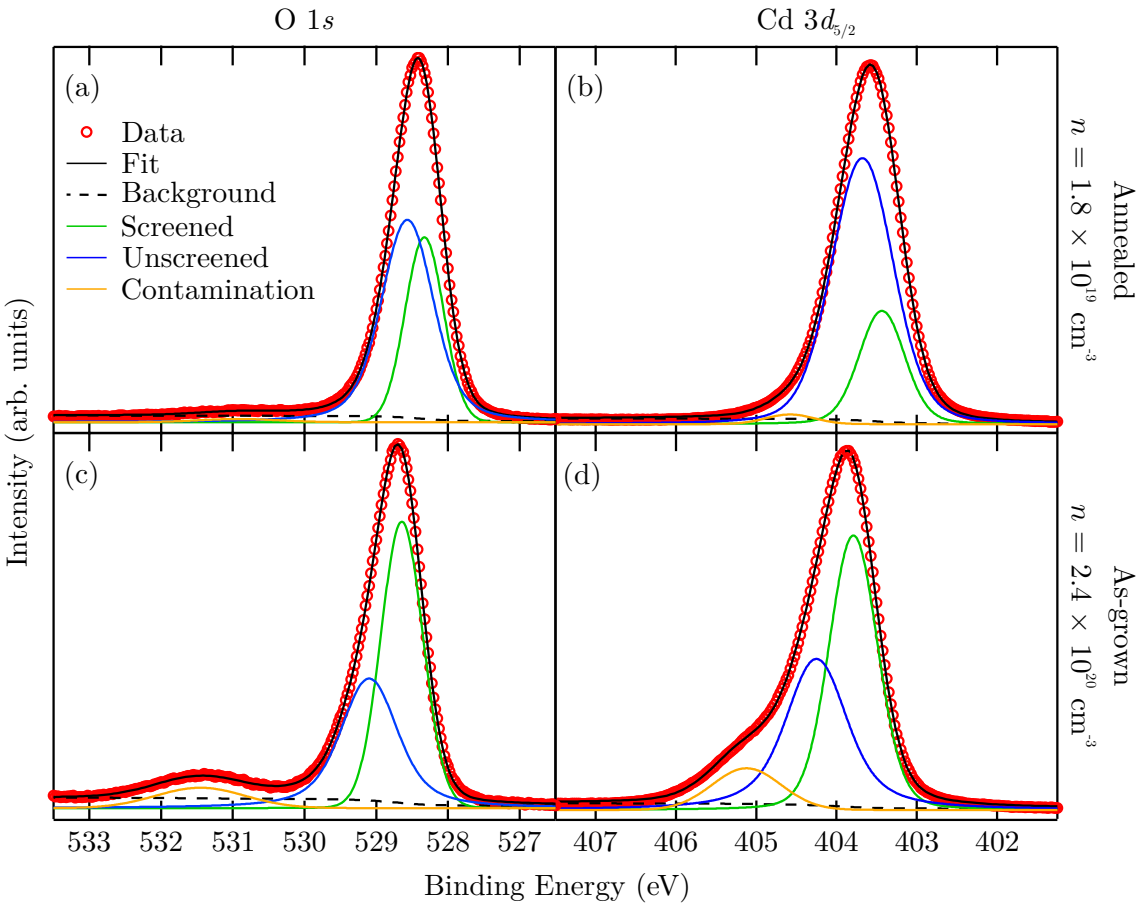


**Figure 4.8.** HAXPES spectra and fits for (a) O 1$s$, (b) Cd 3$d_{5/2}$ for the annealed sample ($n = 1.8 \times 10^{19}$ cm$^{-3}$). (c) O 1$s$ and (d) Cd 3$d_{5/2}$ regions for the as-grown sample ($n = 2.4 \times 10^{20}$ cm$^{-3}$). The spectra have been fitted using the peak model described in the text.

comparing the SXPES and HAXPES.

The spectral weight associated with the low binding energy "main" or screened peak is enhanced, as expected, for the sample with higher carrier density in both the Cd 3$d_{5/2}$ and O 1$s$ regions. The energy separation between the screened and unscreened peaks (main and plasmon satellite, in the plasmon model) is consistent for curve fits of the two different core levels, with a larger separation for the higher carrier density sample. In addition, there is a well-defined peak shift to higher binding energy for the higher carrier density sample, resulting from increased occupation of the conduction band and BGR discussed previously. Finally, the relative intensity of the high binding energy component is weaker in the O 1$s$ region than in the Cd 3$d_{5/2}$ region for both samples. This observation is qualitatively consistent with

the plasmon model because conduction band states in CdO are of predominantly Cd $5s$ character with a weaker O $2p$ contribution arising from O $2p$-Cd $5s$ hybridisation. Therefore, a cadmium core hole is more likely to excite plasmons than an oxygen core hole. It is more difficult to understand the intensity differences utilising the final state screening model. A previous interpretation of core lineshapes in CdO by Piper et al. [113] were based on the proposed existence of $CdO_2$ as a surface phase. These experiments contradict this assignment as the surface contribution in HAXPES is very much lower than in conventional photoemission, but nonetheless the satellites remain strong.

#### 4.3.4.2 Plasmon Satellites

If the two peaks are interpreted as a main peak and a plasmon satellite, the splitting of the two components can be used to obtain a carrier density using the relation [108]

$$E_p = \hbar \left( \frac{ne^2}{m^* \varepsilon_0 \varepsilon(\infty)} \right)^{\frac{1}{2}}. \tag{4.6}$$

Here $E_p$ is the plasmon energy, $\varepsilon(\infty)$ is the high frequency dielectric constant, and $m^*$ is the effective mass at the Fermi level. The band edge effective mass is taken as $m^* = 0.24m_0$ and $\varepsilon(\infty) = 5.4$, [34, 38, 159]. A plasmon energy of $E_p = 245$ meV (obtained by averaging the peak separations extracted from the Cd $3d_{5/2}$ and O $1s$) for the annealed sample this gives a carrier density of $n = 5.9 \times 10^{19}$ cm$^{-3}$, whereas $E_p = 460$ meV for the as-grown sample gives $n = 2.5 \times 10^{20}$ cm$^{-3}$. The agreement with Hall measurement is excellent for the high carrier concentration sample, illustrating the bulk-like sensitivity of HAXPES, and suggesting there is no significant contribution to the carrier density from an electron accumulation layer. For the annealed sample the carrier density obtained from the plasmon separation is notably higher than that obtained from Hall measurements. This indicates the electron accumulation layer plays a significant role in the final state screening, where it contributes a significant fraction of the electron density within the probing depth.

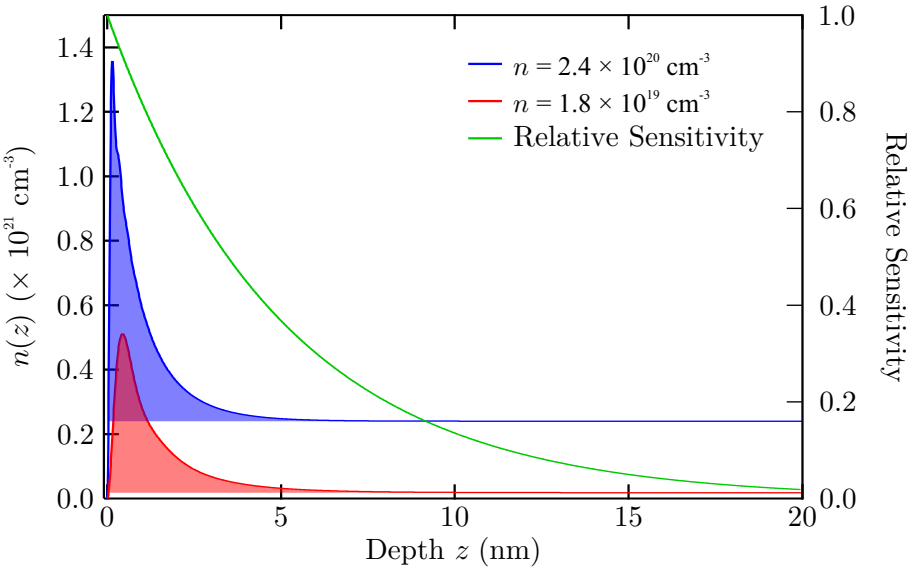


**Figure 4.9.** Electron depth distributions calculated using the method described in section 3.2, with $V_{BB} = -1$ eV and carrier densities equal to the Hall measured values. The shaded regions indicate the electrons considered as in the accumulation layer, when calculating their percentage. The green line shows the relative depth sensitivity as an exponential decay using 6 nm as the IMFP.

In order to observe what effect the accumulation layer would have on a HAXPES measurement, the depth dependent electron concentration has been calculated. This was achieved using the Poisson-MTFA approach described in section 3.2, for the bulk carrier densities obtained from the Hall effect measurements, using a typical downwards band bending of $V_{BB} = -1$ eV. The results of these calculations are shown in figure 4.9. By weighting the electron density by the relative depth sensitivity illustrated by the green curve, plotted as $e^{-z/\lambda}$ and where the IMFP is assumed to be 6 nm, the percentage of electrons in the accumulation layer relative to the total number of electrons probed can be calculated. For the annealed sample 89% of the probed electrons are in the accumulation layer, compared to 40% for the as-grown sample. This qualitatively explains why the plasmon energy observed for the annealed sample corresponds to a carrier density significantly higher than the bulk. The very close agreement of the as-grown result however suggests either the true IMFP is significantly larger than 6 nm, or such a large accumulation layer is not present at the as-grown surface, maybe due to passivation by the surface contamination. This seemingly small contribution of an electron accumulation layer in turn

suggests the large bandwidth of the observed CB feature on the as-grown sample is likely due to a plasmon satellite. This is supported by the observed CB bandwidth of $0.7 \pm 0.1$ eV which would be consistent with a 460 meV plasmon separation observed on the core levels. For the annealed sample, the observed CB bandwidth probably contains a contribution from both a plasmon satellite and quantum well states which cannot be distinguished using HAXPES.

## 4.4 Conclusions

HAXPES has been used to study the intrinsic electronic properties of CdO(100) single crystal thin films. The use of higher energy photons and the associated increase in probing depth allowed the CdO thin films to be studied as-grown, avoiding the reduction in bulk carrier concentration caused by annealing. The effects of CB filling on the Fermi level position were clearly observed, and band gap renormalisation was found to be significant when analysing the VBM and core level shifts. The effects of plasmons, or final state screening on the core level line shapes was observed, revealing a dependence on the carrier concentration. The plasmon energy, extracted using peak fits, was converted to carrier density and showed excellent agreement with the Hall measurements for the as-grown sample. This supports the conclusion that the observed bandwidth of the CB state on the as-grown sample is largely due to a plasmon satellite. For the annealed sample, the plasmon energy indicated a higher carrier concentration than obtained from Hall measurement, suggesting electron accumulation is playing a significant role in the final state screening effects and the resulting core-level lineshapes. This conclusion was supported by analysing the percentage of probed electrons in the accumulation layer, which is significantly higher for the annealed sample. These results indicate that care must be taken when analysing the BE and lineshapes of core-levels of oxide semiconductors in the presence of high carrier concentrations, electron accumulation and final state screening effects. Further theoretical work should be directed at modeling the core-level line-

shapes in such systems to allow the contributions arising from differing final state effects (screening or plasmons) to be unambiguously determined.

In this chapter HAXPES has been shown to be a powerful technique for the investigation of oxide semiconducting materials, especially where in-situ preparation and surface treatment can otherwise significantly alter the intrinsic material properties. For this reason using HAXPES to study a material's bulk properties can provide a potential method for the investigation of the intrinsic sources of high carrier concentrations in TCO materials.

# CHAPTER 5

# Investigation of the VB Orbital Character of CdO

## 5.1 Introduction

In order to exploit CdO in a number of potential applications a detailed knowledge of the electronic structure of the material is required [16]. In particular, determining the band gap is crucial. However, many current theoretical approaches predict CdO to be a semi-metal [160]. This is a result of the underestimation of the binding energy of the Cd $4d$ states, which results in strong $p$-$d$ hybridisation in the VB and a reduction of the band gap. There have been several theoretical attempts to correct this problem including the use of hybrid functionals [37, 161] and $GW$ quasiparticle calculations [162, 163]. These approaches have had some success in predicting the location of the shallow Cd $4d$ states and the band gap, however, they are also computationally complex and therefore less widely applied.

In order to assess the merits of these theoretical approaches, comparisons with experimental data need to be made. Photoemission is an ideal technique for this as it essentially allows the VB DOS to be probed directly. There have been two previous publications comparing theoretical predictions to experimental photoemission data

for CdO, King et al. [115] and Dou et al. [114]. The King et al. study used epitaxial thin films of CdO measured with a photon energy of 1486.6 eV, compared with quasi-particle corrected DFT calculations using the HSE03 functional. The Dou et al. study used polycrystalline CdO samples measured with XPS ($h\nu = 1486.6$ eV) and UPS which was compared to both Hartree-Fock and DFT calculations.

In this chapter syncrotron radiation photoelectron spectroscopy (SR-PES) has been used to obtain both HAXPES data of the CdO VB and Cd $4d$ regions for comparison to DFT, and a series of CdO VB spectra over a range of photon energies to allow the VB orbital character to be investigated in more detail. With its higher incident photon energy (typically $> 5$ keV), HAXPES is a preferred technique for comparison with theoretical calculations as it is more bulk sensitive than conventional photoemission [164], allowing for better comparison with the theoretical bulk calculations. An additional benefit is the smooth variation of photoionisation cross-sections at high photon energies, allowing trends to be more readily observed. Three DFT functionals have been applied (LDA, PBE-GGA, and LDA+$U$), these were chosen due to their widespread availability and relative computational simplicity. The latter, LDA+$U$ [165–167] is where an on-site, orbital dependent Coulomb term is added to the LDA potential, allowing the position of the Cd $4d$ states to be corrected and should therefore improve the associated theoretical predictions.

## 5.2 Experimental Details

Soft and hard x-ray photoelectron spectra were obtained at the I09 beamline of Diamond Light Source, UK, described in section 2.1.8. Hard x-rays ($h\nu \geq 2500$ eV) were monochromated using a cooled Si(111) double crystal monochromator. To maintain sufficient energy resolution at the two highest photon energies an additional Si channel-cut high resolution monochromator, Si(444) for $h\nu = 7935$ eV and Si(004) for $h\nu = 6054$ eV, was used. Soft x-rays ($h\nu = 600$ eV) were monochromated using a plane grating monochromator (300 lines/mm). The endstation is equipped

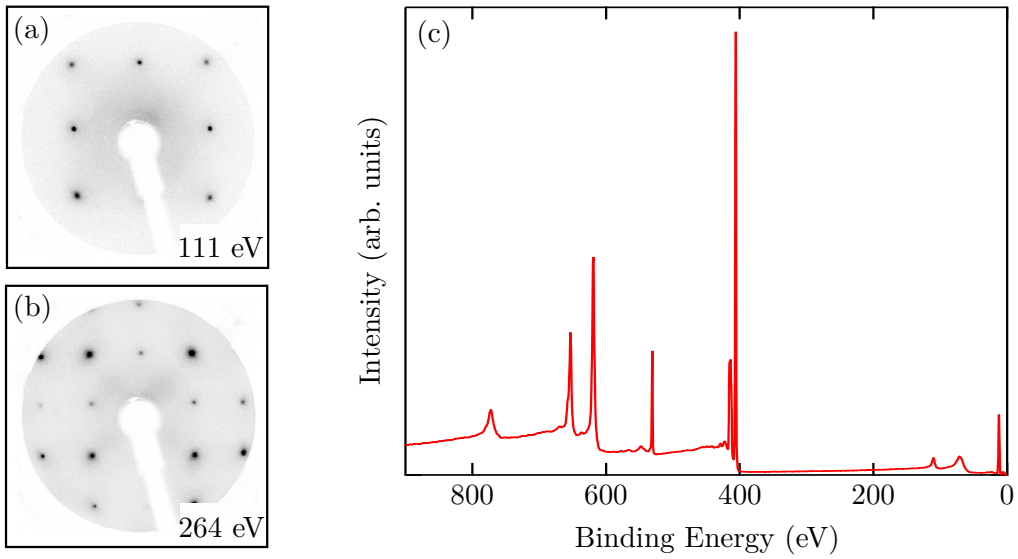


**Figure 5.1.** LEED (a,b) and XPS spectra (c) obtained from the CdO sample following surface preparation by 550 °C annealing. (a) and (b) show sharp $(1 \times 1)$ LEED patterns obtained at 111 eV and 264 eV respectively, indicating good surface order (the images are inverted for clarity). (c) XPS survey spectra of the clean CdO surface obtained using $h\nu = 2500$ eV, no contamination peaks are observed.

with a VG Scienta EW4000 electron analyser with ±30° angular acceptance. In the experimental geometry at I09, shown in figure 2.11, the photon beam is perpendicular to the electron emission direction. The photon beam is polarised in the plane of the orbit (horizontally) resulting in the electric vector being aligned with the electron emission direction. The sample was placed in a grazing incidence geometry ($\sim 5°$), with the surface normal in the plane defined by the photon beam and electron emission direction ($p$-polarized), thereby significantly enhancing the count rate. The experiments were performed at room temperature. The total experimental energy resolution is $< 0.6$ eV, for all photon energies. All experimental data are shown with energy scales referenced to the valence band maximum to allow for comparison to the theoretical calculations.

A CdO sample, as described in section 2.4, was loaded into UHV conditions at the I09 beamline of Diamond Light source. The sample was prepared in UHV by annealing at 550 °C for 45 minutes. This resulted in a clean surface with a sharp $(1 \times 1)$ LEED pattern as shown in figure 5.1 (a) and (b), and no contamination is

visible by core level PES, shown in figure 5.1 (c).

## 5.3 Computational Details

### 5.3.1 Density Functional Theory

Density functional theory (DFT) calculations were performed using the full-potential linearised augmented-plane wave (FP-LAPW) method with local orbitals [124], as implemented in the ELK open source code [168]. Calculations were performed on CdO in the rocksalt structure. Three different DFT functionals were applied;

- Perdew-Zunger local density approximation (LDA) [169].
- Perdew-Burke-Ernzerhof Generalized Gradient Approximation (PBE-GGA) [128].
- LDA+$U$ approach within the fully localised limit (FLL) [165–167].

The difficulty in applying the LDA+$U$ method is choosing a suitable value of $U$. Here a theoretically calculated value of $U = 2.34$ eV, as suggested by Janotti et al. [170], is used and applied to the Cd $4d$ states. Spin-orbit coupling was not considered in the calculations however it effects are expected to be small.h

Structural optimization was conducted with each functional by performing calculations over a range of lattice constants ($a$), and fitting the resulting energy-volume curve with the Murnaghan EOS [171], as displayed in figure 5.2. From these fits the equilibrium lattice parameter was obtained, and this was used when calculating the band structures and partial density of states (PDOS).

Convergence tests with respect to the plane wave cut-off and $k$-point mesh were carried out by increasing the values until the total energy was constant. This indicates the results are numerically converged to $\sim 5$ meV. The wavefunctions inside the muffin-tins were expanded up to $l_{max} = 8$ and the plane waves were expanded

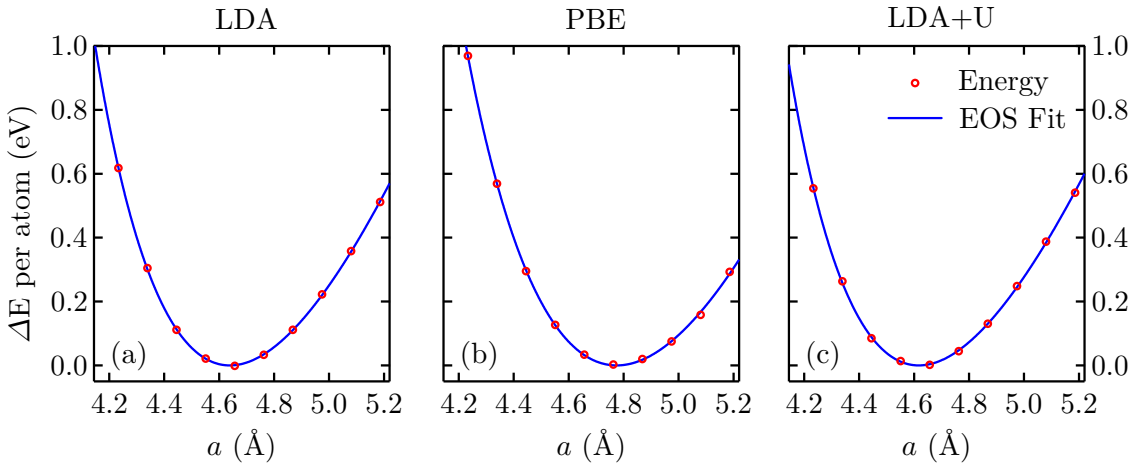


**Figure 5.2.** Energy as a function of lattice constant calculated for each of the DFT functionals. The red points represent the calculated values, and the blue line is a fit using the Murnaghan equation of state equation of state (EOS) [171]. The minimum energy value allows the theoretical lattice constant to be extracted, given in table 5.1.

with a cut-off of $R_{min}^{MT} \times K_{max} = 8.5$, where $R_{min}^{MT}$ is the smallest muffin tin radius and $K_{max} = |\mathbf{G} + \mathbf{k}|$ the maximum value of the wave vector. The muffin-tin radii were chosen as $R_{Cd}^{MT} = 1.35$ Å and $R_{O}^{MT} = 0.94$ Å. A $k$-mesh of $8 \times 8 \times 8$ was found to be sufficient for all calculations.

### 5.3.2 Experimental Comparison

In the regime of high photon energy the DOS available in the final state is so large the measured spectrum reflects the DOS in the initial state, i.e that of the sample. The dependence of the spectra on photon energy therefore depends on the strength of the interaction of the incoming photon with the photoelectron, this varies with photon energy and electron orbital, given by the photoionisation cross-sections. DFT has been used to calculate the orbitally resolved partial density of states (PDOS), and to allow comparison with experimental data the PDOS needs to be weighted by the one-electron photoionisation cross-sections, including an asymmetry correction. To obtain these one-electron photoionisation cross-sections, the tabulated values of the subshell photoionisation cross-sections, calculated by Trzhaskovskaya et al. [91, 97] were summed and divided by the orbital occupancy of a free atom. As the

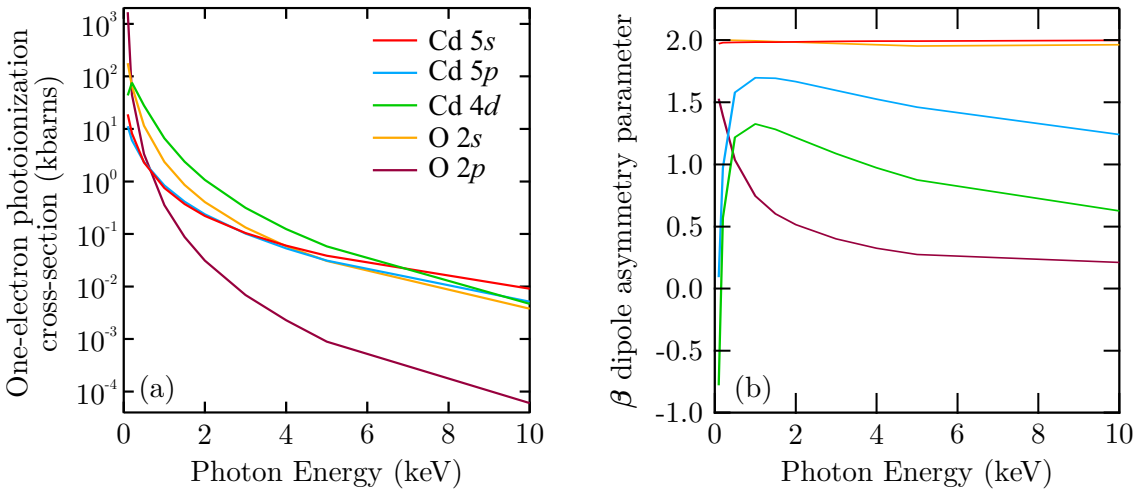


**Figure 5.3.** (a) One-electron photoionisation cross-section and (b) $\beta$ dipole asymmetry parameter for the orbitals constituting the CdO valence band. Shown for photon energies 0.1 to 10 keV. Note the logarithmic scale of the cross-sections. Data from Trzhaskovskaya et al. [91, 97].

Cd $5p$ shell is unoccupied in a Cd atom, the cross-section was estimated by applying the In $5p$/In $5s$ ratio to the Cd $5s$ cross-section. The Cd $5p$ dipole asymmetry parameter was assumed to be equal to the In $5p$ dipole asymmetry parameter, a valid approach as the dipole asymmetry changes only weakly with atomic number [91, 97]. The resulting one-electron photoionisation cross-sections and $\beta$ dipole asymmetry parameters are shown in Figure 5.3.

The differential cross-section for linearly polarised light is given by equation 2.11. In the geometry used at I09 the photon propagation direction is in the plane defined by the polarization and electron emission direction, therefore $\phi = 0$. $\theta$ is defined as the angle between the polarization direction and the electron emission direction, considering the $\pm 30°$ angular acceptance of the electron analyser, equation 2.11 should be integrated in the range $-30 \leq \theta \leq 30$

$$\sigma_i^{total} = \frac{\sigma_i}{4\pi} \int_{-30}^{30} 1 + \underbrace{\beta P_2(\cos\theta)}_{\text{dipolar}} + \underbrace{(\delta + \gamma \cos^2\theta)\sin\theta}_{\text{non-dipolar}} \, \mathrm{d}\theta \tag{5.1}$$

$$= \frac{\sigma_i}{96\pi} \left[ 8\pi + \beta(9\sqrt{3} + 2\pi) \right]. \tag{5.2}$$

As the non-dipolar term has odd parity, after integration over a symmetrical in-

**Table 5.1.** Comparison of the key numerical results from experiment and DFT. The values shown are: lattice parameter $a$, direct band gap ($E_G^{dir}$), indirect band gap ($E_G^{ind}$) (negative values indicate semimetallic behaviour), the VB width ($\Delta$ VB) and location of the Cd $4d$ states with respect to the VBM. All energies are in eV.

| | $a$ (Å) | $E_G^{dir}$ | $E_G^{ind}$ | $\Delta$ VB | $4d$ states |
|---|---|---|---|---|---|
| Exp. | 4.695 [20] | 2.18 [120] | $\sim 0.9$ [36] | $\sim 4.8$ | $\sim -8.70$ |
| LDA | 4.639 | 1.12 | $-0.45$ | 4.72 | $-6.76$ |
| PBE | 4.775 | 0.68 | $-0.51$ | 3.98 | $-6.58$ |
| LDA+$U$ | 4.619 | 1.34 | 0.21 | 4.18 | $-8.60$ |
| HSE 06[a] | 4.720 | 2.18 | 0.89 | 4.45 | $-7.4$ |
| $GW$[b] | 4.650 | 2.88 | 1.68 | $\sim 4.75$ | $\sim -9$ |

[a] Hybrid functional calculation, Burbano et al. [37]
[b] $GW$ quasiparticle calculation, Dixit et al. [162]

terval this term gives no contribution, and therefore there is no dependence on the non-dipolar asymmetry parameters. Equation 5.2 is used to calculate the total cross-section which is then used to weight the DFT calculated PDOS. The photoionisation cross-section weighted PDOS were then summed and convolved with a 0.7 eV FWHM Gaussian to allow for life-time broadening, phonon broadening, and the finite experimental resolution.

## 5.4 Results and Discussion

### 5.4.1 Computational Results

The key numerical results are shown in Table 5.1, which also includes values from recently published hybrid functional (HSE 06) [37], and $GW$ quasiparticle calculations [162]. The calculated lattice parameters agree well with experimental data and previous theoretical calculations [20, 37, 162, 172]. The calculated DFT band structures are shown in Figure 5.4 (a-c), where clear differences between the functionals are visible. Both LDA and PBE predict CdO to be a semi-metal, i.e. the CBM is below the VBM. This is clearly not consistent with the experimental evidence, with the most recent optical measurements placing the direct band gap at 2.18 eV

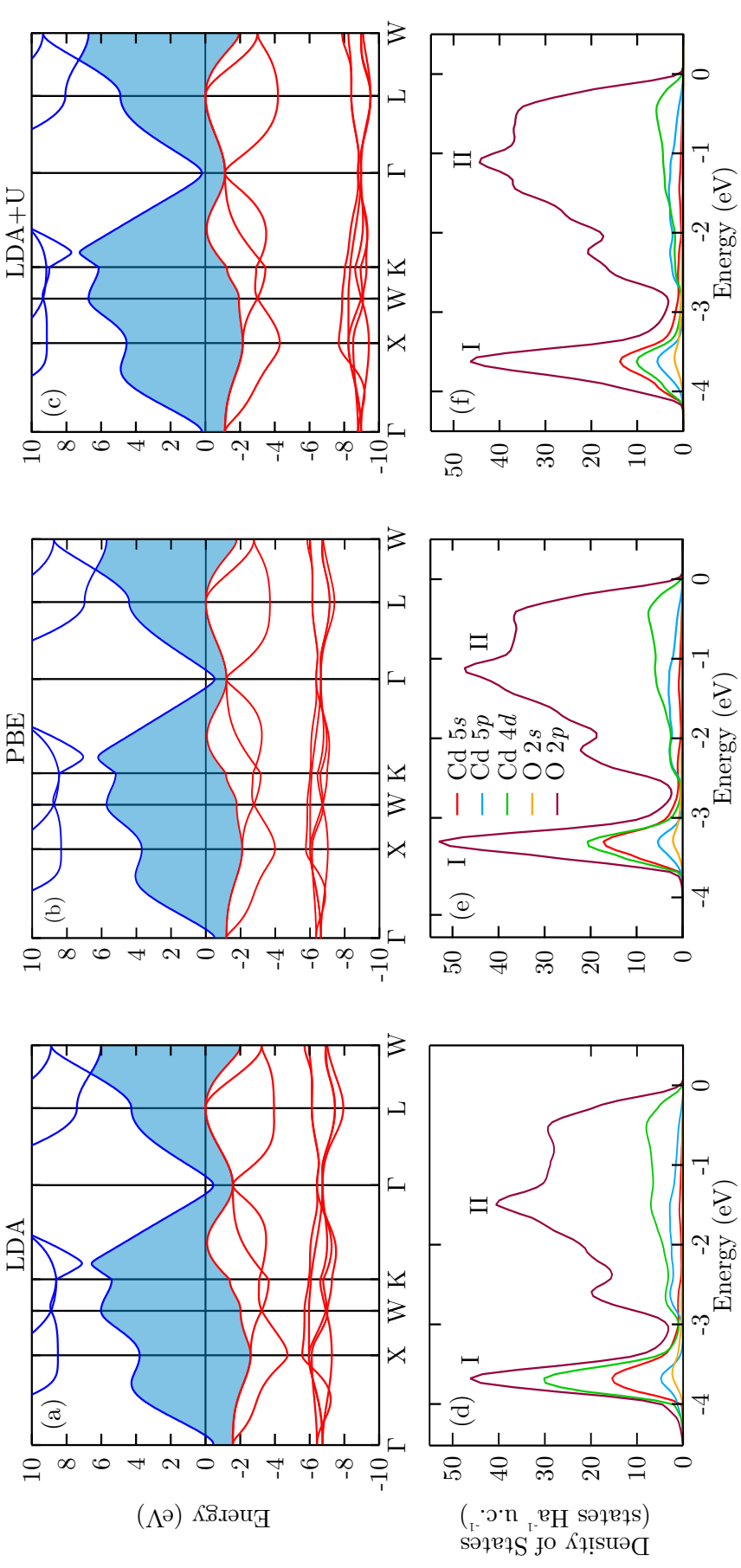


**Figure 5.4.** (a-c) CdO DFT band structures for (a) LDA, (b) PBE, and (c) LDA+$U$. Blue and red lines denote conduction and valence bands respectively, the blue shaded region shows the band gap. Note the overlap of the conduction and valance bands predicted by LDA and PBE indicating a semi-metallic system. Also note the shift in Cd $4d$ states at approximately $-8$ eV produced by LDA+$U$. (d-f) show the DFT PDOS calculated using (a) LDA, (b) PBE, and (c) LDA+$U$. The peak labels I and II derived form experiment refer to the energy ranges -4.5 eV to -3 eV and -3 eV to 0 eV respectively. The energy zero is set to the VBM.

at room temperature [120] and XANES reporting an indirect gap of $\sim 0.9$ eV [36]. PBE predicts the location of the Cd $4d$ states to be very similar to LDA, but with a slightly narrower overall width. LDA+$U$ shifts the Cd $4d$ states down by $\sim 2$ eV and this opens a direct band gap of 1.34 eV. Although semiconducting behaviour, with a non-vanishing indirect gap is now predicted, both the direct and indirect gaps are still too small when compared to experiment. It is worth noting that more sophisticated computational methods such as hybrid functionals [37] can potentially predict the band gap much more accurately.

The PDOS for each of the functionals is shown in Figure 5.4 (d-f). Note that for all of the functionals considered, the VB DOS is dominated by O $2p$ character, and the shape of this feature is very similar. PBE predicts a narrower VB than either LDA or LDA+$U$. The most significant difference is in the orbital character of peak I. LDA predicts this peak to have significant Cd $4d$ character resulting from the underestimation of the Cd $4d$ states binding energy. PBE shows the Cd $4d$ character of this peak to be much reduced giving roughly similar importance to Cd $4d$ and Cd $5s$. For LDA+$U$ the Cd $4d$ character of peak I is further reduced due to the Cd $4d$ states being shifted to lower energy reducing hybridisation. This results in Cd $5s$ contributing more to the DOS in peak I than Cd $4d$. The Cd $5p$ and O $2s$ components are also shown despite often being excluded due to their small contributions. However, at higher photon energies their importance to VB-PES increases as their photoionisation cross-section drops off much less rapidly than O $2p$ as shown in Figures 5.3 and 5.7.

### 5.4.2 DFT compared to HAXPES

A comparison between the three DFT functionals and experimental valence band photoemission spectroscopy (VB-PES) measurements, taken with a photon energy of 6054 eV, is shown in figure 5.5. The higher photon energy compared to earlier studies [114, 115] decreases the degree of surface sensitivity, which is beneficial in the case of CdO as it is known to exhibit surface electron accumulation, [66, 116] which

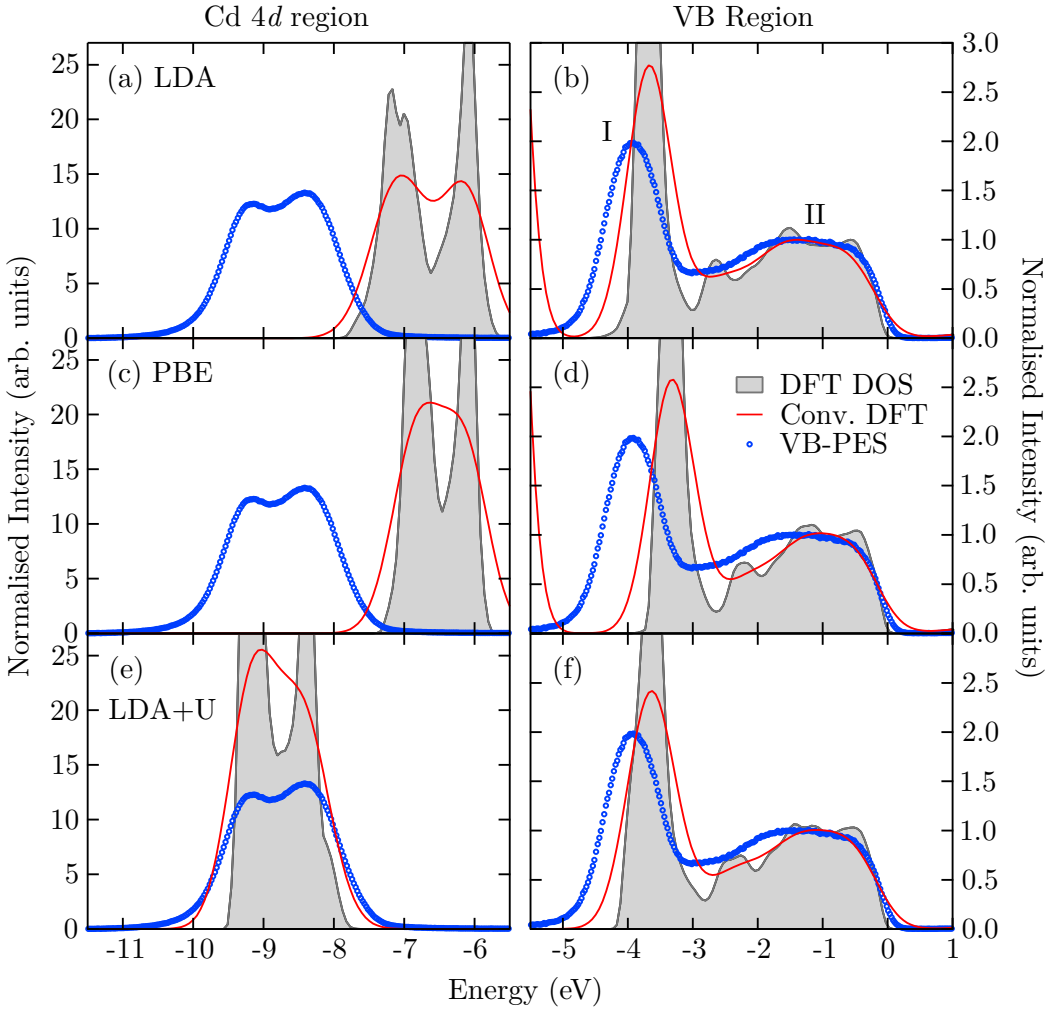


**Figure 5.5.** VB and Cd 4*d* PES spectra compared to DFT, (a) and (b) LDA, (c) and (d) PBE, (e) and (f) LDA+$U$. The DFT PDOS are weighted by the photoionisation cross-sections and summed, shown by the gray shaded areas. The weighted PDOS after convolution with a 0.7 eV FWHM Gaussian are shown by the red line. The experimental data (blue circles) shown is taken with $h\nu = 6054$ eV, and a Shirley background has been subtracted. I and II are peak labels. All energy scales are referenced to the VBM. The experimental spectra and convolved DFT are normalised to the maximum of VB peak II, and the same normalisation has been applied to both the VB and Cd 4*d* regions. Note the different intensity scales.

is not representative of the bulk electronic properties. A Shirley background [77] has been subtracted across the whole region. The PDOS shown in Figure 5.4 (d-f) have been weighted using the photoionisation cross-sections and asymmetry corrections appropriate for a photon energy of 6054 eV and then summed, as shown by the shaded gray region. The sum of weighted PDOS was then convolved with a 0.7 eV FWHM Gaussian, resulting in the red line. The experimental spectra and convolved DFT are normalised to peak II of the VB, and the same normalisation was applied to both the VB and Cd $4d$ panels to allow the relative intensities to be observed.

The Cd $4d$ region in panels (a), (c), and (e) of Figure 5.5 shows experimental data placing the Cd $4d$ state at $\sim -8.70$ eV, in good agreement with previous photoemission measurements [114, 115]. Very significant differences between these functionals can be observed, as discussed previously. LDA and PBE place the Cd $4d$ states at approximately the same energy (-6.3 eV), and this is approximately 2 eV shallower than measured by experiment. LDA+$U$ corrects for this disagreement extremely successfully, placing the Cd $4d$ states in very good agreement with the experimental data. This can also be compared to recent hybrid functional calculations placing the Cd $4d$ states at $-7.4$ eV [37] and to a recent $GW$ quasiparticle calculation which places the Cd $4d$ states at approximately $-9$ eV [162]. However, it is interesting to note that the shape of the Cd $4d$ states is better reproduced by LDA which shows two resolvable peaks as seen in the experiment. Due to the decreased interaction between the Cd $4d$ states and the VB predicted by LDA+$U$, and to a lesser extent PBE, the DOS within the Cd $4d$ states is increased. This results in these functionals overestimating the spectral weight of these states relative to the VB.

The VB region shown in panels (b), (d), and (f) of Figure 5.5 exhibits a two peak structure which is correctly reproduced by all the of DFT functionals. However, it can be seen that all three DFT functionals underestimate the VB width, particularly PBE. This is consistent with previous results [115]. Consequently, VB peak I is placed too shallow by around 0.5 eV when compared to the experimental data. The

shape of peak II is best reproduced by LDA which predicts a slightly wider peak than PBE or LDA+$U$. This is partly due to LDA assigning increased Cd 4$d$ character to VB peak II. This is, offset by the fact that LDA also places the Cd 4$d$ states much too shallow resulting in this effect. The additional Cd 4$d$ character is also responsible for LDA giving VB peak I more spectral weight than observed in the experimental data. The relative intensities of peaks I and II in the VB region is best reproduced by LDA+$U$, which still overestimates peak I intensity.

### 5.4.3 Photon Energy Dependence of the CdO VB

The VB-PES taken with photon energies ranging from 600 eV to 7935 eV is shown in figure 5.6 (a). This approach allows the orbital character of the VB to be identified by exploiting the change in photoionisation cross-sections. The spectra have been normalised to the maximum of VB peak II, following a Shirley background subtraction, to allow relative changes to be observed. The key changes in the VB shape observed experimentally are indicated by the two arrows labeled 1 and 2 in Figure 5.6(a). Arrow 1 shows that peak I of the VB increases in intensity strongly with photon energy relative to peak II. Arrow 2 indicates the region in the centre of the VB which also increases in intensity relative to peak II, and this appears, like a broadening of peak II, with increasing photon energy. Figures 5.6 (b), (c) and (d) show the summed DFT PDOS after weighting with different photoionisation cross-sections as appropriate for each photon energy, and a convolution with a 0.7 eV FWHM Gaussian (as before) to allow direct comparison to the experimental data.

It can be seen qualitatively that all the DFT simulations reproduce the trend of peak I increasing in relative intensity with photon energy, but none of the functionals reproduce this behaviour quantitatively. The experimental data at the lowest photon energy shows peak I weaker than peak II. DFT does not predict any orbitals with lower PDOS in peak I than peak II, indicating the orbital character of the VB predicted by DFT cannot be correct. This result is independent of the photoionisation cross-sections applied. However, it can be seen that by reducing the Cd 4$d$

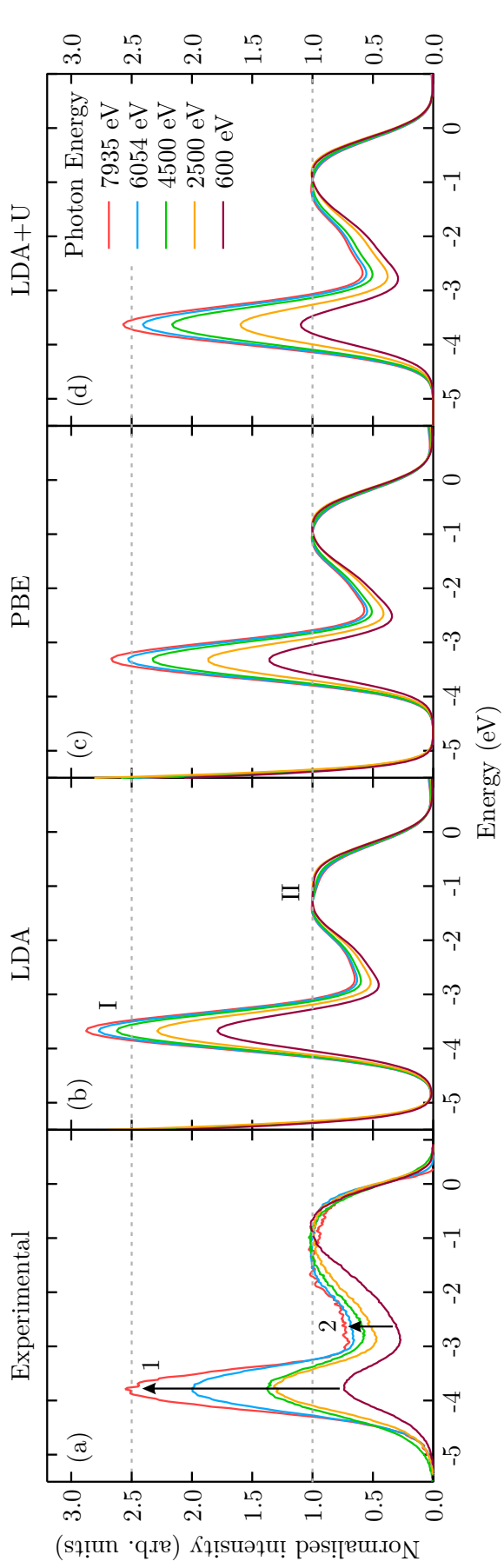


**Figure 5.6.** (a) VB-PES taken with photon energies in the range 600 eV to 7935 eV, a Shirley background has been subtracted. (b-d) Simulations of the VB-PES obtained by applying the photoionisation cross-sections to the DFT approaches. The arrows numbered 1 and 2 in (a) are guides to the eye, discussed in the text. Arrow 1 indicates the increase in intensity of peak I with photon energy, and arrow 2 indicates the enhanced intensity in the centre of the VB with increased photon energy. All spectra have been normalised to the maximum of peak II. The dashed lines are guides to the eye to allow the relative intensities to be observed.

contribution to peak I, which is achieved by LDA+$U$, does significantly improve the experimental agreement. In the experimental data the relative intensity of peak I increases consistently towards the highest photon energy, whereas the simulations predict an initially rapid increase which slows toward the highest photon energy. To address this photon energy dependence, it seems likely that the photoionisation cross-sections may exhibit a more complex energy dependence than encapsulated by the one-electron cross-sections applied here. The rate of decrease of the O $2p$ one-electron cross-section with photon energy appears to be overestimated, as this would result in the more rapid relative increase in peak I intensity with photon energy, as illustrated by the DFT models. Similar conclusions regarding the O $2p$ photoionisation cross-sections being underestimated at higher photon energies were reached in studies of $\beta$-$PbO_2$ [155, 173] and $In_2O_3$, [148] where alternative photoionisation cross-sections calculated by Scofield [95], and by Yeh and Lindau [93] were applied.

One possible explanation is that the very low O $2p$ cross-section at higher photon energies is susceptible to enhancement by interchannel coupling with the much stronger O $2s$ or O $1s$ ionisations. Drube et al. [174] have recently shown that interchannel coupling of this sort may be significant well above threshold. In support of this idea, it should be noted that the agreement between theory and experiment does significantly improve with increasing photon energy. It is also interesting to note that the intensity ratio of peaks I and II is quite well reproduced by all the DFT functionals at the highest photon energy. Here, the VB-PES is dominated by Cd character, whereas at the lowest photon energy Cd and O contribute approximately equally, as shown in Figure 5.7. This suggests that the photoionisation cross-sections are most accurate within an element and may contribute a larger error when comparing orbital character of two or more elements.

The increasing intensity in the centre of the VB with photon energy - shown by arrow 2 at $\sim -2.7$ eV in Figure 5.6 (a) - is most probably a result of Cd $5p$ character in

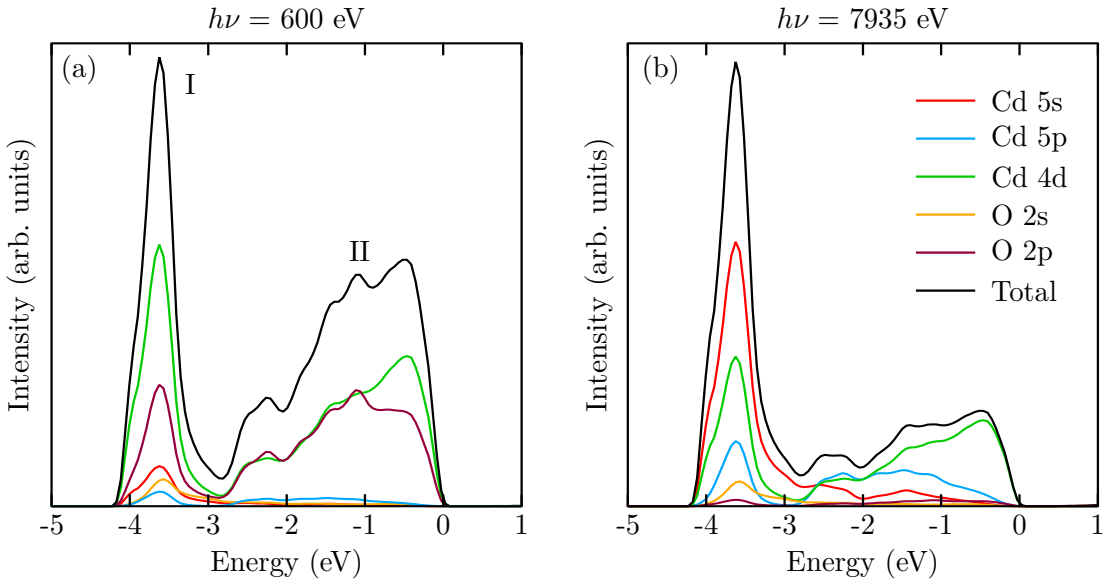


**Figure 5.7.** LDA+$U$ VB PDOS weighted by photoionisation cross-sections for photon energies (a) 600 eV and (b) 7935 eV. It can be seen that at 7935 eV the photoemission is dominated by Cd, whereas at 600 eV Cd and O contribute nearly evenly.

the centre of the VB. The Cd 5$p$ photoionisation cross-section decreases much less rapidly than the O 2$p$ as a function of photon energy, so at the higher photon energies its contribution becomes much more significant (see Figure 5.7). While all the DFT functionals predict some degree of Cd 5$p$ character, it seems likely that this contribution is underestimated, as the experimental data shows a much more significant change. Alternatively, the photoionisation cross-section for Cd 5$p$ could also be underestimated at higher photon energies. While this is possible due to the extrapolation used to obtain the Cd 5$p$ cross-section, it would not be consistent with the trend in peak I which would then show a stronger photon energy dependence if this cross-section was increased.

## 5.5 Conclusions

The VB electronic structure of CdO has been investigated with SR-PES and comparisons to three DFT functionals have been made. The location of the Cd 4$d$ states, which have a significant effect on the theoretical predictions, was not reproduced by either the LDA or PBE-GGA functionals. However LDA+$U$, applied using a

theoretically calculated $U$ value of 2.34 eV, was very successful in predicting the location of these states. Experimentally the VB shows a two peak structure which is correctly reproduced by all the DFT functionals. However, the VB width is underestimated in each case, and the application of LDA+$U$ does not improve this. The photon energy dependence of the VB-PES was measured and compared to the theoretical predictions. All the DFT functionals qualitatively reproduced the observed behaviour, with LDA+$U$ again being the most accurate. The data obtained with the lowest photon energy indicate that the orbital character of the VB was not completely reproduced by the DFT calculations. Additionally the centre of the VB shows a photon energy dependence which was not adequately replicated by any of the DFT functionals. This was assigned to Cd $5p$ character and suggests it is underestimated by the DFT approaches. The trends observed with photon energy indicate the O $2p$ photoionisation cross-sections applied here decrease too quickly with photon energy, in agreement with other studies.

The change in VB shape with photon energy highlights the potential for this kind of approach in understanding the orbital character present in the VB, and by varying the polarisation even more detailed information can be obtained by allowing certain orbital character to be suppressed. In order to exploit this information further, improvements in the photoionisation cross-sections at the high photon energies relevant for HAXPES, or one-step photoemission calculations will be required. All the DFT functionals applied here significantly underestimate the CdO band gap despite their successes in predicting the VB shape and Cd $4d$ position. This clearly illustrates the need for more sophisticated theoretical approaches such as hybrid functionals and $GW$ quasiparticle methods when investigating these materials. It is anticipated that these experimental results will be of use when assessing the successes of these approaches.

# CHAPTER 6

# Control of the CdO Q2DEG and Surface Band Gap

## 6.1 Introduction

In this chapter ARPES, as described in section 2.1.5, is used to probe the quantised 2D electron gas (Q2DEG) states within the surface electron accumulation layer at the CdO(100) surface. The intrinsic surface sensitivity and ability to directly observe the dispersion of subband states makes ARPES an ideal technique to investigate this phenomenon. Q2DEG states form when the downwards bending of the CB is sufficient to quantize the electrons occupying it. There have been two previous ARPES investigations of this phenomena [66, 116]. The first study by Piper et al. [116] confirmed the presence of a Q2DEG and the associated electron density. A more recent study by King et al. [66] found that the electron accumulation layer has a significant effect on the near surface band structure, resulting in surface band gap narrowing. It was proposed that this was due to many-body interactions, specifically electron-electron ($e$-$e$) and electron-phonon ($e$-$p$) interactions in the Q2DEG, effectively renormalising the surface band gap. In turn it might be expected that increasing the electron density in these quantized subbands states would enhance these observed effects.

In the present study, Rb has been deposited on to the CdO surface as a way to introduce extra electrons into the near surface region, and potentially control the 2D electron density. The alkali metals are well known for this electron donation behaviour and have previously been shown to enhance an electron accumulation layer on InAs(110) [175] and induce one on Si(111) [176]. Recently the addition of Rb to the surface of the topological insulator $Bi_2Se_3$ has been shown to induce downwards band bending which can be made robust by intercalation [177]. The addition of alkali metals to graphene has also been used as a way to investigate many-body effects by varying the electron density within this model system [178–180].

A method for accurately obtaining the 2D electron density from the measured Fermi surface is presented and the subband dispersion is extracted. The subband dispersion is simulated using the coupled Poisson-Schrödinger approach described in section 3.2 and fitted to the extracted subband dispersion to allow the conduction band bending (CBB) and subband effective mass to be analysed.

## 6.2 Experimental Details

ARPES data were collected at the SGM-3 beamline of the Astrid synchrotron (Aarhus, Denmark) as described in section 2.1.7. CdO samples, described in section 2.4, were loaded into UHV at the SGM-3 ARPES endstation and prepared by annealing at 600 °C for one hour. This resulted in a sharp $(1 \times 1)$ LEED pattern with low background intensity, indicating a well ordered surface. The highest photon energy available at SGM-3 (130 eV) is insufficient to reach the C $1s$ core level with photoemission, and the Auger spectrometer was not available so the presence of carbon could not be checked. However, as work in the previous chapters of this thesis demonstrate this approach yields a very clean, ordered surface.

The ARPES data presented in this chapter were obtained with a photon energy $h\nu = 30$ eV, an energy chosen based on previous work to maximise the photoemission

intensity of both subband states. The VB and shallow core level spectra were obtained with $h\nu = 32$ eV, thereby maximising the Rb $4p$ core level intensity. The angular resolution was $\sim 0.1^\circ$ which implies a momentum resolution of $\sim 0.025$ Å$^{-1}$, while the overall energy resolution was set to $\sim 30$ meV to allow the experiment to be conducted in a timescale both suitable for Rb in vacuum, and to allow weak spectral features to be resolved. The binding energy scale was referenced to the Fermi edge cutoff visible on the sample. The sample temperature was 70 K throughout all of the ARPES measurements.

The experiments were conducted as follows: the photon energy was set to $h\nu = 30$ eV, an angle scan was taken to obtain a 3D data set from which the Fermi surface was extracted. This angle scan also allows normal emission to be determined. Following the angle scan, the sample was moved to normal emission and a higher statistics scan of the subband dispersion was obtained. The photon energy was then changed to $h\nu = 32$ eV and the VB and shallow core level spectra were obtained. Finally the sample was transferred to the preparation chamber for Rb deposition, and the cycle was repeated.

To deposit Rb the sample was transferred to an uncooled manipulator, resulting in a sample temperature of $\sim 200$ K during deposition. The Rb was deposited using a well-outgassed alkali metal dispenser (SAES Getters) at a working distance of $\sim 15$ mm. The Rb dose was controlled using the exposure time, at a fixed dispenser current of 5.0 A. For the data presented in this chapter the total Rb exposure times were 1, 2, and 4 seconds.

Hall effect measurements of the CdO sample taken following the ARPES experiments revealed a bulk carrier concentration of $n = 2.2 \pm 0.1 \times 10^{19}$ cm$^{-3}$, and mobility of $\mu = 118 \pm 20$ cm$^2$ V$^{-1}$ s$^{-1}$. These values are typical of UHV annealed CdO samples and imply a Fermi level position of 0.1 eV above the CBM, as calculated using $\boldsymbol{k} \cdot \boldsymbol{p}$ carrier statistics, described in section 3.1.3.

## 6.3 Results and Discussion

A 3D schematic of the subband dispersion is shown in figure 6.1 (a) from which two slices have been extracted. The first of these is shown in panels (b-e) and is the Fermi surface as a function of Rb deposition. The Fermi surface plots have been extracted from a 3D ARPES map by integrating the intensity ±10 meV around the Fermi level, which was determined by fitting a Fermi edge to an angle integrated energy distribution curve (EDC). The Fermi surface can be seen to expand as more Rb is added indicating an increased electron density in the Q2DEG, analysed quantitatively in section 6.3.1. The variation in intensity which is observed across the Fermi surface is attributed to changes in experimental alignment while rotating the sample.

The panels (f-i) of figure 6.1 show the dispersion of the two subband states, which appear to shift to larger binding energy as more Rb is added. This effect can be observed more clearly in figure 6.2 where EDCs taken through $k_{||} = 0$ are shown. From the EDC profiles the shift of the two subbands can clearly be observed. The outer subband shifts by $\sim 230$ meV whereas the inner subband shifts by $\sim 100$ meV. At the highest Rb coverage a possible third confined subband is observed, indicated by the peak in the EDC at 0.075 eV, although its BE is very close to that of the bulk CBM. The dispersion of the subband states is discussed further in section 6.3.3 where the dispersion is extracted, and then in section 6.3.4 where the dispersion is simulated and compared to the experiment.

### 6.3.1 Fermi Surface Analysis

The Fermi surfaces shown in figure 6.1 can be analysed in order to obtain information about the 2D electron density as a function of the Rb deposition. The 2D electron density ($N_{2D}$) confined at the surface can be quantified by the Luttinger

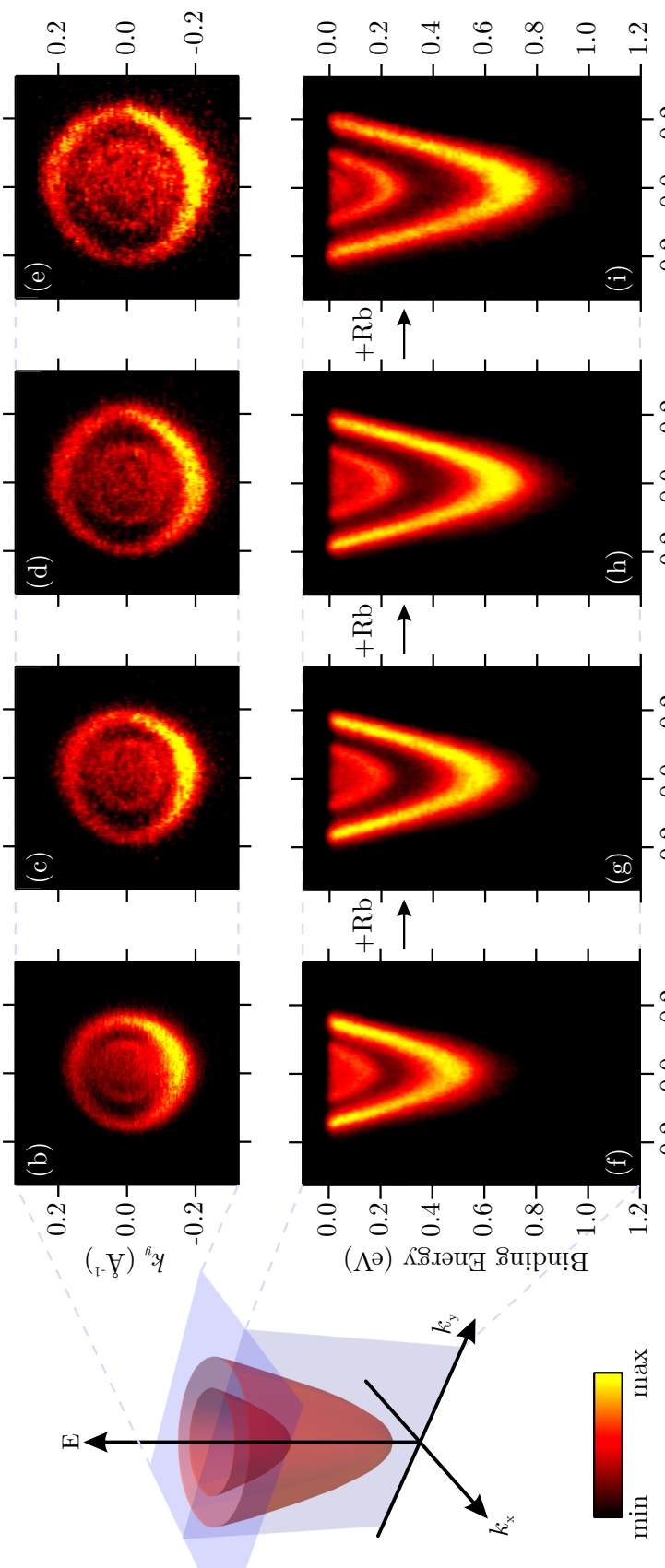


**Figure 6.1.** (a) 3D schematic of the CB quantized subband states. (b-i) ARPES spectra showing photoemission intensity represented by the colour scale indicated. (b-e) Shows the evolution of the Fermi surface as a function of Rb deposition, integrated ±10 meV around the Fermi level. (f-i) shows the evolution of the quantized subbands dispersion as a function of Rb deposition. The Rb deposition times and corresponding $N_{2D}$ displayed are: (b) and (f) 0 sec, $4.71 \times 10^{13}$ cm$^{-2}$; (c) and (g) 1 sec, $6.13 \times 10^{13}$ cm$^{-2}$; (d) and (h) 2 sec, $7.69 \times 10^{13}$ cm$^{-2}$; (e) and (i) 4 sec, $8.80 \times 10^{13}$ cm$^{-2}$. The measurements were performed using $h\nu = 30$ eV, with $k_x$ and $k_{\parallel}$ aligned with the $\overline{\Gamma} \rightarrow \overline{X}$ direction.

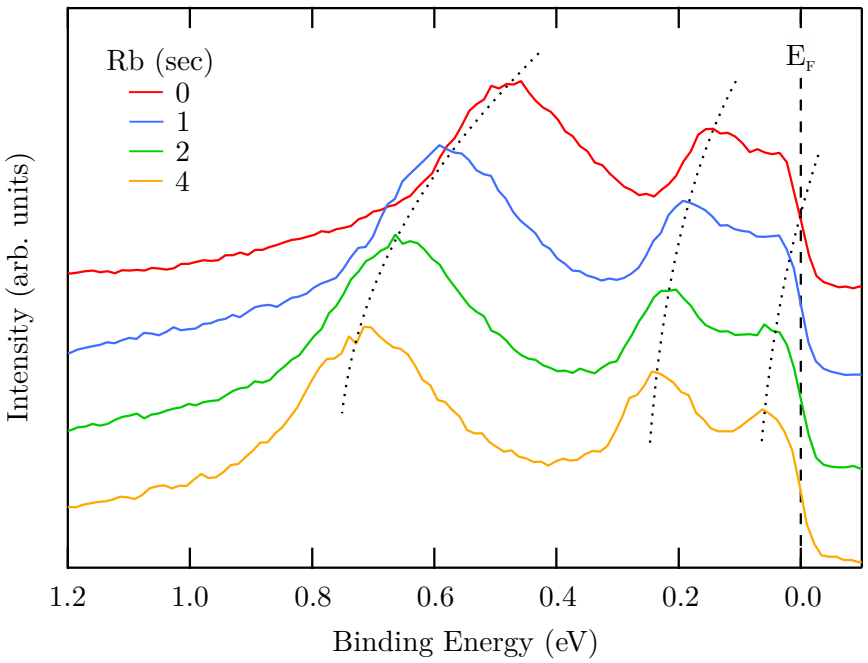


**Figure 6.2.** EDCs taken at $k_{||} = 0$ and integrated 0.01 Å$^{-1}$ from the subband dispersions shown in figure 6.1 (f-i). The spectra are normalised and offset to allow the changes to be observed. The dotted lines are guides to the eye to indicate the location of the subband features including a possible third subband visible in the 4 sec spectra.

equation [181]

$$N_{2D} = \sum_i \frac{k_{Fi}^2}{2\pi}, \tag{6.1}$$

where $i$ is the subband index, and $k_F$ is the wavevector where the subband crosses the Fermi level.

In order to accurately extract the $k_F$ values of the subbands the Fermi surface can be radially integrated, producing a line profile which displays peaks corresponding to the subbands. In order to radially integrate the Fermi surface, 360 line profiles were taken at 1° steps and summed. This results in the radially integrated line profiles shown in figure 6.3 (a). These profiles were fitted with two Voigt peaks in order to accurately extract the $k_F$ position of the subbands. A second order polynomial was used as a background in the peak fitting. There is no physical justification for this choice, however, it allows the peaks to be well fitted and will therefore result in accurate peak positions. The results of these peak fits are shown in figure 6.3 (b-e)

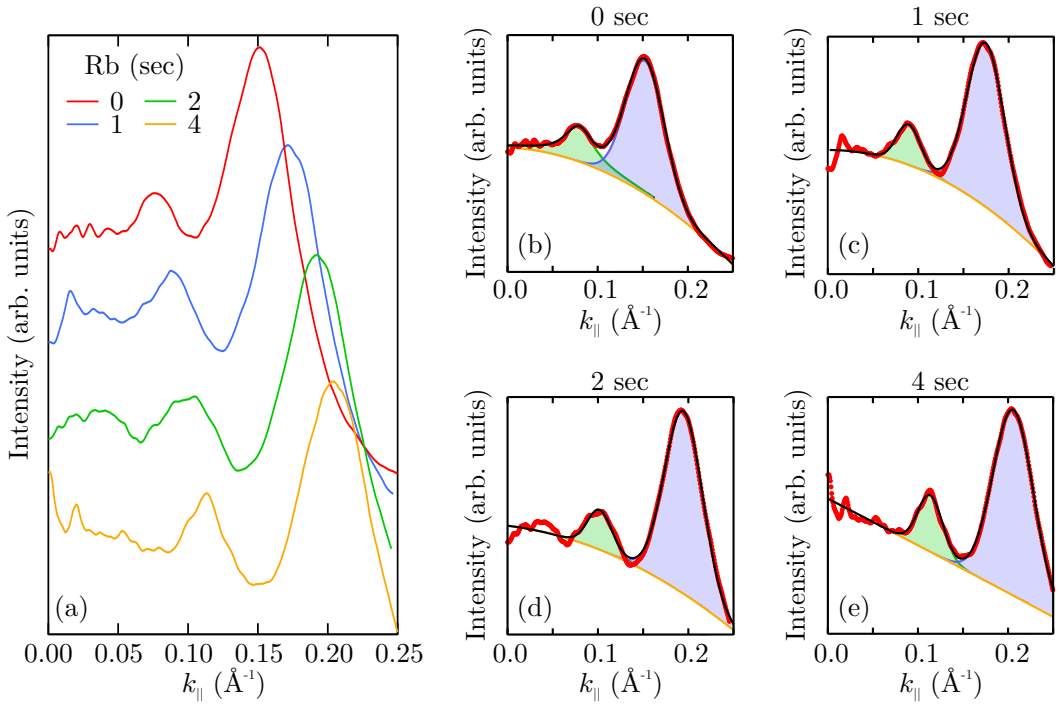


**Figure 6.3.** (a) Radially integrated line profiles of the Fermi surfaces shown in figure 6.1. (b-e) Peak fits to the radially integrated line profiles to extract the positions of the subbands. The red dots are the line profiles for each of the Rb doses, the shaded green and blue peaks are Voigt peaks and the orange and black lines represent a polynomial background and the fitting envelope respectively. The peak positions obtained from the fitting are given in table 6.1.

for each of the Rb doses, and the extracted peak positions are given in table 6.1. Using these extracted peak positions the 2D electron density can be calculated in each case using equation 6.1. The results of this calculation are also shown in table 6.1. These 2D electron densities are used instead of the Rb deposition time for the rest of the discussion.

In order to calculate the total 2D electron density only two subbands have been considered. At the higher Rb doses it is possible that a third subband could be confined, as has been discussed previously and this would add an additional contribution the the total 2D electron density. However, as the third subband would have a relatively small $k_F$, and this term is squared when converting to 2D electron density, its effect would be small. For example a third confined subband with $k_F = 0.05$ Å$^{-1}$ would contribute an additional $\sim 4 \times 10^{12}$ electrons per cm$^2$ to the 2D electron density which is <5 % of the total 2D electron density.

**Table 6.1.** Numerical results from the analysis of the Fermi surfaces obtained for each of the Rb exposure times. The $k_F$ positions are those extracted by the peak fits shown in figure 6.3. The $k_F$ values have an error of $\pm 0.003$ Å$^{-1}$ obtained from the fits. The $N_{2D}$ values are obtained using equation 6.1, and contain an error of $\pm 0.05 \times 10^{13}$ cm$^{-2}$. From the $N_{2D}$ values a monolayer (ML) coverage of Rb has been calculated, discussed in the text.

| | $k_F$ (Å$^{-1}$) | | $N_{2D}$ ($\times 10^{13}$ cm$^{-2}$) | | | |
|---|---|---|---|---|---|---|
| Rb (sec) | Outer | Inner | Outer | Inner | Total | Rb (ML) |
| 0 | 0.153 | 0.079 | 3.70 | 1.01 | 4.71 | 0 |
| 1 | 0.175 | 0.089 | 4.86 | 1.27 | 6.13 | 0.031 |
| 2 | 0.195 | 0.102 | 6.04 | 1.65 | 7.69 | 0.076 |
| 4 | 0.206 | 0.114 | 6.74 | 2.06 | 8.80 | 0.090 |

From the increase in 2D electron density an estimation of the amount of Rb present can be made. If the Rb atoms are assumed to be square packed on the surface, with an atomic radius of 2.35 Å [52], then a density of $4.53 \times 10^{14}$ Rb atoms per cm$^2$ can be calculated. If each Rb atom on the surface is assumed to donate one electron into the Q2DEG, then the monolayer (ML) coverage of Rb required to donate the observed electrons can be calculated. The results of this calculation are shown in table 6.1, where it can be seen that the amount of electronically active Rb on the surface is less than 10 % of a ML for the highest Rb dose.

### 6.3.2 Valence Band and Shallow Core Levels

Angle integrated VB and shallow core level spectra as a function of Rb deposition were also recorded and are shown in figure 6.4. The spectra are integrated over an angular range of $\pm 7°$. The Rb $4p$ peak at $\sim 14.7$ eV is observed to increase as more Rb is deposited, indicating that an increased amount of Rb is present on the CdO surface. By taking the areas of the Rb $4p$ and Cd $4d$ and applying the photoionisation cross-sections an estimate of the Rb coverage can be obtained. Applying this approach here results in Rb coverages of 0.04, 0.29 and 0.89 of a ML for the 1, 2 and 4 second Rb exposure respectively. While there is good agreement between this approach and the electronic estimation made in the previous section for the 1 second

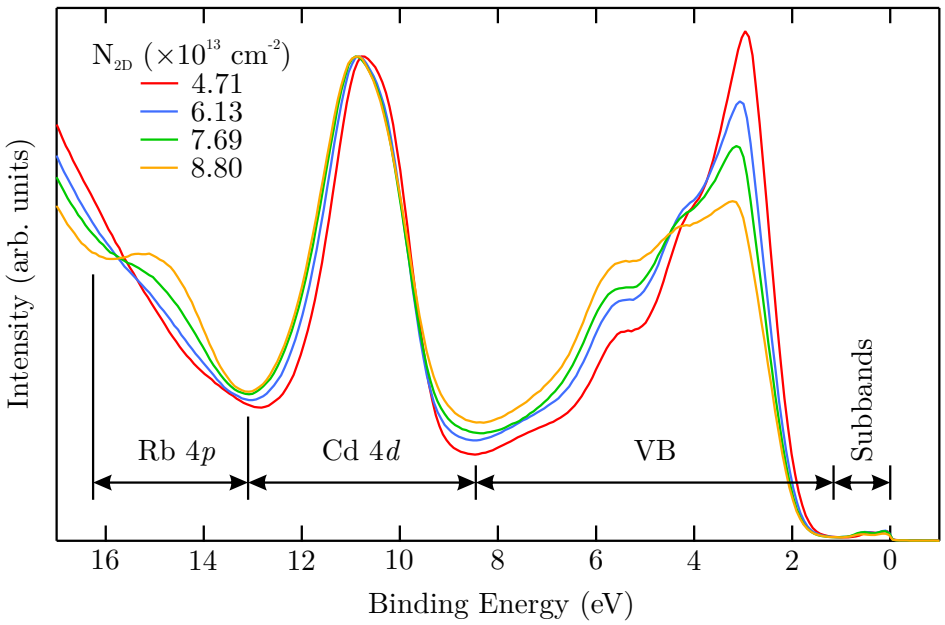


**Figure 6.4.** Angle integrated VB and shallow core level spectra, taken with $h\nu = 32$ eV, as a function of the Rb deposition, parameterised by 2D electron density. The key spectra regions are indicated for clarity. The spectra are normalised to the Cd $4d$ peak at $\sim$ 10.7 eV. The Rb $4p$ peak at $\sim$ 14.7 eV is seen to appear and increase with Rb dose. The subbands can also be seen just below the Fermi level giving an indication of intensity relative to the VB.

exposure there is significant differences for the 2 and 4 second exposures. This may indicate an oxidation of the Rb as the experiment progressed. However these values will contain significant errors due to the difficulty in defining the background and therefore area of the peaks and the uncertainty of the photoionisation cross-sections when applied at very low photon energies.

The Cd $4d$ peak at $\sim$ 10.7 eV is seen to shift to slightly higher binding energy as more Rb is deposited, and this is attributed to increased downwards valence band bending (VBB). The conventional measure of VBB is to extrapolate the leading edge of the VB to obtain a value for the VBM to Fermi level separation at the surface [143], as used previously in this thesis. This approach is, however, complicated for two reasons. The first is that the low photon energy employed does not ensure that the whole BZ is sampled, therefore as the CdO VBM is away from the $\Gamma$ point , this would lead to an overestimation of the value obtained for the VBM position. Secondly the leading edge of the VB changes shape significantly as Rb is deposited

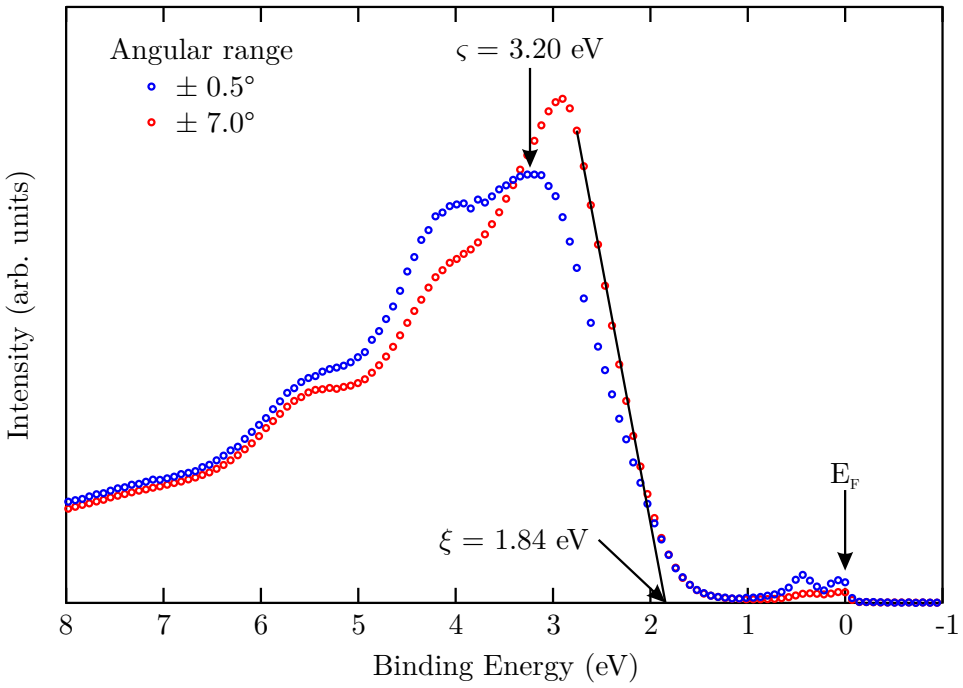


**Figure 6.5.** Angle integrated VB spectra taken with $h\nu = 32$ eV, for two ranges of angular integration ±7° and ±0.5°. From the wider angular range the VB edge has been extrapolated to obtain the surface VBM to Fermi level separation. On the narrow range of angular integration at Γ the position of the first subband peak is indicated.

making it difficult to take consistent extrapolations. This latter difficulty in the VB edge extrapolation can be circumvented by using an alternative measure of the change in the VBB. In this case the Cd $4d$ peak position is used as the measure of the change in VBB. Fitting of this peak is difficult as it hybridises strongly with the VB and so the line shape is not well reproduced by a conventional spin-split doublet as would be expected for the Cd $4d$ peak [66]. The position was therefore extracted by fitting a single Lorentzian to the top of the peak, the resulting peak positions are given in table 6.2. The extracted position moves from 10.50 eV to 10.79 eV, implying the VBB increases by $\sim$ 0.3 eV over the range of 2D electron densities investigated.

Knowledge of the VBB of the clean surface is also required to obtain an absolute value for the VBB. In order to extract the VBB of the clean surface, three approaches have been investigated. Figure 6.5 shows two VB spectra obtained using different angular ranges. The wide angle (±7°) attempts to collect electrons over the full

BZ allowing the VB edge to be extrapolated and obtain the VBM to Fermi level separation at the surface. From this the indirect band gap and Fermi level can be subtracted to obtain the downwards VBB potential ($V_{VBB}$)

$$V_{VBB} = \xi - E_{G\ indirect} - E_F. \tag{6.2}$$

From the VB edge extrapolation $\xi = 1.84$ eV, DFT calculations [37] predict $E_{G\ indirect} = 0.89$ eV, and from Hall measurements $E_F = 0.1$ eV, therefore $V_{VBB} = 0.85^{+0.05}_{-0.40}$ eV. The large error on the lower bound is because the low photon energy does not ensure that the full BZ is sampled, and therefore the VBB will be over estimated.

The second approach uses a small angular range ($\pm 0.5°$) at normal emission ($\Gamma$), and from this spectra the position of the first VB peak ($\varsigma$) should correspond to the VBM at $\Gamma$. From this the direct band gap and Fermi level can be subtracted to obtain the VBB.

$$V_{VBB} = \varsigma - E_{G\ direct} - E_F. \tag{6.3}$$

In this case $\varsigma = 3.20$ eV, and $E_G = 2.2$ eV [38], and therefore $V_{VBB} = 0.9 \pm 0.4$ eV. The error here is due to both the difficulty in accurately obtaining the peak position, and $k_z$ broadening which prevents the $\Gamma$ point being exclusively probed. Finally the position of the Cd $4d$ peak on the clean sample can be compared with previous measurements. In chapter 5 the Cd $4d$ position was found to be $\sim 8.7$ eV below the VBM. Subtracting this value from the position of the Cd $4d$ peak measured from the clean surface (10.50 eV), results in a measure of the VBM ($\xi$), and therefore subtracting the indirect gap and Fermi level results in a measure of VBB via

$$V_{VBB} = (\text{Cd } 4d) - (\text{Cd } 4d - \text{VBM})_{reference} - E_{G\ indirect} - E_F. \tag{6.4}$$

The value of VBB obtained from this approach is $0.81 \pm 0.15$ eV, where the main source of error is in the approach used to obtain the Cd $4d$ peak position.

**Table 6.2.** Numerical results from analysis of the VB and shallow core levels obtained for each of the Rb exposures, parameterised by the 2D electron density. The Cd $4d$ location and shift are given along with the corresponding VBB ($V_{VBB}$). The error in the extracted the peak position is estimated as $\pm 0.05$ eV.

| $N_{2D}$ ($\times 10^{13}$ cm$^{-2}$) | Cd $4d$ (eV) | $\Delta$ Cd $4d$ (eV) | $V_{VBB}$ (eV) |
|---|---|---|---|
| 4.71 | 10.50 | 0 | 0.81 |
| 6.13 | 10.73 | 0.23 | 1.04 |
| 7.69 | 10.77 | 0.27 | 1.08 |
| 8.80 | 10.79 | 0.29 | 1.10 |

While the values obtained from the different approaches are in good agreement, they have relatively large errors due to difficulties with the methods. This highlights the advantages of higher photon energies for determining band bending values accurately, although this still requires accurate knowledge of the indirect gap. For the following discussion the VBB value of the clean surface will be taken as $V_{VBB} = 0.81$ eV as this is the value with the smallest uncertainty. This value is relatively high in comparison to previous measurements ($\sim 0.25$ eV), although the difficulty in accurately obtaining this value were also noted in that study [66]. The exact value used for the clean surface VBB would result in an offset in the surface band gap but would not alter any trends discussed later.

### 6.3.3 Extracting the Subband Dispersion.

In order to perform qualitative analysis of the subbands, the subband dispersion needs to be extracted from the ARPES spectra. This was achieved using a combination of MDC and EDC fitting. Figure 6.6 (a) shows the subband dispersion ARPES spectra with red and blue lines to indicate the location of example MDC and EDC profiles respectively. These example profiles are shown in figure 6.6 (b) and (c), where the intensity present due to the subbands can be observed as peaks. In order to extract the location of the subbands from these profiles, a Lorentzian peak was fitted with a linear background to a region of the profile, and this was repeated successively moving along the band. The peak positions extracted using

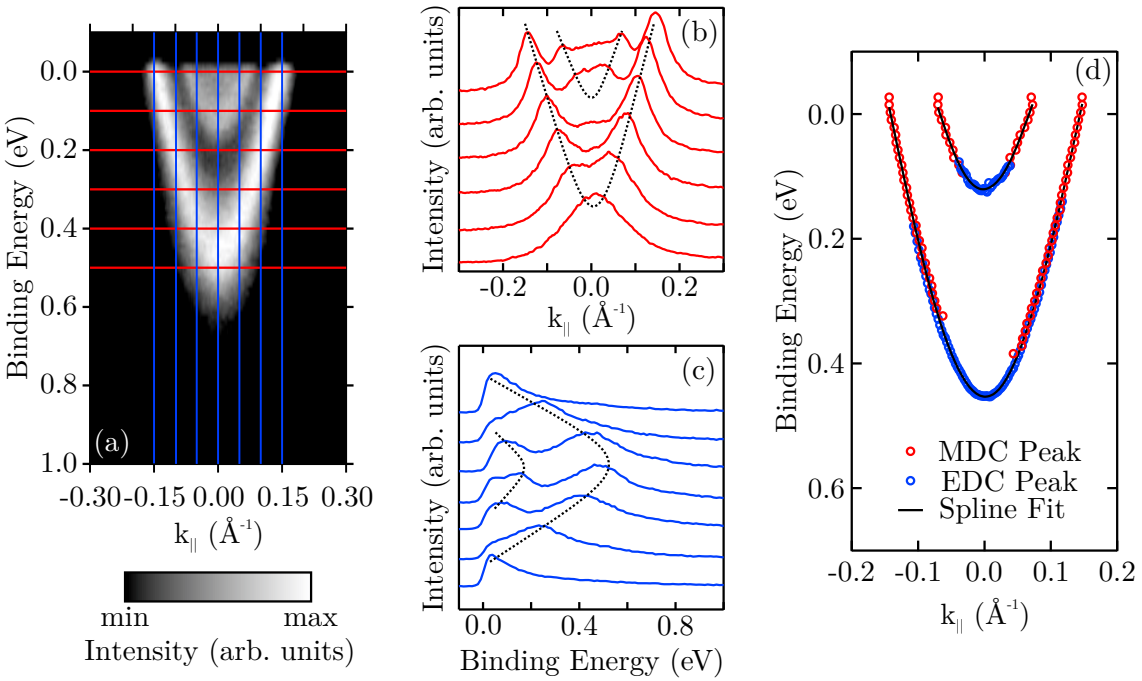


**Figure 6.6.** Extraction of the subband dispersion. (a) Clean subband dispersion (as in figure 6.1 (f)) red and blue lines indicate the positions of momentum distribution curve (MDC) and EDC profiles respectively, the intensity colour scale is also shown. (b) MDCs from positions indicated in (a) integrated ±5 meV. (c) EDCs from positions indicated in (a) integrated ±0.005 $Å^{-1}$. The dotted lines in (b) and (c) are guides to the eye to allow the subband dispersion to be observed. (d) Peak positions obtained from fits to the MDC and EDC shown as open circles and a spline fitted through the points to extract the final dispersion.

this procedure are displayed by the red and blue open circles for MDC and EDC respectively in figure 6.6 (d). The stability of the fitting is best when the peak is sharply defined, which occurs on the sides of the subband when using MDCs and near the bottom of the subband when using EDCs. It is for this reason that applying both allows the dispersion to be accurately extracted over the whole subband. Once the MDC and EDC peak positions have been extracted a single spline was fitted through each subband to obtain the final dispersion. The final extracted dispersions are shown in figure 6.7 (a-d) overlayed on the ARPES spectra to allow the agreement to be observed. In figure 6.7 (e) the extracted dispersion for each of the 2D electron densities are plotted together to allow the effect of increasing the 2D electron density to be observed. From the extracted dispersions the outer subband can be seen to shift to higher BE by $230 \pm 5$ meV whereas the inner subband shifts

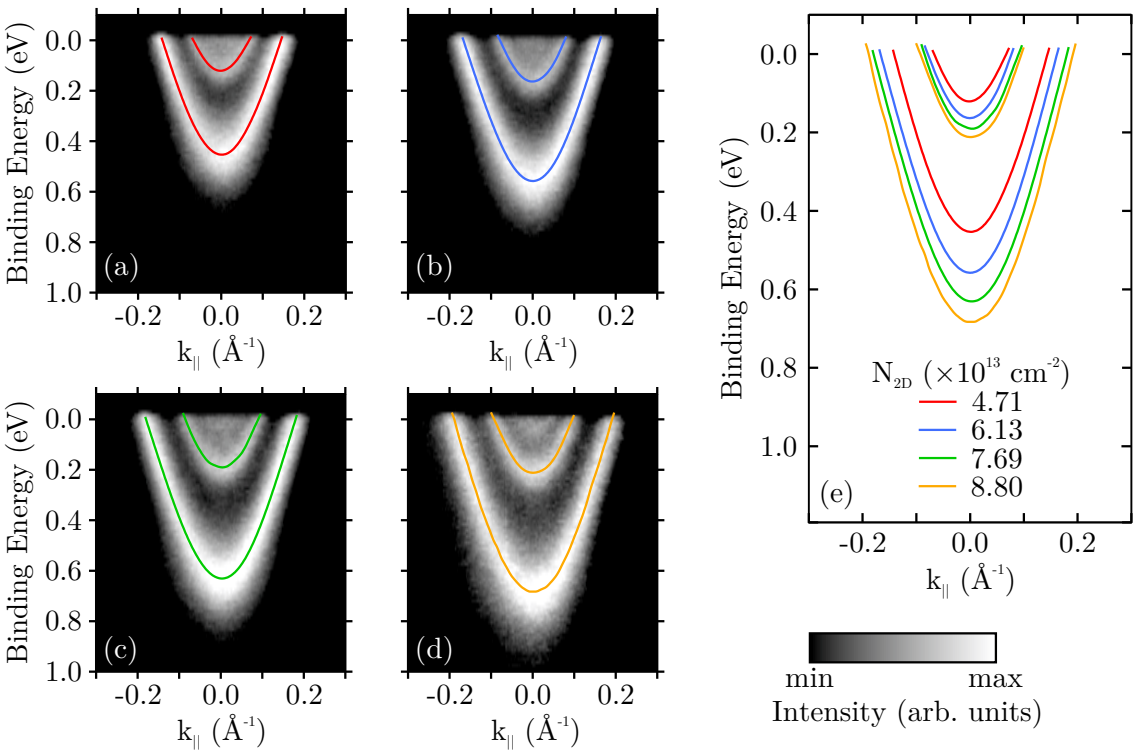


**Figure 6.7.** (a-d) Subband ARPES spectra (as in figure 6.1 (f-i)) with the extracted dispersions overlayed. The colour scale representing photoemission intensity is also shown. (e) Comparison of the extracted subband dispersions for each of the 2D electron densities.

by $91 \pm 5$ meV with the highest Rb coverage.

### 6.3.4 Simulation of the Subband Dispersion

Extracting the subband dispersion allows it to be quantitatively analysed. Using the coupled Poisson-Schrödinger approach described in section 3.2, the subband dispersion was simulated and then compared to the experimental data. The free parameters in the model are the conduction band bending (CBB), and material properties including: the direct band gap ($E_G$), the CB effective mass ($m^*$), the bulk carrier concentration ($n$) and the static dielectric constant ($\epsilon_0$). The values used for these material parameters are taken from previously published results and are: $E_G = 2.20$ eV, $m^* = 0.24m_e$ [38, 120] and $\epsilon_0 = 18$ [159]. The bulk carrier concentration was taken from Hall effect measurements made on the samples following the ARPES measurements, giving $n = 2.2 \times 10^{19}$ cm$^{-2}$. Only the outer subband was considered when performing the fitting as its dispersion can be extracted more

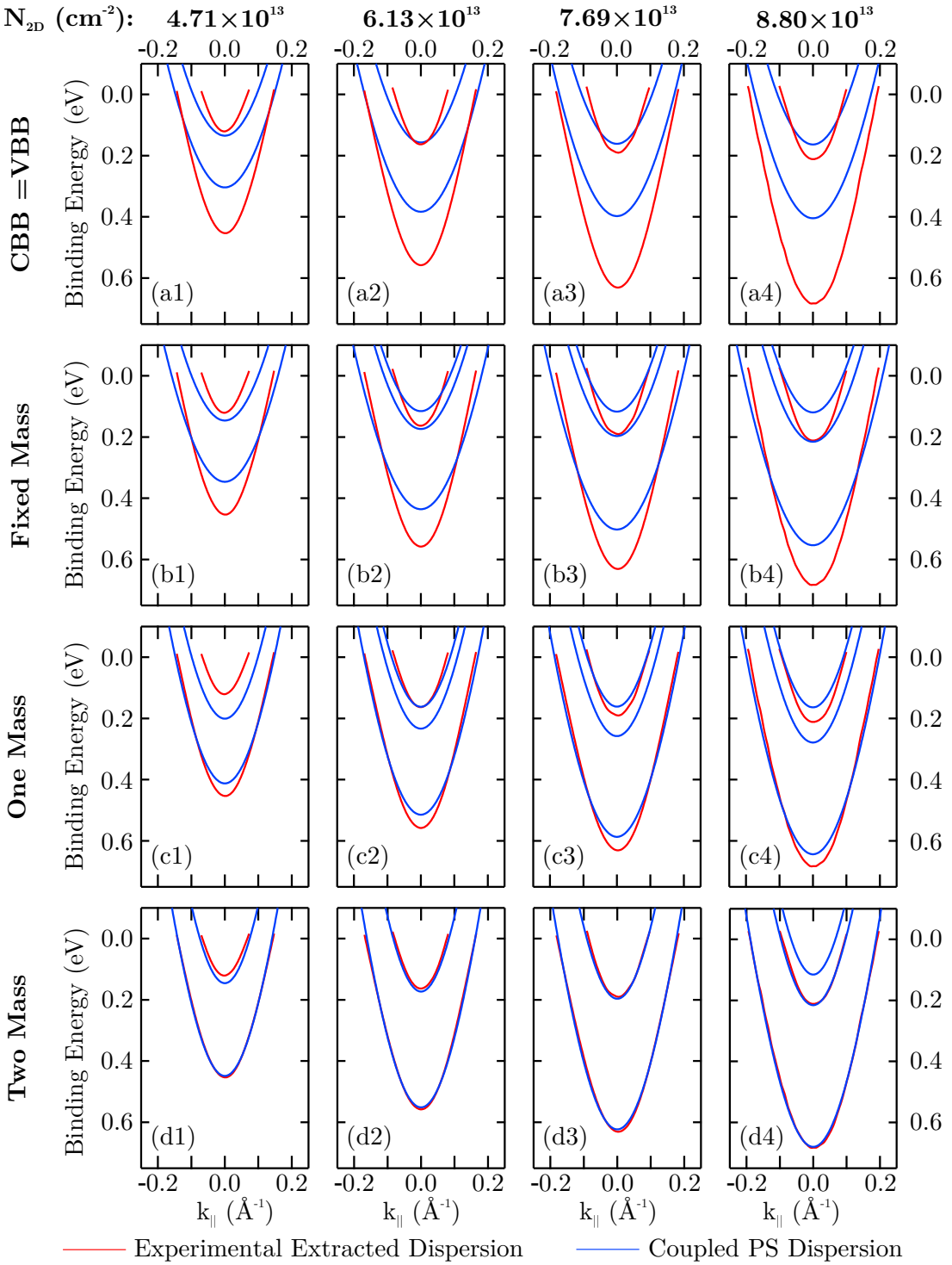


**Figure 6.8.** Results of fitting the coupled Poisson-Schrödinger model to the extracted subband dispersions. The experimentally extracted dispersions are shown in red for each of the 2D electron densities, and the simulated subband dispersions are shown in blue. Four approaches to the fitting are shown as described in the text, with the numerical results given in table 6.3. Rows: (a) CBB=VBB, (b) $m^* = 0.24m_e$, (c) $m^*$ is a fitting parameter, (d) the subband effective mass is allowed to vary, while the bulk mass is set at $m^* = 0.24m_e$. Columns: (1) $N_{2D} = 4.71 \times 10^{13}$ cm$^{-2}$, (2) $N_{2D} = 6.13 \times 10^{13}$ cm$^{-2}$, (3) $N_{2D} = 7.69 \times 10^{13}$ cm$^{-2}$, (4) $N_{2D} = 8.80 \times 10^{13}$ cm$^{-2}$.

**Table 6.3.** Numerical results obtained from fitting of subband dispersions using the coupled Poisson-Schrödinger approach. For the fitting approaches shown in figure 6.8 and discussed in the text.

| | Fixed Mass | One mass | | Two mass | |
|---|---|---|---|---|---|
| $N_{2D}$ ($\times 10^{13}$ cm$^{-2}$) | $V_{CBB}$ | $V_{CBB}$ | $m^*/m_e$ | $V_{CBB}$ | $m^*_{subband}/m_e$ |
| 4.71 | 1.03 | 0.96 | 0.136 | 1.59 | 0.129 |
| 6.13 | 1.29 | 1.25 | 0.139 | 1.91 | 0.132 |
| 7.69 | 1.47 | 1.45 | 0.143 | 2.11 | 0.137 |
| 8.80 | 1.61 | 1.60 | 0.146 | 2.27 | 0.139 |

reliably, which additionally allows the position and dispersion of the inner subband to be used as an independent measure when assessing the accuracy of the model.

Four different approaches (named: CBB=VBB, fixed mass, one mass, and two mass) have been applied when simulating the subband dispersion. Initially, the most simple approach is to assume that the CBB is equal to the VBB obtained from the VB and shallow core level analysis in section 6.3.2. This approach is referred to as "CBB=VBB", where no fitting is performed in this approach and the results are shown in figure 6.8 (a1-a4). It can be observed that the binding energy position of the outer subband is significantly underestimated with respect to the measured dispersion. This discrepancy increases as the 2D electron density rises, as the VBB does not increase significantly with the addition of Rb. This model indicates that the CBB is significantly underestimated by assuming it is equal to the VBB.

The second approach is to allow the CBB to be a free parameter and perform fitting, a method referred to as "fixed mass" (as the effective mass is constant at the bulk value $m^* = 0.24m_e$). The results of this approach are shown in figure 6.8 (b1-b4) and in table 6.3. Several aspects of this fit deserve comment, firstly the position of the bottom of the band is still not well reproduced for the outer subband, despite this being fitted. This is due to the poor agreement of the simulated and measured dispersion, with the measured dispersion appearing to have a much lighter effective mass. Despite this failure, the inner subband position is reproduced quite well,

especially at the higher 2D electron densities, however it also appears to have a lower effective mass than predicted by the simulation.

The third fitting approach is to allow the CBB and the effective mass to be treated as fitting parameters, this approach is referred to as "one mass". The results of this approach are shown in figure 6.8 (c1-c4) and in table 6.3. The results obtained using this approach indicate that the effective mass required to fit the subbands is much lower than the reported bulk mass. An effective mass in the range $0.136m_e$ to $0.146m_e$ was found, and this value is approximately half that of the bulk mass. It is also interesting to note that despite this large discrepancy in the effective mass, the values of CBB obtained from this approach are in broad agreement with those obtained using the fixed mass approach.

The final approach is to use the bulk mass of $m^* = 0.24m_e$ when solving the Poisson equation for the band bending profile (i.e. the shape of the potential well), and then use a second mass when solving the Schrödinger equation to obtain the subband dispersion, in effect allowing a different subband mass ($m^*_{subband}$). This additional subband mass is used as a fitting parameter along with the CBB, this approach is referred to as "two mass". The intriguing results of this approach are shown in figure 6.8 (d1-d4) and in table 6.3. Firstly, the calculated subband dispersions provide an excellent match to the experimental data, for both the outer subband, which was used in the fitting, but also the position and dispersion of the inner subband (which was not included in the fitting). In addition, only two subbands are predicted for the lowest three 2D electron densities and three at the highest density, in agreement with the extra observed peak in the subband EDCs, shown in figure 6.2. The values obtained for the CBB using this approach are significantly larger than the other approaches, with a CBB value of 2.27 eV obtained for the highest 2D electron density. However, the values obtained for the subband effective mass are in close agreement with those obtained by the one mass approach.

The results obtained from all four of these fitting approaches are summarised in

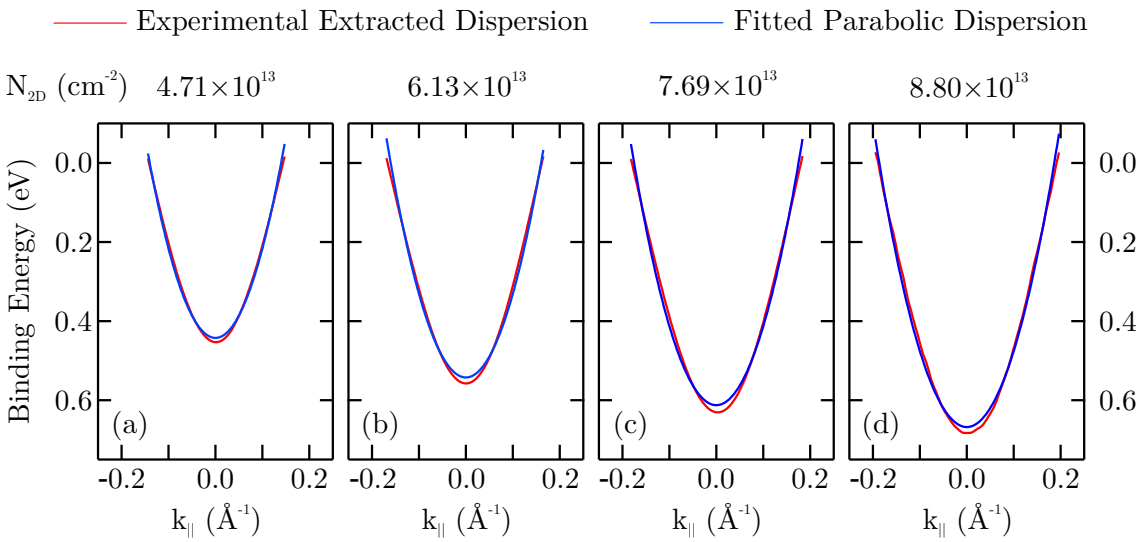


**Figure 6.9.** Outer subband dispersion and parabolic fits to extract the effective mass for each of the 2D electron densities. The obtained effective masses are given in table 6.4.

table 6.3. Two key results can be extracted, the first is that the subband effective mass appears to be significantly reduced when compared to the bulk effective mass. This result is supported by all of the approaches and when the effective mass is fixed at the bulk mass of $0.24m_e$ the dispersions obtained for the subbands are too heavy. When the effective mass is allowed to vary as a fitting parameter, in both the one and two mass approaches, the result is a much lighter effective mass than in the bulk, and both of these approaches obtain similar subband effective masses values. The second key result is that the CBB increases significantly more than the VBB with increasing electron density, resulting in increased surface band gap narrowing. These two results are discussed separately, and in more detail, in the following sections.

#### 6.3.4.1 Subband Effective Mass

The results obtained above indicate that the subbands have an effective mass significantly lower than the bulk CB effective mass. This result has been obtained using the coupled Poisson-Schrödinger model. The most simple approach to obtain the effective mass of a band is via a parabolic fit directly to the dispersion. This allows the effective mass to be obtained without requiring any prior knowledge of

**Table 6.4.** Numerical results of the subband effective masses, extracted by the three fitting approaches, discussed in the text, parameterised by the 2D electron density. The errors on the masses are estimated as ±0.005 from the fitting.

| | $m^*_{subband}/m_e$ | | |
|---|---|---|---|
| $N_{2D}$ ($\times 10^{13}$ cm$^{-2}$) | Parabolic | One Mass | Two Mass |
| 4.71 | 0.168 | 0.136 | 0.129 |
| 6.13 | 0.180 | 0.139 | 0.132 |
| 7.69 | 0.190 | 0.143 | 0.137 |
| 8.80 | 0.197 | 0.146 | 0.139 |

the material parameters. The parabolic dispersion given by equation 3.9 was used to fit the extracted outer subband dispersion, with $E_C(0)$ and $m^*$ treated as free parameters. The results of parabolic fitting are shown in figure 6.9, with the numerical values given in table 6.4. The effective mass values obtained range from 0.168 to 0.197, and confirm a lower mass than in the bulk. However, this mass is not as low as that obtained by the coupled Poisson-Schrödinger approach. This discrepancy is assigned to non-parabolicity which can be observed by comparison of the extracted dispersions and the parabolic fits. This prevents the parabolic model from accurately following the subband dispersion and indicates that accounting for non-parabolicity is crucial when analysing this system.

The agreement between the measured and calculated dispersions obtained using the two mass approach, combined with the low masses obtained from the one mass and parabolic analysis, suggests that there is a lower effective mass present in the Q2DEG than in the bulk. The measured bulk value of $0.24m_e$ used here was obtained from optical measurements of CdO samples over a range of carrier concentrations [38]. This result followed from an earlier optical study where a bulk mass of $0.21m_e$ had been reported [39]. Most recently, temperature dependent optical and transport measurements have been performed on CdO samples, confirming an effective mass of $0.238m_e$ at room temperature which increases to $0.266m_e$ at 0 K [120]. This value of $\sim 0.24m_e$ for the bulk CB effective mass is also supported by various recent DFT calculations including references [37, 162, 163]. Comparing the experimental results

presented here with the body of experimental and theoretical work strongly suggests there maybe a difference between the bulk and subband/surface effective masses. A previous surface study using electron energy loss spectroscopy (EELS) reported an effective mass of $0.13m_e$ for undoped CdO [114] which is in close agreement with the values obtained here from the Poisson-Schrödinger fitting. It is also interesting to note that several other studies of polycrystalline CdO films have reported CB effective masses close to $0.13m_e$ including references [15, 182, 183]. This apparent discrepancy between the surface measurements (ARPES and EELS), and the bulk measurements (optical) and DFT, combined with the success of the two mass fitting approach, are taken as evidence to suggest the surface Q2DEG has a significantly lower effective mass than the bulk. The low masses reported in polycrystalline samples suggest the transport properties here may also be dominated by "surface" conduction within the Q2DEG.

Similar results have been observed at the $SrTiO_3(001)$ surface, where a Q2DEG was created by UV exposure and investigated by ARPES [184]. Here quantised subbands were also observed to possess an effective mass around half that of the lightest bulk effective mass. It was speculated that this could be related to the shrinkage of the band gap at the surface, which has the counter-intuitive effect of lowering the effective mass. Additionally a recent study of $In_2O_3$ similarly reported a lower subband effective mass than observed in the bulk [185]. These other results suggest this effect may not be unique to CdO but a property of oxide semiconductors.

Finally figure 6.10 shows a trend of increasing subband effective mass with 2D electron density ($N_{2D}$). The change in effective mass is, however, quite small over the range of 2D electron densities investigated here, and it is therefore difficult to draw any strong conclusions from this. As many-body interactions are increased, this could lead to an enhancement of the effective mass. However, this trend could also result from increased surface disorder induced by the Rb deposition.

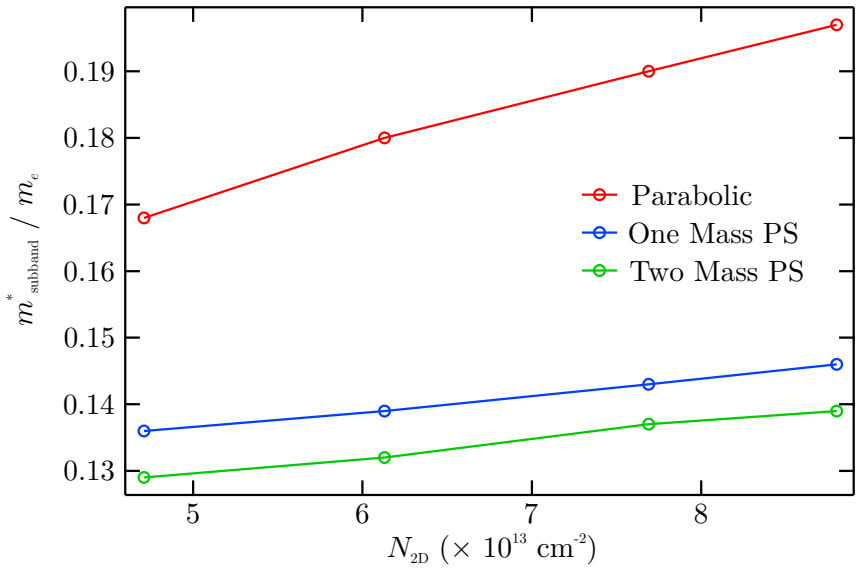


**Figure 6.10.** Subband effective masses extracted using both parabolic and Poisson-Schrodinger fitting as a function of 2D electron density. All approaches show an approximately linear increase in effective mass with $N_{2D}$.

### 6.3.5 Surface Band Gap Narrowing

In the previous sections, independent measurements of the valence band bending (VBB) and conduction band bending (CBB) have been made. With this knowledge, the surface band gap can be calculated and therefore be compared with the bulk band gap. In section 6.3.2 the Cd 4*d* core level shift was used as a measure of the change in the VBB. Several approaches were explored to obtain the initial VBB of the clean surface, and comparison of these methods resulted in a value of 0.81 eV being taken as the initial VBB. The CBB must be obtained by analysis of the measured Q2DEG states. Two of the approaches, the fixed mass and one mass approaches, resulted in very similar values of the CBB. Therefore the fixed mass approach was taken to represent these two approaches and is compared with the two mass approach. A summary of the VBB, CBB and surface band gaps is given in table 6.5.

Using the values of the CB and VB bending obtained above, the band bending profiles can be calculated for each of the 2D electron densities. The results of these calculations are shown in figure 6.11. For both the fixed mass and two mass

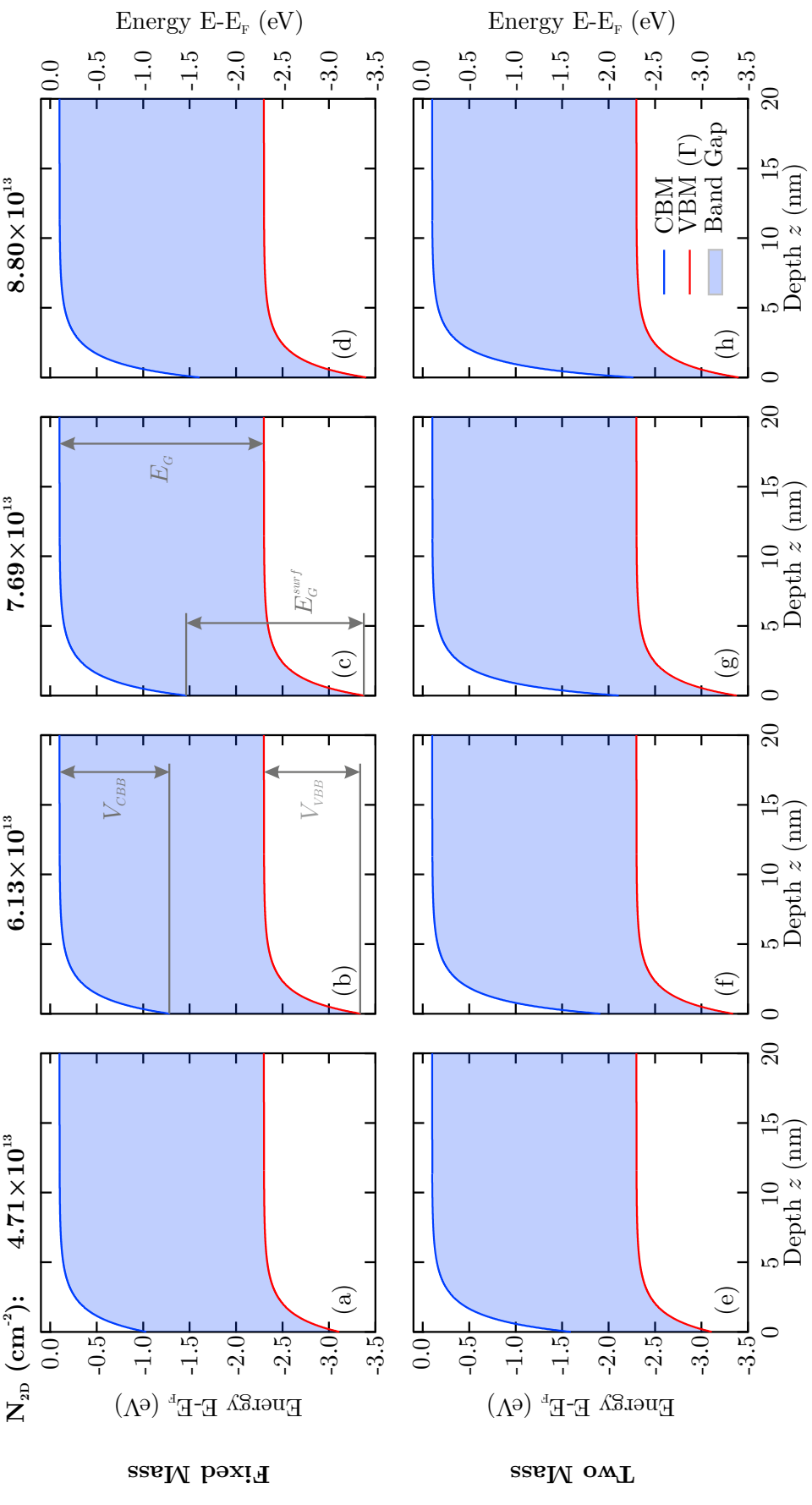


**Figure 6.11.** CB and VB band bending profiles for all the 2D electron densities calculated using the band bending values obtained from analysis of the VB and shallow core levels, and from the simulation of the measured subband dispersion. Two of the approaches applied to simulation of the subband dispersion are shown; the fixed mass approach (a-d) and the two mass approach (e-h). The CBB and VBB are indicated in panel (b) and the surface and bulk band gap are indicated in panel (c).

**Table 6.5.** Summary of the conduction and valence band bending and the resulting surface band gap, as a function of 2D electron density. The 2D electron density ($N_{2D}$) is given in units of $\times 10^{13}$ cm$^{-2}$, all other values are in eV.

| | | Fixed Mass | | Two Mass | |
|---|---|---|---|---|---|
| $N_{2D}$ | $V_{VBB}$ | $V_{CBB}$ | $E_G^{surf}$ | $V_{CBB}$ | $E_G^{surf}$ |
| 4.71 | 0.81 | 1.03 | 1.98 | 1.59 | 1.42 |
| 6.13 | 1.04 | 1.29 | 1.95 | 1.91 | 1.33 |
| 7.69 | 1.08 | 1.47 | 1.81 | 2.11 | 1.17 |
| 8.80 | 1.10 | 1.61 | 1.69 | 2.27 | 1.03 |

approach it can be observed that the surface band gap is reduced with respect to that of the bulk. This reduction of the surface band gap is much stronger for the two mass approach where a much deeper and steeper potential well is predicted. Both approaches show the surface band gap to be further reduced by increasing the 2D electron density. From the calculated band bending profiles it is interesting to note that the potential well has a spacial extent of $\sim$ 5 nm, which is very similar to other oxide surfaces and interfaces including $In_2O_3$ [185] and the $LaAlO_3/SrTiO_3$ interface [186].

The variation of the surface band gap ($E_G^{surf}$) as a function of 2D electron density ($N_{2D}$) is shown in figure 6.12. It is interesting to note that despite the large difference in the initial surface band gap obtained by the fixed mass and two mass approaches, the decrease in surface band gap is very similar for both at $\sim$ 0.35 eV. This correlation between the surface band gap and 2D electron density provides strong evidence that the origin of this surface band gap narrowing is many-body interactions. Many-body interactions have been shown to result in band gap shrinkage in degenerately doped bulk semiconductors [141], and this idea has been explored further in reference [187].

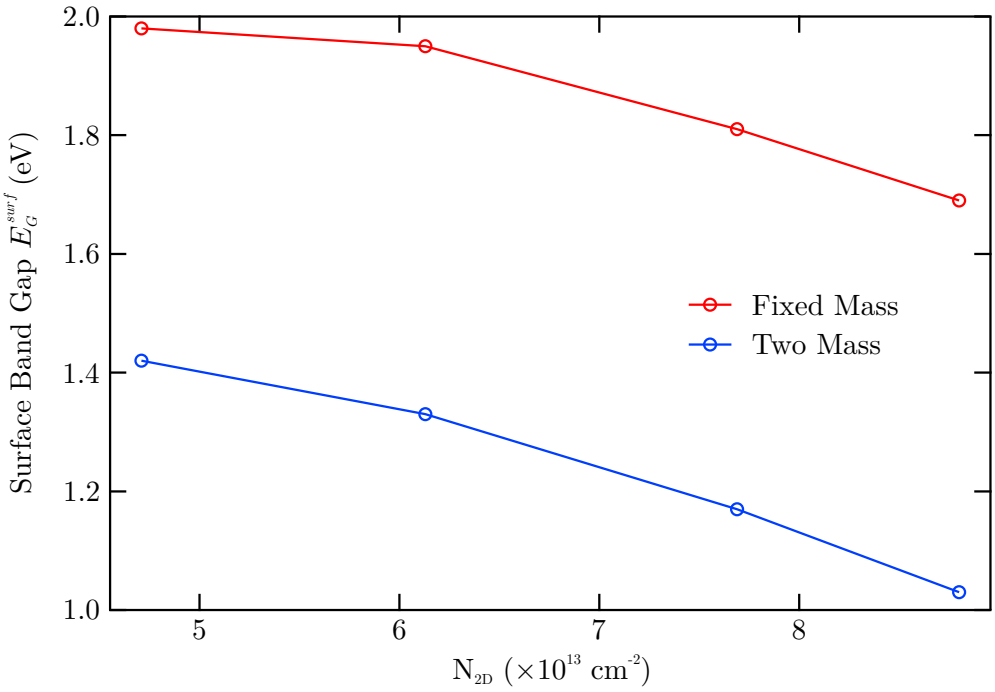


**Figure 6.12.** Surface band gap as a function of 2D electron density ($N_{2D}$). The values obtained from both the fixed mass and two mass fitting approaches are shown.

## 6.4 Conclusions

In this chapter the effects of depositing sub ML coverage of Rb on the CdO surface have been investigated. As the CdO(100) surface already supports an intrinsic electron accumulation layer with a Q2DEG, the addition of Rb can serve as a means to increase the electron density at the surface and achieve control over the Q2DEG. The measurement and analysis of the Fermi surface allowed the 2D electron density to be directly obtained. A method of radial integration and peak fitting was developed to allow $k_f$ values associated with the subbands to be accurately obtained. From this analysis it was found that the 2D electron density was increased from $4.71 \times 10^{13}$ cm$^{-2}$ to $8.8 \times 10^{13}$ cm$^{-2}$ by the addition of Rb to the surface, almost doubling the 2D electron density.

The dispersion of the Q2DEG states was also measured, the addition of the Rb caused the states to shift to higher BE. In order to analyse the dispersion quantitatively, it was extracted using a combination of MDC and EDC fitting. Once

extracted, the dispersion could be compared with the simulations produced by conducting coupled Poisson-Schrödinger calculations. Several differing approaches were applied to model the subband dispersion. Initially the approach of fixing the effective mass at the bulk value was used, but this resulted in poor agreement with the measured subband dispersion. The effective mass was then added as a fitting parameter resulting in closer agreement with the measured dispersions, and suggesting that the subbands do have a significantly lighter effective mass than the bulk CB. Finally the effective mass used to calculated the subband dispersion, and the effective mass used to calculate the band bending profile were separated. The bulk CB effective mass was used to calculate the band bending profile and the subband effective mass was treated as a fitting parameter. This approach led to extremely good agreement of the simulated and measured subband dispersions, with both subbands being extremely well reproduced despite only the outer subband being considered when performing the fitting.

The effective mass value obtained by fitting the subband dispersions using either the one mass or the two mass approach gave similar results of a subband mass of $\sim 0.14m_e$, considerably lower than the bulk CB effective mass of $0.24m_e$. Additional evidence for the confined subband states exhibiting a low effective mass was provided by direct parabolic fitting of the subband dispersion, and additionally has been observed in similar oxide 2DEGs.

Finally, the simulation of the subband states allows a value of the CBB to be obtained, and coupled with the knowledge of the VBB extracted from VB and shallow core level analysis allows the surface band gap to be investigated. The CdO surface is found to exhibit surface band gap narrowing, with this effect being enhanced by an increase in the 2D electron density. This correlation between the surface band gap and the 2D electron density is taken as strong evidence that the narrowing is driven by many-body interactions ($e$-$e$ and electron-phonon ($e$-$p$)) within the accumulation layer.

The results presented in this chapter demonstrate that alkali metal deposition onto a surface with an electron accumulation layer can serve as a method to further enhance the surface electron density. The lower effective mass of the subbands compared to the bulk and the significant surface band gap narrowing, which increases with electron density, are strong indications that many-body effects are significant at the CdO(100) surface. Further theoretical effort is needed to understand the mechanism by which the subband effective mass is lowered. Typically in systems where quasi-particles play an important role, such as the high $T_C$ superconductors, many-body interactions lead to "mass-enhancement" [188]. Recently the Ruddlesden-Popper ruthenate $SrRuO_3$ has been demonstrated to exhibit a similar mass-enhancement effect [189]. However, this can be contrasted to the cases of $SrTiO_3$(001) [184] and $In_2O_3$(111) [185] where similarly low effective masses of Q2DEG states have been observed. These results serve to highlight that both the origin and resulting properties of surface 2DEGs, particularly at oxide surfaces and interfaces, are still not well understood. This is therefore an area of strong interest where potentially interesting or novel functional properties could still be discovered.

# CHAPTER 7

# Conclusions

## 7.1 Summary and Conclusions

This thesis has been concerned with the determination of electronic properties of single crystal CdO thin films. These films have been studied with a variety of photoemission techniques, principally utilising synchrotron radiation. Firstly the use of HAXPES in chapter 4 allowed photoemission measurements of CdO in the as-grown condition, thus avoiding the reduction in carrier concentration typically observed upon annealing which is required to make conventional photoemission measurements. Effects associated with high carrier concentrations ($> 10^{20}$ cm$^{-3}$) were then observed, including: core level shifts, band gap renormalisation, and the effects of plasmons or final state screening on the core level line shapes. The observation of plasmon satellites allows the sample carrier concentration to be extracted directly from the photoemission measurement, and this was found to be in excellent agreement with Hall effect measurements. These results show HAXPES can be a powerful technique in accessing the bulk properties of TCOs which can be especially useful when trying to determine the sources of bulk electronic properties, whilst avoiding the effects of surface electron accumulation which appears to be an almost universal property of TCOs.

In chapter 5 the electronic structure of CdO was investigated with a combination

of SR-PES, and DFT. The experimentally measured location of the Cd $4d$ states were not reproduced by either LDA or PBE-GGA. However, LDA+$U$ applied using a theoretically calculated U value of 2.34 eV was very successful in predicting the location of these states. The photon energy dependence of the VB-PES was measured and compared to theoretical predictions by utilising the one-electron photoionisation cross-sections. The DFT calculations qualitatively reproduced the observed behaviour, with LDA+$U$ again being the most accurate. However there are still discrepancies between the theory and experiment, and these were assigned to both an underestimation of the Cd $4p$ character in the VB and to the O $2p$ photoionisation cross-sections, which appears to decrease too rapidly with photon energy. These observations are in agreement with other studies. The change in VB shape with photon energy highlights the potential for this kind of approach in understanding the orbital character present in the VB, especially within TCOs where there are strong variations in the photoionisation cross-section behaviour of the orbitals which constitute the VB. This technique can be extended by varying the polarisation, allowing even more detailed information to be obtained by allowing certain orbital characters to be suppressed. In order to exploit this approach further, the photoionisation cross-sections at the high photon energies, relevant for HAXPES, should be examined experimentally to confirm their accuracy. Despite the success of DFT in reproducing many elements of the experiment, the functionals applied here (LDA, PBE, LDA+$U$) still significantly underestimate the CdO band gap. This clearly illustrates the need for more sophisticated theoretical approaches when investigating these materials, such as hybrid functionals and $GW$ quasiparticle methods. These improvements in theoretical approaches will require ever more sophisticated experiments to adequately assess their predictions, an area where photoemission can play a key role.

Finally, in chapter 6, the effects of depositing Rb on the CdO surface have been investigated by ARPES. As the CdO(100) surface already supports an intrinsic

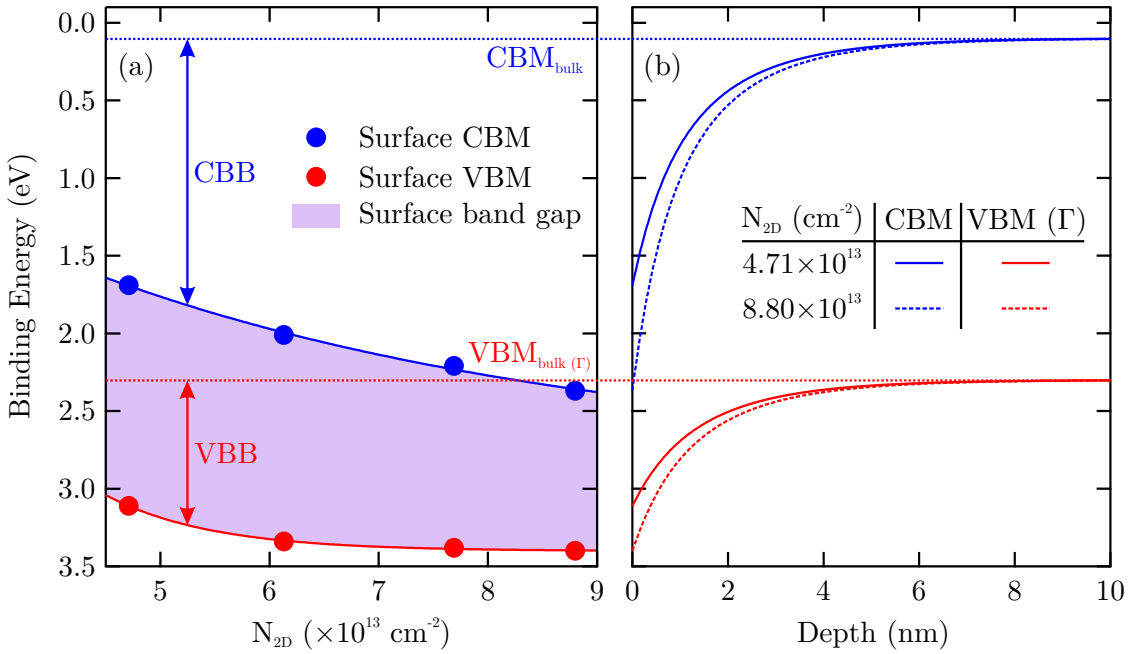


**Figure 7.1.** Summary of surface band bending investigated in this thesis. (a) Surface CBM and VBM as a function of 2D electron density to allow the shrinking of the surface band gap to be observed. (b) CB and VB bending profiles for the lowest and highest 2D electron densities investigated in this thesis to compare how the band bending changes. The results shown are from the two mass model.

electron accumulation layer with a Q2DEG, the addition of Rb can serve as a way to increase the electron density and achieve control over the Q2DEG. The range of 2D electron densities achieved here was $4.71 \times 10^{13}$ cm$^{-2}$ to $8.8 \times 10^{13}$ cm$^{-2}$, giving almost a doubling of the 2D electron density by the addition of Rb. The dispersion of the Q2DEG subband states was measured, and compared with the simulations produced by conducting coupled Poisson-Schrödinger calculations. Several differing approaches were applied to model the subband dispersion, with the results indicating that the subband states have a significantly lower effective mass than reported values for the bulk. Additionally, the simulation of the subband states allows a value of the CBB to be obtained, and coupled with the knowledge of the VBB extracted from VB and shallow core level analysis allowed the surface band gap to be investigated. The CdO(100) surface is found to exhibit surface band gap narrowing, and this effect is enhanced by the increased 2D electron density. This correlation between the surface band gap and the 2D electron density, summarised in figure 7.1, is taken as

strong evidence that the narrowing is driven by many-body interactions ($e$-$e$ and $e$-$p$) within the accumulation layer. Further theoretical effort is needed to understand the mechanism by which the subband effective mass is lowered, and the surface band gap is narrowed.

## 7.2 Future Work

The use of HAXPES to study CdO allowed photoemission measurements of as-grown samples with high carrier concentration. However, the source of this high carrier concentration has still not been determined experimentally. The decrease in carrier concentration on annealing would suggest that the origin is not likely to be oxygen vacancies, as is commonly assumed for TCOs. This leaves other possibilities, particularly hydrogen which is present in abundance during the growth of the samples studied within this thesis. As hydrogen is difficult to detect using photoemission, but could be assumed to easily diffuse out of CdO at elevated temperature, a temperature programmed desorption (TPD) experiment would be ideal to test this hypothesis. In addition, this experiment could give information about the activation energies of this process, which could be compared to theory.

Potential uses of CdO in gas sensing applications rely on the surface electronic properties. As has been shown in this thesis, ARPES is an extremely sensitive probe of these properties, and therefore an investigation into the effects of gas exposure on the CdO surface using ARPES would be valuable in determining the source of this sensitivity, and therefore enhance or manipulate this capability. This type of study may also be applied more widely to the range of metal oxides currently in use as gas sensors to understand more about the operation of these devices.

The low subband effective mass and surface band gap narrowing at the CdO surface have been assigned to many-body interactions. Although this assignment seems to qualitatively explain the observed effects, no spectroscopic evidence of these effects have yet been published for any binary oxide system (only very recently have they

been observed in $SrTiO_3$ [190]). Therefore to observe kinks in the subband dispersion would serve as unambiguous identification of these effects. As to why these dispersion anomalies are not observed in the ARPES data presented here, it may be that the surface preparation approach used caused too much surface roughness, as observation of dispersion anomalies up to now has mostly been achieved on surfaces cleaved in-situ. Therefore an improved approach to the surface preparation and further improved growth, when combined with extremely high resolution ARPES measurements may allow experimental observation of these effects.

Finally all the work presented in this thesis has been conducted on the (100) face of CdO, however it would be of interest to examine the properties of other high symmetry surfaces such as (110) and (111). The unreconstructed (110) face would have alternating rows of Cd and O, which could be expected to give rise to anisotropic surface properties [191]. The unreconstructed (111) face would be terminated by a complete layer of Cd or O and would therefore be polar. This is expected to be a high energy situation which should lead to a reconstruction, and perhaps interesting physics such as the "polar catastrophe" observed during the growth of $SrTiO_3/LaAlO_3$ [192]. However the investigation of these surfaces is ultimately dependent on the ability to control the growth of the required structures.

# Bibliography


[1] J. Heber, Nature **459**, 28 (2009).

[2] J. Mannhart and D. G. Schlom, Science **327**, 1607 (2010).

[3] H. Y. Hwang, Y. Iwasa, M. Kawasaki, B. Keimer, N. Nagaosa, and Y. Tokura, Nat. Mater. **11**, 103 (2012).

[4] D. S. Ginley, ed., *Handbook of Transparent Conductors* (Springer US, Boston, MA, 2011).

[5] J. Meyer, S. Hamwi, M. Kröger, W. Kowalsky, T. Riedl, and A. Kahn, Adv. Mater. **24**, 5408 (2012).

[6] J. Wu, J. Cao, W.-Q. Han, A. Janotti, and H.-C. Kim, eds., *Functional Metal Oxide Nanostructures*, Springer Series in Materials Science, Vol. 149 (Springer New York, New York, NY, 2012).

[7] A. Tsukazaki, A. Ohtomo, T. Kita, Y. Ohno, H. Ohno, and M. Kawasaki, Science **315**, 1388 (2007).

[8] A. Ohtomo and H. Y. Hwang, Nature **427**, 423 (2004).

[9] A. McCollam, S. Wenderich, M. K. Kruize, V. K. Guduru, H. J. A. Molegraaf, M. Huijben, G. Koster, D. H. A. Blank, G. Rijnders, A. Brinkman, H. Hilgenkamp, U. Zeitler, and J. C. Maan, APL Mater. **2**, 022102 (2014).

[10] S. Gariglio, N. Reyren, A. D. Caviglia, and J.-M. Triscone, J. Phys. Condens. Matter **21**, 164213 (2009).

[11] J. A. Bert, B. Kalisky, C. Bell, M. Kim, Y. Hikita, H. Y. Hwang, and K. A. Moler, Nat. Phys. **7**, 767 (2011).

[12] A. Brinkman, M. Huijben, M. van Zalk, J. Huijben, U. Zeitler, J. C. Maan, W. G. van der Wiel, G. Rijnders, D. H. a. Blank, and H. Hilgenkamp, Nat. Mater. **6**, 493 (2007).

[13] K. Nomura, H. Ohta, K. Ueda, T. Kamiya, M. Hirano, and H. Hosono, Science **300**, 1269 (2003).

[14] T. Minami, Thin Solid Films **516**, 5822 (2008).

[15] T. J. Coutts, D. L. Young, X. Li, W. P. Mulligan, and X. Wu, J. Vac. Sci. Technol. A **18**, 2646 (2000).

[16] P. D. C. King and T. D. Veal, J. Phys. Condens. Matter **23**, 334214 (2011).

[17] F. Streintz, Ann. Phys. **314**, 854 (1902).

[18] K. Bädeker, Ann. Phys. **327**, 749 (1907).

[19] R. Chandiramouli and B. Jeyaprakash, Solid State Sci. **16**, 102 (2013).

[20] J. Zuñiga Pérez, C. Munuera, C. Ocal, and V. Muñoz Sanjosé, J. Cryst. Growth **271**, 223 (2004).

[21] Y. Yang, S. Jin, J. E. Medvedeva, J. R. Ireland, A. W. Metz, J. Ni, M. C. Hersam, A. J. Freeman, and T. J. Marks, J. Am. Chem. Soc. **127**, 8796 (2005).

[22] A. B. M. A. Ashrafi, H. Kumano, I. Suemune, Y.-W. Ok, and T.-Y. Seong, Appl. Phys. Lett. **79**, 470 (2001).

[23] A. B. M. A. Ashrafi, H. Kumano, I. Suemune, Y. W. Ok, and T. Y. Seong, J. Cryst. Growth **237-239**, 518 (2002).

[24] M. Yan, M. Lane, C. R. Kannewurf, and R. P. H. Chang, Appl. Phys. Lett. **78**, 2342 (2001).

[25] B. J. Zheng, J. S. Lian, L. Zhao, and Q. Jiang, Appl. Surf. Sci. **256**, 2910 (2010).

[26] S. Duman, G. Turgut, F. Ş. Özçelik, and B. Gurbulak, Mater. Lett. **126**, 232 (2014).

[27] S. Aksoy, Y. Caglar, S. Ilican, and M. Caglar, Int. J. Hydrogen Energy **34**, 5191 (2009).

[28] W.-M. Cho, G.-R. He, T.-H. Su, and Y.-J. Lin, Appl. Surf. Sci. **258**, 4632 (2012).

[29] K. M. Yu, M. A. Mayer, D. T. Speaks, H. He, R. Zhao, L. Hsu, S. S. Mao, E. E. Haller, and W. Walukiewicz, J. Appl. Phys. **111**, 123505 (2012).

[30] R. R. Salunkhe and C. D. Lokhande, Sensors Actuators B Chem. **129**, 345 (2008).

[31] T. Krishnakumar, R. Jayaprakash, T. Prakash, D. Sathyaraj, N. Donato, S. Licoccia, M. Latino, a. Stassi, and G. Neri, Nanotechnology **22**, 325501 (2011).

[32] Z. Guo, M. Li, and J. Liu, Nanotechnology **19**, 245611 (2008).

[33] N. Rajesh, J. Kannan, S. Leonardi, G. Neri, and T. Krishnakumar, J. Alloys Compd. **607**, 54 (2014).

[34] H. Landolt and R. Börnstein, *Landolt-Börnstein Numerical Data and Functional Relationships in Science and Technology: New Series. Volume 17 Semiconductors.* (Springer-Verlag, 1982).

[35] F. Koffyberg, Phys. Rev. B **13**, 4470 (1976).

[36] I. N. Demchenko, J. D. Denlinger, M. Chernyshova, K. M. Yu, D. T. Speaks, P. Olalde-Velasco, O. Hemmers, W. Walukiewicz, A. Derkachova, and K. Lawniczak-Jablonska, Phys. Rev. B **82**, 075107 (2010).

[37] M. Burbano, D. O. Scanlon, and G. W. Watson, J. Am. Chem. Soc. **133**, 15065 (2011).

[38] S. K. Vasheghani Farahani, T. D. Veal, P. D. C. King, J. Zúñiga Pérez, V. Muñoz Sanjosé, and C. F. McConville, J. Appl. Phys. **109**, 073712 (2011).

[39] P. H. Jefferson, S. A. Hatfield, T. D. Veal, P. D. C. King, C. F. McConville, J. Zúñiga Pérez, and V. Muñoz Sanjosé, Appl. Phys. Lett. **92**, 022101 (2008).

[40] K. Momma and F. Izumi, J. Appl. Crystallogr. **44**, 1272 (2011).

[41] N. W. Ashcroft and N. D. Mermin, *Solid State Physics* (Brooks/Cole, Cengage Learning, New York, 1976).

[42] W. Shockley, Physical Review **56**, 317 (1939).

[43] W. Mönch, *Semiconductor surfaces and interfaces*, Vol. 26 (Springer, 2001).

[44] V. Heine, Phys. Rev. **138**, A1689 (1965).

[45] Y.-C. Chang, Phys. Rev. B **25**, 605 (1982).

[46] Y.-C. Chang and J. Schulman, Phys. Rev. B **25**, 3975 (1982).

[47] C. Tejedor and F. Flores, J. Phys. C Solid State Phys. **11**, L19 (1977).

[48] J. Tersoff, Phys. Rev. Lett. **52**, 465 (1984).

[49] J. C. Inkson, J. Phys. C Solid State Phys. **13**, 369 (1980).

[50] W. Mönch, J. Appl. Phys. **80**, 5076 (1996).

[51] J. Tersoff, Phys. Rev. B **32**, 6968 (1985).

[52] J. C. Slater, J. Chem. Phys. **41**, 3199 (1964).

[53] A. L. Allred, J. Inorg. Nucl. Chem. **17**, 215 (1961).

[54] P. D. C. King, T. D. Veal, P. H. Jefferson, J. Zúñiga Pérez, V. Muñoz Sanjosé, and C. F. McConville, Phys. Rev. B **79**, 35203 (2009).

[55] A. A. Dakhel, Semicond. Sci. Technol. **23**, 055017 (2008).

[56] D. T. Speaks, M. A. Mayer, K. M. Yu, S. S. Mao, E. E. Haller, and W. Walukiewicz, J. Appl. Phys. **107**, 113706 (2010).

[57] C. G. Van de Walle and J. Neugebauer, Nature **423**, 626 (2003).

[58] J. Suh, D. Fu, X. Liu, J. K. Furdyna, K. M. Yu, W. Walukiewicz, and J. Wu, Phys. Rev. B **89**, 115307 (2014).

[59] P. D. C. King, T. Veal, F. Fuchs, C. Wang, D. J. Payne, A. Bourlange, H. Zhang, G. Bell, V. Cimalla, O. Ambacher, R. Egdell, F. Bechstedt, and C. McConville, Phys. Rev. B **79**, 205211 (2009).

[60] T. D. Veal, P. D. C. King, S. A. Hatfield, L. R. Bailey, C. F. McConville, B. Martel, J. C. Moreno, E. Frayssinet, F. Semond, and J. Zúñiga Pérez, Appl. Phys. Lett. **93**, 202108 (2008).

[61] P. D. C. King, T. D. Veal, P. H. Jefferson, C. F. McConville, T. Wang, P. J. Parbrook, H. Lu, and W. J. Schaff, Appl. Phys. Lett. **90**, 132105 (2007).

[62] P. D. C. King, T. Veal, C. Kendrick, L. Bailey, S. Durbin, and C. McConville, Phys. Rev. B **78**, 033308 (2008).

[63] B. Falabretti and J. Robertson, J. Appl. Phys. **102**, 123703 (2007).

[64] V. N. Brudnyi, S. N. Grinyaev, and N. G. Kolin, Semiconductors **37**, 537 (2003).

[65] P. D. C. King, T. Veal, P. Jefferson, S. Hatfield, L. Piper, C. McConville, F. Fuchs, J. Furthmüller, F. Bechstedt, H. Lu, and W. Schaff, Phys. Rev. B **77**, 045316 (2008).

[66] P. D. C. King, T. D. Veal, C. F. McConville, J. Zúñiga Pérez, V. Muñoz Sanjosé, M. Hopkinson, E. D. L. Rienks, M. F. Jensen, and P. Hofmann, Phys. Rev. Lett. **104**, 256803 (2010).

[67] A. Askarinejad and A. Morsali, Mater. Lett. **62**, 478 (2008).

[68] G. Reza Khayati, H. Dalvand, E. Darezereshki, and A. Irannejad, Mater. Lett. **115**, 272 (2014).

[69] D. Sathya Raj, R. Jayaprakash, T. Prakash, S. Kumar, G. Neri, and T. Krishnakumar, Appl. Surf. Sci. **266**, 268 (2013).

[70] H. Hertz, Ann. Phys. **31**, 983 (1887).

[71] A. Einstein, Ann. Phys. **322**, 132 (1905).

[72] K. Siegbahn, Science **217**, 111 (1982).

[73] Ph. Hofmann, *Surface Physics, An Introduction* (Self Published, 2013).

[74] J. C. Vickerman and I. Gilmore, *Surface Analysis: The Principal Techniques* (Wiley, 2009).

[75] Omicron Nanotechnology, "EA 125 Energy Analyser User Guide," (2002).

[76] M. Cardona and L. Ley, eds., *Photoemission in Solids I*, Topics in Applied Physics, Vol. 26 (Springer Berlin Heidelberg, Berlin, Heidelberg, 1978).

[77] D. A. Shirley, Phys. Rev. B **5**, 4709 (1972).

[78] S. Tougaard, Surf. Sci. **216**, 343 (1989).

[79] C. S. Fadley, J. Electron Spectros. Relat. Phenomena **178-179**, 2 (2010).

[80] S. Suga and A. Sekiyama, *Photoelectron Spectroscopy: Bulk and Surface Electronic Structures*, Springer Series in Optical Sciences (Springer London, Limited, 2013).

[81] T. Kiss, T. Shimojima, F. Kanetaka, K. Kanai, T. Yokoya, S. Shin, Y. Onuki, T. Togashi, C. Zhang, C. Chen, and S. Watanabe, J. Electron Spectros. Relat. Phenomena **144-147**, 953 (2005).

[82] J. D. Koralek, J. F. Douglas, N. C. Plumb, J. D. Griffith, S. T. Cundiff, H. C. Kapteyn, M. M. Murnane, and D. S. Dessau, Rev. Sci. Instrum. **78**, 053905 (2007).

[83] A. Tamai, W. Meevasana, P. D. C. King, C. W. Nicholson, A. de la Torre, E. Rozbicki, and F. Baumberger, Phys. Rev. B **87**, 075113 (2013).

[84] C. S. Fadley, Nucl. Instruments Methods Phys. Res. Sect. A Accel. Spectrometers, Detect. Assoc. Equip. **547**, 24 (2005).

[85] W. Drube, J. Electron Spectros. Relat. Phenomena **190**, 125 (2013).

[86] A. Zangwill, *Physics at Surfaces* (Cambridge University Press, 1988).

[87] D. R. Penn, J. Electron Spectros. Relat. Phenomena **9**, 29 (1976).

[88] S. Hofmann, *Auger and X-Ray Photoelectron Spectroscopy in Materials Science: A User-Oriented Guide*, Springer Series in Surface Sciences (Springer, 2012).

[89] S. Tanuma, C. J. Powell, and D. R. Penn, Surf. Interface Anal. **21**, 165 (1993).

[90] S. Tanuma, C. J. Powell, and D. R. Penn, Surf. Interface Anal. **43**, 689 (2011).

[91] M. B. Trzhaskovskaya, V. I. Nefedov, and V. G. Yarzhemsky, At. Data Nucl. Data Tables **77**, 97 (2001).

[92] J. W. Cooper, Phys. Rev. A **47**, 1841 (1993).

[93] J. Yeh and I. Lindau, At. Data Nucl. Data Tables **32**, 1 (1985).

[94] J. H. Scofield, J. Electron Spectros. Relat. Phenomena **8**, 129 (1976).

[95] J. H. Scofield, Lawrence Livermore Lab. Rep. No. UCRL-51326 (1973).

[96] M. B. Trzhaskovskaya, V. I. Nefedov, and V. G. Yarzhemsky, At. Data Nucl. Data Tables **82**, 257 (2002).

[97] M. B. Trzhaskovskaya, V. K. Nikulin, V. I. Nefedov, and V. G. Yarzhemsky, At. Data Nucl. Data Tables **92**, 245 (2006).

[98] A. Damascelli, Phys. Scr. **T109**, 61 (2004).

[99] A. X. Gray, C. Papp, S. Ueda, B. Balke, Y. Yamashita, L. Plucinski, J. Minár, J. Braun, E. R. Ylvisaker, C. M. Schneider, W. E. Pickett, H. Ebert, K. Kobayashi, C. S. Fadley, and J. Minar, Nat. Mater. **10**, 759 (2011).

[100] A. X. Gray, J. Minár, S. Ueda, P. R. Stone, Y. Yamashita, J. Fujii, J. Braun, L. Plucinski, C. M. Schneider, G. Panaccione, H. Ebert, O. D. Dubon, K. Kobayashi, and C. S. Fadley, Nat. Mater. **11**, 957 (2012).

[101] S. Hüfner, *Photoelectron Spectroscopy: Principles and Applications*, Advanced Texts in Physics (Springer, 2003).

[102] S. V. Hoffmann, C. Søndergaard, C. Schultz, Z. Li, and P. Hofmann, Nucl. Instruments Methods Phys. Res. Sect. A Accel. Spectrometers, Detect. Assoc. Equip. **523**, 441 (2004).

[103] R. Stensgaard, Phys. Scr. **T22**, 315 (1988).

[104] J. S. Hangst, K. Berg-Sø rensen, P. S. Jessen, M. Kristensen, K. Mø lmer, J. S. Nielsen, P. Poulsen, J. P. Schiffer, and P. Shi, Nucl. Instruments Methods Phys. Res. Sect. B Beam Interact. with Mater. Atoms **68**, 17 (1992).

[105] E. H. Hall, Am. J. Math. **2**, 287 (1879).

[106] E. Ramsden, *Hall-Effect Sensors: Theory and Application* (Elsevier Science, 2011).

[107] L. J. van der Pauw, Philips Res. Rep. **13**, 1 (1958).

[108] P. Y. Yu and M. Cardona, *Fundamentals of Semiconductors: Physics and Materials Properties*, Graduate Texts in Contemporary Physics (Springer, 2010).

[109] K. Seeger, *Semiconductor Physics: An Introduction*, Advanced Texts in Physics (U.S. Government Printing Office, 2004).

[110] D. P. Woodruff and T. A. Delchar, *Modern Techniques of Surface Science* (Cambridge University Press, 1994).

[111] M. A. Van Hove, W. H. Weinberg, and C. M. Chan, *Low-Energy Electron Diffraction: Experiment, Theory and Surface Structure Determination*, Springer Series in Surface Sciences (Springer London, Limited, 2011).

[112] J. B. Pendry, *Low Energy Electron Diffraction: The Theory and its Application to Determination of Surface Structure*, Techniques of Physics Series (Academic Press, 1974).

[113] L. F. J. Piper, P. H. Jefferson, T. D. Veal, C. F. McConville, J. Zuñiga Pérez, and V. Muñoz Sanjosé, Superlattices Microstruct. **42**, 197 (2007).

[114] Y. Dou, R. Egdell, T. Walker, D. Law, and G. Beamson, Surf. Sci. **398**, 241 (1998).

[115] P. D. C. King, T. D. Veal, A. Schleife, J. Zúñiga Pérez, B. Martel, P. H. Jefferson, F. Fuchs, V. Muñoz Sanjosé, F. Bechstedt, and C. F. McConville, Phys. Rev. B **79**, 205205 (2009).

[116] L. F. J. Piper, L. Colakerol, P. D. C. King, A. Schleife, J. Zúñiga Pérez, P.-A. Glans, T. Learmonth, A. Federov, T. D. Veal, F. Fuchs, V. Muñoz Sanjosé, F. Bechstedt, C. F. McConville, and K. E. Smith, Phys. Rev. B **78**, 165127 (2008).

[117] M. Born and R. Oppenheimer, Ann. Phys. **389**, 457 (1927).

[118] E. O. Kane, J. Phys. Chem. Solids **1**, 249 (1957).

[119] M. Willatzen and L. C. Lew Yan Voon, *The $k \cdot p$ Method* (Springer Berlin Heidelberg, Berlin, Heidelberg, 2009).

[120] S. K. Vasheghani Farahani, V. Muñoz Sanjosé, J. Zúñiga Pérez, C. F. McConville, and T. D. Veal, Appl. Phys. Lett. **102**, 022102 (2013).

[121] K. Burke, "The ABC of DFT," (2007).

[122] D. Sholl and J. A. Steckel, *Density Functional Theory: A Practical Introduction* (Wiley, 2011).

[123] S. Cottenier, "Density Functional Theory and the Family of (L)APW-methods: a step-by-step introduction," (2013).

[124] D. J. Singh and L. Nordström, *Planewaves, Pseudopotentials, and the LAPW method*, 2nd ed. (Springer, 2005).

[125] J. Kitchin, "Modeling materials using density functional theory," (2012).

[126] P. Hohenberg, Phys. Rev. **136**, B864 (1964).

[127] W. Kohn and L. J. Sham, Phys. Rev. **140**, A1133 (1965).

[128] J. P. Perdew, K. Burke, and M. Ernzerhof, Phys. Rev. Lett. **77**, 3865 (1996).

[129] A. D. Becke, Phys. Rev. A **38**, 3098 (1988).

[130] C. Lee, W. Yang, and R. G. Parr, Phys. Rev. B **37**, 785 (1988).

[131] F. Aryasetiawan and O. Gunnarsson, Reports Prog. Phys. **61**, 237 (1998).

[132] O. K. Andersen, Phys. Rev. B **12**, 3060 (1975).

[133] E. Wimmer, H. Krakauer, M. Weinert, and A. J. Freeman, Phys. Rev. B **24**, 864 (1981).

[134] G. Paasch and H. Übensee, Phys. status solidi **113**, 165 (1982).

[135] J.-P. Zöllner, H. Übensee, G. Paasch, T. Fiedler, and G. Gobsch, Phys. status solidi **134**, 837 (1986).

[136] P. King, T. Veal, and C. McConville, Physical Review B **77**, 125305 (2008).

[137] G. Wannier, Phys. Rev. **52**, 191 (1937).

[138] S. Abe, T. Inaoka, and M. Hasegawa, Phys. Rev. B **66**, 205309 (2002).

[139] P. Risterucci, O. Renault, E. Martinez, B. Detlefs, V. Delaye, J. Zegenhagen, C. Gaumer, G. Grenet, and S. Tougaard, Appl. Phys. Lett. **104**, 051608 (2014).

[140] Y. Dou, T. Fishlock, R. G. Egdell, D. S. L. Law, and G. Beamson, Phys. Rev. B **55**, R13381 (1997).

[141] K. Berggren and B. Sernelius, Phys. Rev. B **24**, 1971 (1981).

[142] T. Nagata, O. Bierwagen, M. E. White, M. Y. Tsai, Y. Yamashita, H. Yoshikawa, N. Ohashi, K. Kobayashi, T. Chikyow, and J. S. Speck, Appl. Phys. Lett. **98**, 232107 (2011).

[143] S. A. Chambers, T. Droubay, T. C. Kaspar, and M. Gutowski, J. Vac. Sci. Technol. B Microelectron. Nanom. Struct. **22**, 2205 (2004).

[144] J. N. Chazalviel, M. Campagna, G. K. Wertheim, and H. R. Shanks, Phys. Rev. B **16**, 697 (1977).

[145] L. Ley and M. Cardona, eds., *Photoemission in Solids II*, Topics in Applied Physics, Vol. 27 (Springer Berlin Heidelberg, Berlin, Heidelberg, 1979).

[146] J. J. Mudd, T.-L. Lee, V. Muñoz Sanjosé, J. Zúñiga Pérez, D. J. Payne, R. G. Egdell, and C. F. McConville, Phys. Rev. B **89**, 165305 (2014).

[147] R. G. Egdell, J. Rebane, T. J. Walker, and D. S. L. Law, Phys. Rev. B **59**, 1792 (1999).

[148] C. Körber, V. Krishnakumar, A. Klein, G. Panaccione, P. Torelli, A. Walsh, J. L. F. Da Silva, S.-H. Wei, R. G. Egdell, and D. J. Payne, Phys. Rev. B **81**, 165207 (2010).

[149] A. Bourlange, D. J. Payne, R. G. Palgrave, H. Zhang, J. S. Foord, R. G. Egdell, R. M. J. Jacobs, T. D. Veal, P. D. C. King, and C. F. McConville, J. Appl. Phys. **106**, 013703 (2009).

[150] P. D. C. King, T. D. Veal, H. Lu, S. A. Hatfield, W. J. Schaff, and C. F. McConville, Surf. Sci. **602**, 871 (2008).

[151] A. Kotani and Y. Toyozawa, J. Phys. Soc. Japan **37**, 912 (1974).

[152] A. Kotani and Y. Toyozawa, J. Phys. Soc. Japan **37**, 563 (1974).

[153] N. Beatham, P. A. Cox, R. G. Egdell, and A. F. Orchard, Chem. Phys. Lett. **69**, 479 (1980).

[154] M. Campagna, G. Wertheim, H. Shanks, F. Zumsteg, and E. Banks, Phys. Rev. Lett. **34**, 738 (1975).

[155] D. J. Payne, G. Paolicelli, F. Offi, G. Panaccione, P. Lacovig, G. Beamson, A. Fondacaro, G. Monaco, G. Vanko, and R. G. G. Egdell, J. Electron Spectros. Relat. Phenomena **169**, 26 (2009).

[156] V. Christou, M. Etchells, O. Renault, P. J. Dobson, O. V. Salata, G. Beamson, and R. G. Egdell, J. Appl. Phys. **88**, 5180 (2000).

[157] R. G. Egdell, T. J. Walker, and G. Beamson, J. Electron Spectros. Relat. Phenomena **128**, 59 (2003).

[158] D. J. Payne, R. G. Egdell, W. Hao, J. S. Foord, A. Walsh, and G. W. Watson, Chem. Phys. Lett. **411**, 181 (2005).

[159] H. Finkenrath, N. Uhle, and W. Waidelich, Solid State Commun. **7**, 11 (1969).

[160] A. Schleife, F. Fuchs, J. Furthmüller, and F. Bechstedt, Phys. Rev. B **73**, 245212 (2006).

[161] F. Labat, P. Baranek, C. Domain, C. Minot, and C. Adamo, J. Chem. Phys. **126**, 154703 (2007).

[162] H. Dixit, D. Lamoen, and B. Partoens, J. Phys. Condens. Matter **25**, 035501 (2013).

[163] A. Schleife, F. Fuchs, C. Rödl, J. Furthmüller, and F. Bechstedt, Phys. status solidi **246**, 2150 (2009).

[164] J. J. Mudd, T.-l. Lee, V. Muñoz Sanjosé, J. Zúñiga Pérez, D. Hesp, J. M. Kahk, D. J. Payne, R. G. Egdell, and C. F. McConville, Phys. Rev. B **89**, 035203 (2014).

[165] V. I. Anisimov, J. Zaanen, and O. K. Andersen, Phys. Rev. B **44**, 943 (1991).

[166] A. I. Liechtenstein, V. I. Anisimov, and J. Zaanen, Phys. Rev. B **52**, R5467 (1995).

[167] V. I. Anisimov, F. Aryasetiawan, and A. I. Lichtenstein, J. Phys. Condens. Matter **9**, 767 (1997).

[168] "Elk FP-LAPW DFT Code http://elk.sourceforge.net/," (2013).

[169] J. P. Perdew and A. Zunger, Phys. Rev. B **23**, 5048 (1981).

[170] A. Janotti, D. Segev, and C. G. Van de Walle, Phys. Rev. B **74**, 045202 (2006).

[171] F. D. Murnaghan, Proc. Natl. Acad. Sci. **30**, 244 (1944).

[172] R. Miloua, F. Miloua, A. Arbaoui, Z. Kebbab, and N. Benramdane, Solid State Commun. **144**, 5 (2007).

[173] D. J. Payne, R. G. Egdell, G. Paolicelli, F. Offi, G. Panaccione, P. Lacovig, G. Monaco, G. Vanko, A. Walsh, G. W. Watson, J. Guo, G. Beamson, P.-A. Glans, T. Learmonth, and K. E. Smith, Phys. Rev. B **75**, 153102 (2007).

[174] W. Drube, T. M. Grehk, S. Thieß, G. B. Pradhan, H. R. Varma, P. C. Deshmukh, and S. T. Manson, J. Phys. B At. Mol. Opt. Phys. **46**, 245006 (2013).

[175] V. Y. Aristov, J. Vac. Sci. Technol. B Microelectron. Nanom. Struct. **12**, 2709 (1994).

[176] R. Biagi, P. Fantini, V. De Renzi, M. Grazia Betti, C. Mariani, and U. del Pennino, Phys. Rev. B **67**, 155325 (2003).

[177] M. Bianchi, R. C. Hatch, Z. Li, P. Hofmann, F. Song, J. Mi, B. B. Iversen, Z. M. A. El-Fattah, P. Löptien, L. Zhou, A. a. Khajetoorians, J. Wiebe, R. Wiesendanger, and J. W. Wells, ACS Nano **6**, 7009 (2012).

[178] A. Bostwick, T. Ohta, T. Seyller, K. Horn, and E. Rotenberg, Nat. Phys. **3**, 36 (2006).

[179] A. Bostwick, T. Ohta, J. L. McChesney, T. Seyller, K. Horn, and E. Rotenberg, Solid State Commun. **143**, 63 (2007).

[180] M. Bianchi, E. D. L. Rienks, S. Lizzit, A. Baraldi, R. Balog, L. Hornekæ r, and P. Hofmann, Phys. Rev. B **81**, 041403 (2010).

[181] J. Luttinger, Phys. Rev. **119**, 1153 (1960).

[182] X. Li, D. L. Young, H. Moutinho, Y. Yan, C. Narayanswamy, T. A. Gessert, and T. J. Coutts, Electrochem. Solid-State Lett. **4**, C43 (2001).

[183] J. M. Rueben, Z. Yuankun, and A. André, J. Phys. D. Appl. Phys. **45**, 425302 (2012).

[184] W. Meevasana, P. D. C. King, R. H. He, S.-K. Mo, M. Hashimoto, A. Tamai, P. Songsiriritthigul, F. Baumberger, and Z.-X. Shen, Nat. Mater. **10**, 114 (2011).

[185] K. H. L. Zhang, R. G. Egdell, F. Offi, S. Iacobucci, L. Petaccia, S. Gorovikov, and P. D. C. King, Phys. Rev. Lett. **110**, 56803 (2013).

[186] Y. Y. Chu, Y. F. Liao, V. T. Tra, J. C. Yang, W. Z. Liu, Y. H. Chu, J. Y. Lin, J. H. Huang, J. Weinen, S. Agrestini, K.-D. Tsuei, and D. J. Huang, Appl. Phys. Lett. **99**, 262101 (2011).

[187] P. D. C. King, *Physics (College. Park. Md).*, Ph.D. thesis, University of Warwick (2009).

[188] S. Hüfner, ed., *Very high resolution photoelectron spectroscopy*, Lecture Notes in Physics, Vol. 715 (Springer Berlin Heidelberg, Berlin, Heidelberg, 2007).

[189] D. Shai, C. Adamo, D. Shen, C. Brooks, J. Harter, E. Monkman, B. Burganov, D. Schlom, and K. Shen, Phys. Rev. Lett. **110**, 087004 (2013).

[190] P. D. C. King, S. McKeown Walker, A. Tamai, A. de la Torre, T. Eknapakul, P. Buaphet, S.-K. Mo, W. Meevasana, M. S. Bahramy, and F. Baumberger, Nat. Commun. **5**, 3414 (2014).

[191] J. Zúñiga Pérez, C. Martínez-Tomás, V. Muñoz Sanjosé, C. Munuera, C. Ocal, and M. Laügt, J. Appl. Phys. **98**, 034311 (2005).

[192] N. Nakagawa, H. Y. Hwang, and D. A. Muller, Nat. Mater. **5**, 204 (2006).